



**TECHNISCHE
UNIVERSITÄT
WIEN**

Vienna University of Technology

DISSERTATION

Grazing incidence X-ray fluorescence combined with X-ray reflectivity: development of an evaluation software

ausgeführt zum Zwecke der Erlangung des akademischen Grades eines
Doktors der technischen Wissenschaften unter der Leitung von

Ao.Univ.Prof. Dipl.-Ing. Dr.techn. Christina Strelj

E141

Atominstitut

eingereicht an der Technischen Universität Wien

Fakultät für Physik

von

Dieter Ingerle

9426647

Floridsdorfer Hauptstraße 22/4/9, 1210 Wien

Wien, am 11. Juli 2017

Kurzfassung

Röntgenfluoreszenzanalyse unter streifendem Einfall (GIXRF) ist eine empfindliche, zerstörungsfreie analytische Methode, die den Effekt der totalen externen Reflexion von Röntgenstrahlen auf einer glatten, polierten Oberfläche nutzt. Da sie ein wertvolles Hilfsmittel für Prozessanalyse und -kontrolle in der Entwicklung und Herstellung von Halbleiterbauteilen ist, hat die Methode in den letzten Jahren einen Wiederaufschwung erlebt. Die ständige Verkleinerung im Bereich der Halbleitertechnik hat die Schichtdicken und Implantationstiefen auf wenige Nanometer reduziert und somit in den Bereich gebracht, in dem GIXRF sehr empfindlich ist. Bei GIXRF wird die Intensität der charakteristischen Röntgenfluoreszenz gemessen, die in einer Probe durch einen einfallenden Röntgenstrahl erzeugt wird. Der Strahl trifft die Probe dabei unter verschiedenen Winkeln unter streifendem Einfall im Bereich des Grenzwinkels, wodurch winkelabhängige Kurven gemessen werden. Der Verlauf dieser Kurven ist abhängig von der Schichtdicke und -dichte bzw. Tiefenverteilung der Elemente in der Probe. Da die Auswertung von GIXRF-daten nicht eindeutig bezüglich der genauen Verteilung von Implantaten oder der Korrelation von Dicke und Dichte bei Schichten ist, muss das Verfahren mit anderen Methoden kombiniert werden. Naheliegend ist hier die Röntgenreflektometrie, da sie ähnliche Messabläufe und Auswertverfahren verwendet und auf den gleichen physikalischen Prinzipien fußt. Eine kombinierte Analyse von GIXRF und XRR reduziert Mehrdeutigkeiten und experimentelle Unsicherheiten der individuellen Methoden.

In der vorliegenden Arbeit wird die technische Umsetzung eines kombinierten Messaufbaus anhand zweier Beispiele diskutiert. Das eine basiert auf einem selbst entwickeltem Spektrometer, während das andere die Adaptierung eines kommerziellen Diffraktometers zeigt. Weiters werden die Grundlagen der Datenauswertung durch gleichzeitige Berechnung und Anpassung der GIXRF- sowie der XRR-daten besprochen. Zur Ermittlung der Probenparameter werden globale Optimierungsverfahren eingesetzt. Basierend auf den besprochenen Ansätzen wurde ein Programmpaket mit benutzerfreundlicher grafischer Oberfläche entwickelt: JGIXA (Java Grazing Incidence X-ray Analysis). Ebenfalls besprochen werden, von der Software berechnete, notwendige instrumentelle Korrekturen, um die Simulation einer Messung zu vervollständigen. Das Auswertungsverfahren und die Software wurden anhand von Metall- und Metalloxidschichten auf sowie Arsenimplantaten in Silizium getestet. Die Ergebnisse und die Konvergenz der verschiedenen Optimierungsverfahren für diese Probentypen wer-

den verglichen. Einschränkungen der Methode aufgrund der begrenzten Kohärenz des Strahls werden untersucht. Schließlich werden noch Simulationen, die unter Annahme einer unbeeinflussten stehenden Welle erstellt wurden, und entsprechende Messungen von Nanopartikeln aus Eisen auf goldbeschichtetem Silizium gezeigt.

Abstract

Grazing Incidence XRF (GIXRF) is a very surface sensitive, nondestructive analytical tool making use of the phenomenon of total external reflection of X-rays on smooth polished surfaces. In recent years the method experienced a revival, being a powerful tool for process analysis and control in the development and fabrication of semiconductor based devices. Due to the downscaling of the process size for semiconductor devices, junction depths as well as layer thicknesses are reduced to a few nanometers, i.e. the length scale where GIXRF is highly sensitive. GIXRF measures the X-ray fluorescence induced by an X-ray beam incident under varying grazing angles and results in angle dependent intensity curves. These curves are correlated to the layer thickness, depth distribution and mass density of the elements in the sample. But the evaluation of these measurements is ambiguous with regard to the exact distribution function for the implants as well as for the thickness and density of nanometer-thin layers. In order to overcome this ambiguity, GIXRF can be combined with X-ray reflectometry (XRR). This is straightforward, as both techniques use similar measurement procedures and the same fundamental physical principles can be used for a combined data evaluation strategy. Such a combined analysis removes ambiguities in the determined physical properties of the studied sample and, being a correlative spectroscopic method, also significantly reduces experimental uncertainties of the individual techniques.

Possibilities for the technical realization of a combined instrument are discussed and two examples, one based on a table-top spectrometer, the other on a commercial diffractometer, are presented. The approach to a combined data analysis, realized by concurrent calculation and fitting of simultaneously recorded GIXRF and XRR data is presented. Global optimization algorithms are used for the determination of the sample parameters leading to the smallest chi-squared. Based on this approach a multi-platform software package equipped with a user-friendly graphic user interface (GUI) and offering various optimization algorithms was developed: JGIXA (Java Grazing Incidence X-ray Analysis). The software includes typical instrumental functions for the simulation of the spectrometer in use. Software and data evaluation approach were benchmarked by characterizing metal and metal oxide layers on Silicon as well as arsenic implants in silicon. The results of different optimization algorithms were compared to test the convergence of the algorithms. Restrictions of the technique due to the limited coherence of the beam were investigated. Finally, simulations and mea-

measurements of iron nanoparticles on a gold coated wafer are presented, using the assumption of an unaltered X-ray Standing Wave above the surface.

Part of this work has been published in the following publications:

1. D. Ingerle, G. Pepponi, F. Meirer, P. Wobrauschek, C. Strelti, JGIXA — A software package for the calculation and fitting of grazing incidence X-ray fluorescence and X-ray reflectivity data for the characterization of nanometer-layers and ultra-shallow-implants, *Spectrochim. Acta Part B At. Spectrosc.* 118 (2016) 20–28, doi:10.1016/j.sab.2016.02.010
2. B. Caby, F. Brigidi, D. Ingerle, E. Nolot, G. Pepponi, C. Strelti, L. Lutterotti, A. André, G. Rodriguez, P. Gergaud, M. Morales, D. Chateigner, Study of annealing-induced interdiffusion in In₂O₃/Ag/In₂O₃ structures by a combined X-ray reflectivity and grazing incidence X-ray fluorescence analysis, *Spectrochim. Acta Part B At. Spectrosc.* 113 (2015) 132–137, doi:10.1016/j.sab.2015.09.008
3. D. Ingerle, M. Schiebl, C. Strelti, P. Wobrauschek, Combination of grazing incidence x-ray fluorescence with x-ray reflectivity in one table-top spectrometer for improved characterization of thin layer and implants on/in silicon wafers, *Rev. Sci. Instrum.* 85 (2014) 83110, doi:10.1063/1.4893383
4. D. Ingerle, F. Meirer, G. Pepponi, E. Demenev, D. Giubertoni, P. Wobrauschek, C. Strelti, Combined evaluation of grazing incidence X-ray fluorescence and X-ray reflectivity data for improved profiling of ultra-shallow depth distributions., *Spectrochim. Acta. Part B. At. Spectrosc.* 99 (2014) 121–128, doi:10.1016/j.sab.2014.06.019
5. G. Pepponi, D. Giubertoni, M. Bersani, F. Meirer, D. Ingerle, G. Steinhauser, C. Strelti, P. Hoenicke, B. Beckhoff, Grazing incidence x-ray fluorescence and secondary ion mass spectrometry combined approach for the characterization of ultrashallow arsenic distribution in silicon, *J. Vac. Sci. Technol. B Microelectron. Nanom. Struct.* 28 (2010) C1C59, doi:10.1116/1.3292647
6. D. Ingerle, F. Meirer, N. Zoeger, G. Pepponi, D. Giubertoni, G. Steinhauser, P. Wobrauschek, C. Strelti, A new spectrometer for grazing incidence X-ray fluorescence for the characterization of Arsenic implants and Hf based high-k layers, *Spectrochim. Acta Part B At. Spectrosc.* 65 (2010) 429–433, doi:10.1016/j.sab.2010.02.015

Talks (1 invited) and Posters (1 best poster award) related to parts of this work have been presented at the following conferences:

1. D. Ingerle, G. Pepponi, F. Meirer, P. Wobrauschek, C. Strelti: "JGIXA - a software package for the calculation and fitting of grazing incidence X-ray flu-

- orescence and X-ray reflectivity data for the characterization of nanometer-layers and ultra-shallow-implants"; European Conference on X-ray Spectrometry (EXRS 2016), Gothenburg, Sweden; 19.06.2016 - 24.06.2016; oral
2. D. Ingerle, W. Artner, K. Hradil, C. Strelj: "Refitting an X-ray Diffraction System for combined GIXRF and XRR measurements"; European Conference on X-ray Spectrometry (EXRS 2016), Gothenburg, Sweden; 19.06.2016 - 24.06.2016; poster
 3. D. Ingerle, G. Pepponi, F. Meirer, P. Wobrauschek, C. Strelj: "Measurement, calculation and fitting of grazing incidence X-ray fluorescence and X-ray reflectivity data for the characterization of nanometer-layers and ultra-shallow-implants"; Chinese Conference on X-ray Spectrometry, Weihai, China; 27.09.2015 - 28.09.2015; oral
 4. D. Ingerle, P. Wobrauschek, C. Strelj, G. Pepponi, F. Meirer: "JGIXA - A Software Package for the Calculation and Fitting of Grazing Incidence X-ray Fluorescence and X-ray Reflectivity Data for the Characterization of Nanometer-layers and Ultra-shallow-implants"; TXRF 2015, Westminster, CO, USA; 03.08.2015 - 07.08.2015; oral
 5. B. Caby, B. Detlefs, G. Picot, E. Nolot, F. Brigidi, G. Pepponi, D. Ingerle, C. Strelj, L. Lutterotti, D. Chateigner, M. Morales: "Comparison of Four Data Analysis Software for Combined X-ray Reflectivity and Grazing Incidence X-ray Fluorescence Measurements"; TXRF 2015, Westminster, CO, USA; 03.08.2015 - 07.08.2015; oral
 6. D. Ingerle, P. Wobrauschek, C. Strelj, G. Pepponi, J. Leani, A. Migliori, A.G. Karydas, D. Eichert, W. Jark, J. Zecevic, F. Meirer: "Comparison of Grazing Incidence X-ray Fluorescence and X-ray Reflectivity Data Obtained at the XRF Beamline of the Elettra Sincrotrone Trieste and an Optimized Lab Spectrometer"; TXRF 2015, Westminster, CO, USA; 03.08.2015 - 07.08.2015; poster (best poster award)
 7. D. Ingerle, G. Pepponi, F. Meirer, M. Schiebl, D. Giubertoni, E. Demenev, P. Wobrauschek, C. Strelj: "New approach for characterization of ultra-shallow implants by simultaneous evaluation of GIXRF and XRR"; 63th Denver X-ray Conference (2014), Big Sky Montana, USA; 28.07.2014 - 01.08.2014; oral
 8. D. Ingerle, P. Wobrauschek, C. Strelj: "The influence of beam coherence on the GIXRF characterization of nanoparticles"; 63th Denver X-ray Conference (2014), Big Sky Montana, USA; 28.07.2014 - 01.08.2014; poster
 9. D. Ingerle, J. Kirschner, B. Caby, C. Strelj: "Investigation of fitness land-

- scapes for GIXRF and XRR"; 63th Denver X-ray Conference (2014), Big Sky Montana, USA; 28.07.2014 - 01.08.2014; poster
10. D. Ingerle, P. Wobrauschek, C. Strelti: "The influence of beam coherence on the GIXRF characterization of nanoparticles"; EXRS 2014, Bolgona, Italy; 16.06.2014 - 20.06.2014; poster
 11. D. Ingerle, J. Kirschner, B. Caby, C. Strelti: "Investigation of fitness landscapes for GIXRF and XRR"; EXRS 2014, Bolgona, Italy; 16.06.2014 - 20.06.2014; poster
 12. B. Caby, D. Ingerle, G. Pepponi, C. Strelti, E. Nolot, F. Mazen, M. Morales, D. Chateigner: "XRR & GiXRF combined analysis of Plasma Immersion Ion Implantation Ultra-Shallow junctions"; EXRS 2014, Bolgona, Italy; 16.06.2014 - 20.06.2014; oral
 13. D. Ingerle, G. Pepponi, F. Meirer, D. Giubertoni, E. Demenev, P. Wobrauschek, C. Strelti: "New approach for characterization of ultra-shallow implants by simultaneous evaluation of GIXRF and XRR"; 15th Int. Conference on TXRF and related methods, Osaka, Japan; 23.09.2013 - 26.09.2013; oral (invited)
 14. G. Pepponi, F. Meirer, F. Brigidi, E. Demenev, D. Giubertoni, S. Gennaro, M. Bersani, D. Ingerle, C. Strelti, G. Steinhauser, A. Mehta, P. Pianetta, V. Vishwanath, M. Foad: "GIXRF and GEXRF analysis of PIII ultra shallow arsenic profiles in Silicon"; 15th Int. Conference on TXRF and related methods, Osaka, Japan; 23.09.2013 - 26.09.2013; oral
 15. D. Ingerle, G. Pepponi, F. Meirer, M. Schiebl, D. Giubertoni, E. Demenev, P. Wobrauschek, C. Strelti: "New approach for characterization of ultra-shallow implants by simultaneous evaluation of GIXRF and XRR"; ICXOM 2013, Hamburg, Germany; 02.09.2013 - 06.09.2013; poster
 16. M. Schiebl, D. Ingerle, C. Strelti, P. Wobrauschek: "Instrumental setup for simultaneous GIXRF and XRR measurement for Characterization of thin films on Si wafers"; ICXOM 2013, Hamburg, Germany; 02.09.2013 - 06.09.2013; poster
 17. B. Caby, E. Nolot, D. Chateigner, M. Morales, C. Strelti, G. Pepponi, P. Gergaud, L. Lutterotti, D. Ingerle, F. Brigidi: "XRR & GiXRF combined analysis of TCO/metal/TCO structures for photovoltaic applications"; 15th Int. Conference on TXRF and related methods, Osaka, Japan; 23.09.2013 - 26.09.2013; poster
 18. D. Ingerle, G. Pepponi, F. Meirer, E. Demenev, D. Giubertoni, C. Strelti: "Modelling shallow dopant distributions as layered samples for grazing

- incidence x-ray fluorescence analysis"; EXRS Conference, Vienna, Austria; 18.06.2012 - 22.06.2012; poster
19. D. Ingerle, G. Pepponi, F. Meirer, C. Strel, P. Wobrauschek, J. van den Berg, M. Reading: "Combined approach of GIXRF+XRR for Characterization of thin films on Si wafers"; TXRF 2011 Conference, Dortmund, Germany; 07.06.2011 - 09.06.2011; poster
 20. D. Ingerle, F. Meirer, N. Zöger, G. Pepponi, D. Giubertoni, P. Wobrauschek, C. Strel: "A GIXRF laboratory instrument for the characterization of ultra shallow implants and thin films"; ALTECH ECS Meeting, Wien; 04.10.2009 - 09.10.2009; oral
 21. D. Ingerle, N. Zöger, P. Wobrauschek, C. Strel, F. Meirer, G. Pepponi, D. Giubertoni: "Spectrometer For Grazing Incidence Xrf: Characterization Of As Implants And Hf Layers"; 58th Denver X-ray Conference, Colorado Springs; 27.07.2009 - 31.07.2009; oral
 22. D. Ingerle, F. Meirer, N. Zöger, G. Pepponi, D. Giubertoni, P. Wobrauschek, C. Strel: "Spectrometer for Grazing Incidence XRF: Characterization of As Implants and Hf Layer"; TXRF conference 2009, Goetheborg; 15.06.2009 - 19.06.2009; oral
 23. D. Giubertoni, G. Pepponi, B. Beckhoff, P. Hoenicke, S. Gennaro, F. Meirer, D. Ingerle, G. Steinhauser, M. Fried, P. Petrik, A. Parisini, M. Reading, C. Strel, J. van den Berg, M. Bersani: "Multi-technique characterization of arsenic ultra shallow junctions in silicon within the ANNA consortium"; Frontiers of Characterization and Metrology for Nanoelectronics, College of Nanoscale Science and Engineering, University at Albany, Albany, NY; 11.05.2009 - 15.05.2009; oral
 24. G. Pepponi, F. Meirer, D. Giubertoni, D. Ingerle, G. Steinhauser, C. Strel, P. Hoenicke, B. Beckhoff, M. Bersani: "Grazing Incidence x-ray fluorescence and secondary ion mass spectrometry combined approach for characterization of ultra shallow arsenic distribution in silicon"; International Workshop on INSIGHT in Semiconductor Device Fabrication, Metrology, and Modeling (INSIGHT-2009), Napa, CA, USA; 26.04.2009 - 29.04.2009; oral

Acknowledgements

Firstly, I would like to express my sincere gratitude to my advisor and group leader Dr. Christina Streli for encouragement and support, but also patience.

I am thankful to Dr. Peter Wobrauschek, who is still, despite being officially “im Ruhestand” (in retirement), a very enthusiastic and active member of the group, always ready to share his experience.

I want also to mention and express my gratitude to former members of the X-ray group, who worked with me and helped on the project, namely Dr. Norbert Zöger and Dr. Florian Meirer, as well as Dr. Giancarlo Pepponi, who often joined our discussions, when we were left wondering what is actually happening during the measurements.

I thank Dr. Peter Kregsamer for playing the role of *advocatus diaboli* and the ensuing fruitful discussions.

I would also like to extend my sincere gratitude to Dr. Klaudia Hradil and the X-ray Center for access to the instruments and provided equipment.

Special thanks also to all other members of the X-ray group at the Atominsti-
tut for support and assistance in time of need.

I owe my gratitude to my family, my wife and parents, for their continued support and patience.

Finally, I acknowledge the support of this work by the Austrian Science Fund (FWF), project number P 23832-N20.

Contents

1	Introduction	13
1.1	X-ray reflectivity	14
1.2	Grazing Incidence XRF	14
1.3	The ambiguity problem	15
1.4	Glancing incidence X-ray analysis	16
2	Fundamentals	19
2.1	Principles of Calculation	19
2.1.1	Atomic scattering factors	19
2.1.2	Refractive Index	21
2.1.3	X-ray Standing Wave	22
2.1.4	Calculation of GIXRF and XRR intensities	23
2.1.5	Roughness	28
2.1.6	Calculation examples	28
2.2	Coherence	29
2.3	Correction of instrumental effects	32
2.3.1	Angular divergence	32
2.3.2	Beam footprint	35
3	Instrumentation for combined measurements	38
3.1	GIXRF and XRR table-top vacuum spectrometer	39
3.2	Refitting an X-ray Diffraction System for combined GIXRF and XRR measurements	42
3.3	Comparison of measurements	46
3.3.1	Comparison of the table-top spectrometer with the Empyrean X-ray Diffraction System	46
3.3.2	Comparison of the table-top spectrometer with the XRF beamline of Elettra Sincrotrone Trieste	46
4	Evaluation	50
4.1	Optimization	50
4.2	Overview of available optimization algorithms	51
4.3	Comparison of optimization algorithms	53
4.3.1	Layers	53
4.3.2	Ion implanted samples	54

4.4	Software - JGIXA	58
4.4.1	XRF lines and measurement data	60
4.4.2	Setup parameters	62
4.4.3	Sample model	63
4.4.4	Fit and optimization algorithm	64
4.4.5	Data plot	65
4.4.6	Load and Save	65
5	Applications	67
5.1	Instrument characterization	67
5.2	Layers	68
5.2.1	Nickel layer	68
5.2.2	Titanium layer	68
5.2.3	In ₂ O ₃ and Ag layers	69
5.3	Ion implanted samples	71
5.3.1	Influence of Implanted Dose	72
5.3.2	Influence of Layer Model	72
5.3.3	Comparison with other techniques	73
5.3.4	Depth-sensitivity of the method	77
5.4	Nanoparticles	77
6	Concluding remarks	80
	References	82

1 Introduction

The research in Grazing Incidence XRF (GIXRF) and later in the combination with X-ray reflectivity (XRR), i.e. Glancing incidence X-ray analysis (GIXA), was not only motivated by scientific curiosity, but also driven by the requirements of the semiconductor industry. As the device size for semiconductor fabrication was reaching some tens of nanometers, it became clear that the dielectric constant of SiO_2 , which was used for the gate insulator of a Field-effect transistors, is no longer sufficient for reliable and efficient operation. Therefore, the semiconductor manufacturers commenced investigation of materials with higher dielectric constants (high-K materials) like HfO_2 . Moreover new implantation processes like plasma-immersion-ion-implantation (PIII) of arsenic for ultra-shallow-junctions (USJ) were also researched. The fabrication with these materials and processes require precise control of the film thickness and elemental composition, as well as precise information on implantation depth and implant distribution.

The research on the characterization of these samples with GIXRF was performed within the framework of the European Integrated Activity of Excellence and Networking for Nano and Micro- Electronics Analysis (ANNA), which was supported by the European Commission Research Infrastructure Action under the FP6 "Structuring the European Research Area" Programme. As it became apparent that GIXRF evaluations could be ambiguous, the technique was used as a complimentary technique to Secondary Ion Mass Spectrometry (SIMS), which used on its own also had difficulties with very shallow implantations.

After the end of the ANNA project the new goal was to advance the combination of GIXRF with XRR, which was part of a new project funded by the Austrian Science Fund (FWF). From the beginning the investigated samples during the previous project had influence on the design decisions for an enhanced spectrometer and the evaluation software. The measurement setup had to be flexible enough to allow the use of different incident energies (anode materials) for best possible excitation of the investigated sample and capable of vacuum operation to reduce the absorption of the produced XRF. For the software it implied fast calculation speed, as it should represent the implantation profile as a stack of very thin layers, which model the smoothly varying composition and optical properties. Additionally it should have a graphical user interface (GUI) and facilitate relatively simple operation, in order to encourage the adoption of GIXA.

The present thesis summarizes the work on GIXA within the framework of the FWF project P 23832-N20.

1.1 X-ray reflectivity

XRR is a non-destructive, highly accurate method used to determine thickness and roughness of thin layers - with thicknesses ranging from a few nanometers to some hundred nanometers - as well as the optical properties of the reflecting interfaces. XRR spectra are acquired by varying the incident angle in the grazing incidence regime while measuring the specular reflected X-ray beam.

In contrast to the widespread adoption nowadays, XRR had not a promising start historically. Röntgen in his paper relating the discovery of x-rays in 1895 stated that “no noticeable regular reflection of the rays takes place from any of the substances examined” [1]. Only decades later in 1922 Compton argued that due to the refractive index, which for x-rays is smaller than unity in matter, a beam should be totally reflected on a plane surface and this effect was in fact observed [2]. Arguably this could be seen as the starting point of the grazing incidence techniques and especially XRR. Some years later Prins investigated the influence of the wavelength on the reflection and included absorption in the refractive index for Fresnel’s formula [3]. In 1931 Kiessig investigated the distinct, periodic maxima and minima, which occurred in reflections from a thin nickel layer on glass. He explained these (“Kiessig”) fringes by interference of reflections on different interfaces and also perceived the link of the distance of the maxima and minima to the thickness of the film [4]. The groundwork for modern XRR analysis was finally laid by Parratt in a seminal paper by presenting a recursion formula for the calculation of reflections from layered structures [5] and the work of Croce et al. added the description of roughness to the theory [6]. Since then the technique has grown to a valuable and essential tool for the characterization of surfaces and layers.

1.2 Grazing Incidence XRF

GIXRF is a technique, which similar to XRR is non-destructive and uses an X-ray beam with varying incident angle in the grazing incidence regime. In this case not the reflected beam but the XRF originating in the sample is recorded in dependence on the incident angle of the primary beam. Due to the varying penetration depth and the interference of incident and reflected fields, the GIXRF spectrum shows variations and oscillations in the intensity, which are correlated to the depth distribution of the elements in the sample.

Historically the research for GIXRF was significantly slower and later than for XRR. Although there were publications dealing with the phenomenon of emission of X-rays by the X-Ray Evanescent-Wave [7] and under grazing angles [8] in the 1980s, it was not before the early 1990s, when de Boer (partly with van den Hoogenhof as co-author) published a seminal series of articles on TXRF and GIXRF of thin-layered samples, that the possibilities of this technique were thoroughly investigated. In these papers a detailed description and analysis of X-ray standing wave effects and the angle dependent measurement curves is given [9, 10, 11]. Also a detailed formalism for the calculation of the emitted fluorescence intensities was introduced [12]. During the following years they continued this series (partly with Leenaers) and presented the idea of a combined GIXRF and X-ray reflectometry (XRR) analysis and an instrument for this combined Glancing incidence X-ray analysis (GIXA) [13, 14, 15, 16]. But layer thicknesses and device sizes used in semiconductor device fabrication at this time were probably still too large, i.e. in the range of some hundred nanometers, to fully utilise the potential of this technique. Furthermore the calculation of emitted fluorescence intensities is quite complicated and thus was probably too time-consuming, for the computers at this time, to employ it in routine analysis.

About ten years later GIXRF was “rediscovered” by Pepponi et al. [17] as a complementary technique to SIMS for the analysis of ultra-shallow junctions. The measurements presented in this paper were carried out at a synchrotron beamline, as there was no suitable measurement chamber for the laboratory. Nowadays implantation depths and layer thicknesses for semiconductor device fabrication are in the range of some nanometers and thus seem ideally suited for GIXRF, which has its largest sensitivity on the surface and up to a few nanometer below it. Thus the idea was born to develop the knowledge of and instrumentation for GIXRF and to compare the performance of the technique with other methods. This was done within the European Integrated Activity of Excellence and Networking for Nano and Micro- Electronics Analysis (ANNA) from 2006 to 2011 [18, 19, 20, 21], which included several partners who are still working on GIXRF, specifically Fondazione Bruno Kessler, Trento (FBK), Physikalisch-Technische Bundesanstalt, Berlin (PTB) and Atominstitut, TU Wien (ATI).

1.3 The ambiguity problem

During the work on the ANNA project it became obvious that the evaluation of GIXRF data alone is not able to provide an unambiguous solution for concentration profiles in a material. In fact the determination of the concentration requires

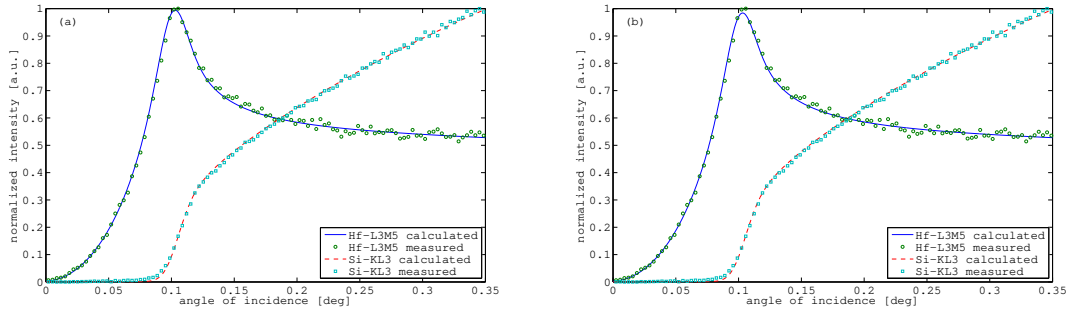


Figure 1: GIXRF fluorescence signal from Hf and Si from a HfSiO_x layer. The calculation was performed using only the GIXRF signal. Good fit results are obtained for a density of 6.1 g/cm³ using a thickness of 2.25 nm (a) as well as a density of 6.7 g/cm³ using a thickness of 2.05 nm (b), thus showing the ambiguity of the GIXRF data.

the solution of an ill-posed inverse problem.

Figure 1 shows as example the GIXRF results of the fluorescence radiation from Hf L₃-M₅ and Si K-L₃ from a nominal 2 nm thick Hf_{0.6}Si_{0.4}O₂ layer on a Si substrate. By fitting the thickness and the density, the results are ambiguous: A set of combinations density-thickness can be found resulting in good fitting, for demonstration 2 combinations were selected. Very good fitting results can be obtained for a thickness of 2.25 nm with a density of 6.1 g/cm³ (Figure 1a), but also for a thickness of 2.05 nm with a density of 6.7 g/cm³ (Figure 1b).

The same ambiguity also exists for ion implantation profiles. Figure 2a and Figure 2b show the results of a fitting to GIXRF data using two very different arsenic depth profiles (Figure 2c and Figure 2d). The simulation and optimization of the sample parameters was performed following the procedures described in detail in chapter 2 and chapter 4. Although the agreement between simulated and measured As and Si GIXRF signals is equally good for both depth profiles, the distribution shown in 2c is physically unrealistic.

However, when introducing the XRR measurement and simulations (Figure 3) based on the profiles in Figure 2c and Figure 2d, only the profile shown in Figure 2d leads to an excellent agreement between GIXRF and XRR data. Here it has to be noted that using only the XRR data is also not sufficient to determine the depth profile because also the fit to the collected XRR data has no unique solution. [22, 23, 24]

1.4 Glancing incidence X-ray analysis

As mentioned before the combined analysis of different X-ray techniques, was proposed and investigated in 1993 by van den Hoogenhof et al. [15], but already

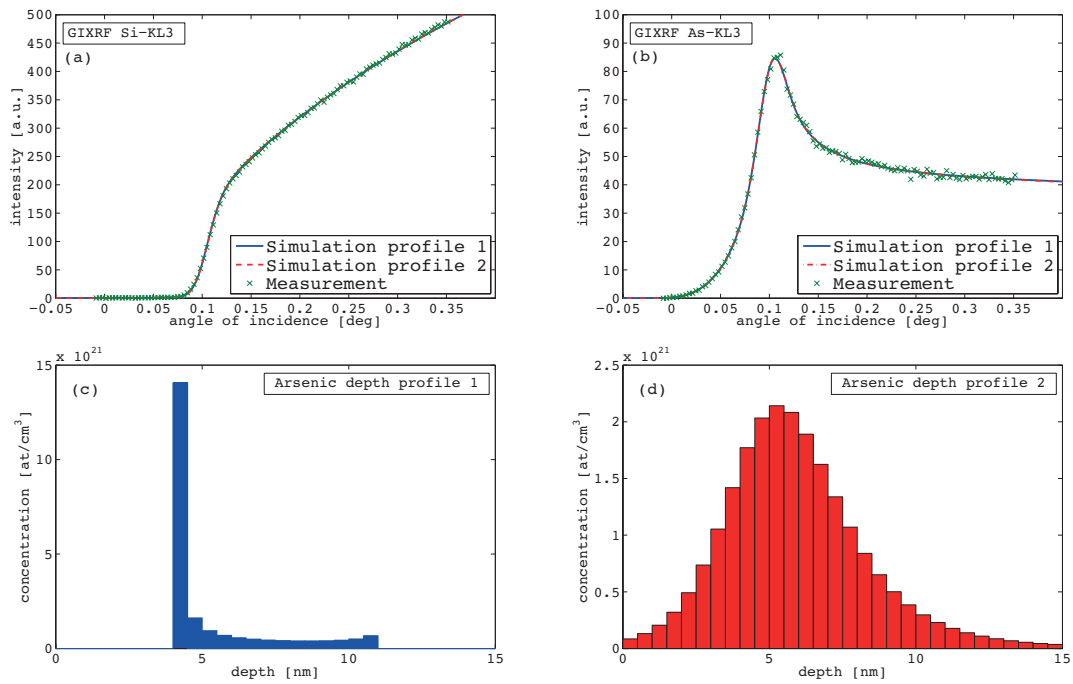


Figure 2: (a) GIXRF Silicon bulk signal (fitted and experimental), (b) GIXRF Arsenic implant signal (fitted and experimental), and (c and d) assumed Arsenic depth profiles for the GIXRF simulation in (a) and (b).

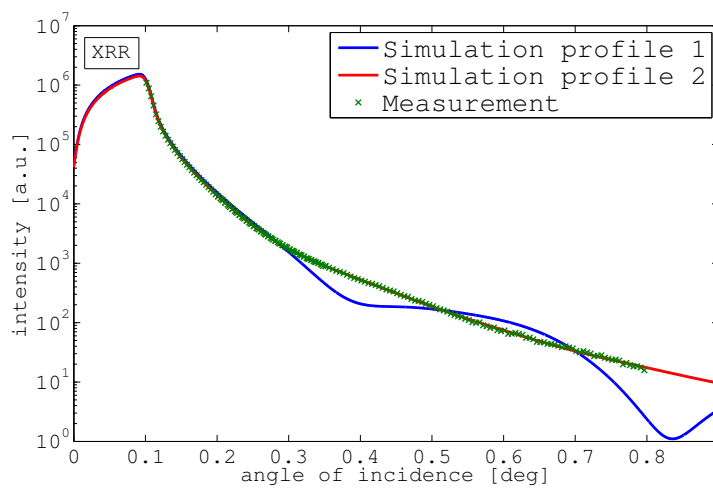


Figure 3: Measured and simulated XRR signal for the profiles shown in Figure 2c and Figure 2d.

one year later in 1994 the same authors posed the question “Glancing incidence X-ray analysis: Forgotten or to be discovered?” [16]. And it really seems like GIXA had to be rediscovered, as in the last few years a lot of activity, besides our own efforts, has started in the field of GIXA.

On the software side there are now several packages under more or less active development, some with slightly different focus: Tiwari et al. published CATGIXRF [25] for calculations, which was just recently improved with a GUI [26]; Brigidi and Pepponi published the GIMPY software [27], which offers the possibility to simulate and fit a whole EDXRF spectrum at each angle step; Bortolotti and Lutterotti added, with support by Pepponi, calculations of XRF intensities to the XRD Rietveld refinement software MAUD [28]; Lühl et al. presented their MARS software in the poster session of the European Conference on X-Ray Spectrometry (EXRS) 2014 [29]; Detlefs et al. [30] created MedePy and presented it at the 16th International Conference on Total Reflection X-ray Fluorescence Analysis and Related Methods (TXRF 2015); additionally we know of a software which has been developed for the International Atomic Energy Agency (IAEA), but was not yet, to the best of our knowledge, published or presented.

Similarly, there was also a lot of recent activity on the instrumentation side, but mainly at the synchrotrons. Tiwari et al. [31] performed measurements at the B16 Test beamline at Diamond Light Source and Tiwari now continues this work with Das et al. at BL-16 beamline of Indus-2 [32]. Furthermore measurement chambers were developed in a cooperation of PTB and TU Berlin[33]. Relatively similar instruments are now available at the XRF beamline of Elettra Sincrotrone Trieste[34], the metrology beamline of SOLEIL [35] and at the X-ray innovation laboratory BLiX (TU Berlin), whereas the original instrument at the PTB laboratory at BESSY II[36] is somewhat larger.

2 Fundamentals

The methodology of GIXRF and XRR measurements is based on the principle of irradiating a flat and smooth sample under a small glancing angle by a primary X-ray beam and measuring the resulting secondary radiation after the interaction with the matter of the sample. The evaluated radiation may be different for the two techniques, i.e. we use the produced characteristic X-ray fluorescence for GIXRF and the specular reflected beam for XRR, but the interaction processes occurring in the sample are the same.

In the incident energy range of 1 keV to 30 keV, which is typically used for our experiments, the dominant interaction processes are scattering from the bound electrons and photoelectric absorption. Our treatment of these processes is based on the well documented and tabulated atomic scattering factors, from which one can directly derive properties like refractive index and mass attenuation coefficient of a material. These properties can then be used to calculate the intensities for GIXRF and XRR simulations.

2.1 Principles of Calculation

2.1.1 Atomic scattering factors

In sufficient distance from the source the electromagnetic radiation, which represents our primary beam at position \vec{r} , can be written as a plane wave with wave vector \vec{k} :

$$\vec{E}_i = \vec{E}_0 \exp \left[i \left(\omega t - \vec{k} \vec{r} \right) \right] \quad (1)$$

If this incident field is scattered by a free electron, due to oscillations of the electron in the field, the scattered electric field at an angle Θ to the polarization direction can be written as:

$$E_s = -E_0 \frac{r_e \sin \Theta}{r} \exp [i (\omega t - kr)] = -E_0 \frac{r_e \sin \Theta}{r} \exp \left[i \omega \left(t - \frac{r}{c} \right) \right] \quad (2)$$

where r_e is the classical electron radius [37, 38]. This is a scalar field, as only the scalar transverse component of acceleration contributes.

In the case of scattering by the electrons of an atom then, the complex atomic scattering factor

$$f = f_1 + i f_2 \quad (3)$$

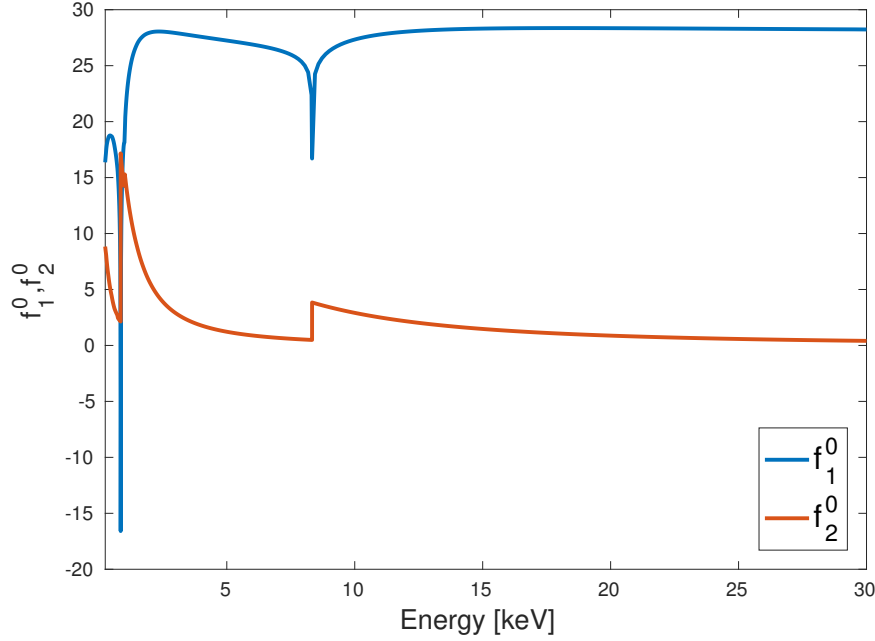


Figure 4: The angle-independent forward atomic scattering factor components f_1^0 and f_2^0 of Nickel. (data from [39])

is the factor by which one must multiply the amplitude scattered by a single free electron to yield the total amplitude coherently scattered by the particular atom:

$$E_s = -E_0 \frac{r_e \sin \Theta}{r} f(\Delta \vec{k}, \omega) \exp \left[i\omega \left(t - \frac{r}{c} \right) \right] \quad (4)$$

In the general case f depends on the on the energy of the incident radiation and on the scattering vector

$$\Delta \vec{k} = \vec{k}_s - \vec{k}_i \quad (5)$$

where \vec{k}_s and \vec{k}_i are the wavevectors of the scattered and incident wave. The wavevectors \vec{k}_s and \vec{k}_i are equal in magnitude $\frac{\omega}{c}$ and form an isocles triangle with the angle 2θ so that:

$$\left| \Delta \vec{k} \right| = 2k_i \sin \theta = \frac{4\pi}{\lambda} \sin \theta = q \quad (6)$$

which defines the magnitude q of the scattering vector.

In the limit of small scattering angles and/or for wavelengths that are comparable with atomic dimensions the atoms within a condensed system scatter as dipoles and the atomic scattering factors become independent of the scattering

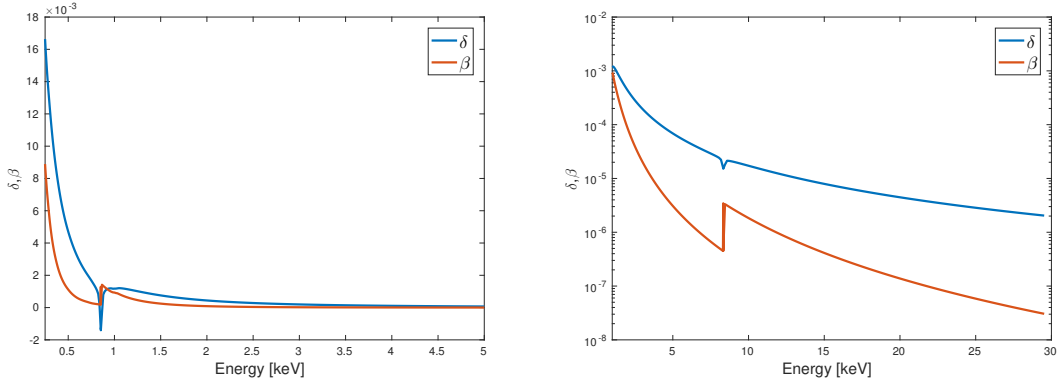


Figure 5: Refractive index of Nickel from 250 to 30,000 eV. (split in two parts for clarity)

vector, but not of the energy. The angle-independent forward atomic scattering factor components f_1^0 and f_2^0 are tabulated, e.g. by Henke et al. [39] for energies from 50 to 30,000 eV. Figure 4 shows as an example the forward atomic scattering factor for Nickel. These tabulated values are quite accurate in regions not too close to the absorption edges, but care must be taken when measuring in the X-ray absorption fine structure (XAFS) region. The tabulated scattering factors are calculated for individual atoms, assuming that the scattering is essentially unaffected by the condensed state of the system. Thus they do not and actually can not take into account the modulations due to neighbouring atoms, bonding and chemical state as observed in the XAFS case.

Incoherent Compton scattering is always zero for $\theta = 0$ and is proportional to $\sin^2 \theta$ for small angles [40] and thus can be neglected in our considerations.

2.1.2 Refractive Index

The refractive index of an arbitrary material can now be determined by summing over the scattering contributions of the individual atoms:

$$n = 1 - \delta - i\beta = 1 - \frac{r_e}{2\pi} \lambda^2 \sum_q n_q (f_1^0 + i f_2^0) \quad (7)$$

where n_q is the number of atoms of type q per unit volume [41, 39].

The real part δ , which measures the deviation of the real component from unity, is quite small, but for the most part positive (see Figure 5), and this results in a real part of the refractive index smaller than unity. A consequence of this fact is the existence of the phenomenon of total *external* reflection of X-rays at small angles of incidence.

The imaginary component β is a measure of the attenuation and can be related

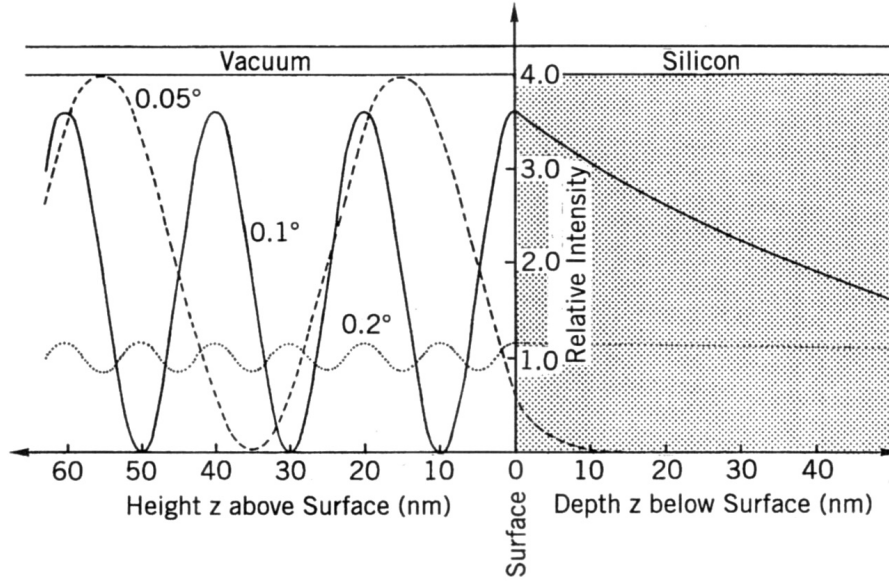


Figure 6: X-Ray intensities above (within the standing wave field) and below a thick Si-flat calculated for different angles of incidence. It can be seen that the dependence of the distance between nodes and antinodes is a function of the incident angle. Inside the medium, the intensity decreases as a function of the refraction angle.[41]

to the mass attenuation coefficient (μ/ρ) [41, 38]:

$$\beta = \frac{\lambda}{4\pi} \left(\frac{\mu}{\rho} \right) \rho \quad (8)$$

where ρ is the density.

The critical angle of total reflection can be approximated by the relation

$$\alpha_{crit} \approx \sqrt{2\delta} \quad (9)$$

which gives values between 0.04° and 0.6° for media and X-ray energies as typically used in GIXRF and XRR.

2.1.3 X-ray Standing Wave

In GIXRF the primary intensity in and above the reflecting surface appears as an evanescent wave field or as a X-ray standing wave field (XSW) with locally dependent fluctuations (Figure 6). The intensity of the fluorescence radiation emitted by atoms which are excited by these fields is direct proportional to the wave field intensity. Therefore the fluorescent signal emitted by a sample refers to the varying field intensity of the standing or evanescent wave field within the sample. Moreover it additionally provides information on the elemental composition of the sample. As the distribution of nodes and antinodes of the standing

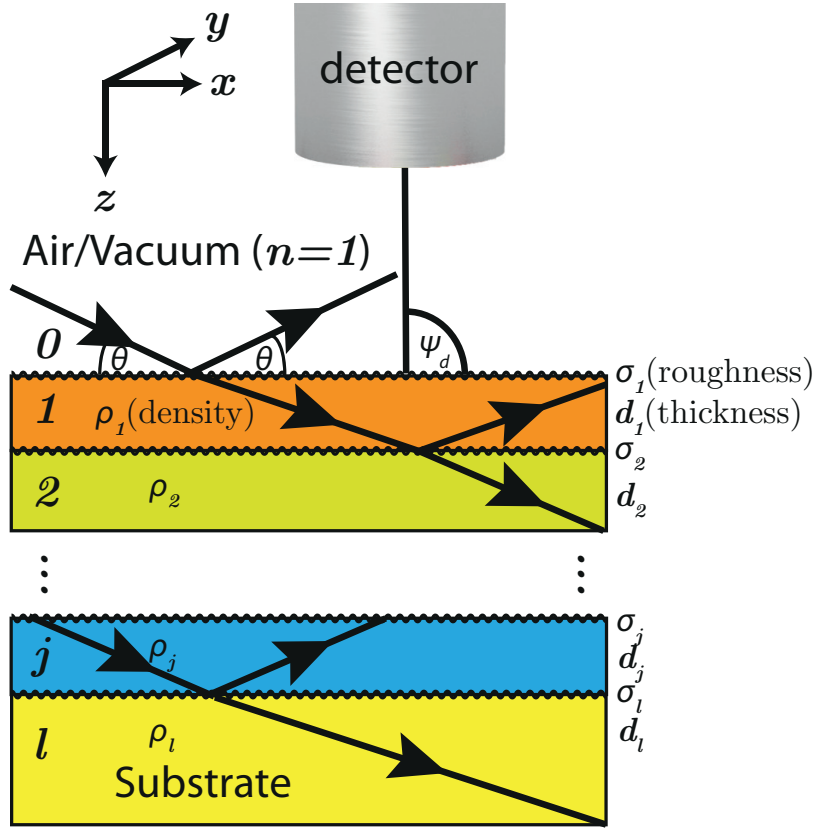


Figure 7: The layer model, which is used for GIXRF and XRR calculations.

wave field within and above the surface is a function of the incident angle of the primary radiation, the (consequently angle dependent) fluorescence signal can be used for nondestructive depth profiling of layered structures or for size determination of particles on the surface.

2.1.4 Calculation of GIXRF and XRR intensities

The formalism and theory for the calculation of GIXRF intensities has been described in several publications [42, 43, 12, 44, 45, 25, 41]. We will give here a concise but thorough introduction to the formalism, which largely follows the approach of de Boer [12], which is the most complete in our view. Figure 7 shows the layer model, which we use for our calculations.

The XRR intensity ensues inherently in the GIXRF calculation, as it is simply the total reflected intensity, which is calculated anyway.

We calculate intensities for s polarization only, as in the typically considered incident energy range of ~ 1 to 30 keV δ and β are small enough, that the result for p polarization is identical [12].

The number of fluorescence photons created in a material by atoms of a par-

ticular element a per unit time for incident radiation of wavelength λ can be obtained from fundamental parameters and the number of absorbed photons, which is obtained by dividing the absorbed energy P by $\frac{hc}{\lambda}$:

$$I_a = C_a \frac{S_{a\lambda}}{\mu_\lambda} \frac{\lambda}{hc} P \quad (10)$$

where C_a is the mass fraction of element a in the material, μ_λ is the mass absorption coefficient of the material and $S_{a\lambda}$ is a sensitivity value of element a at wavelength λ :

$$S_{a\lambda} = \tau_{a\lambda} J_{a\lambda} \omega_a g_a \quad (11)$$

where $\tau_{a\lambda}$ is the photoelectric part of the mass absorption coefficient, $J_{a\lambda}$ is the jump factor at the relevant absorption edge, ω_a is the fluorescence yield and g_a is the relative emission rate.

We can use Poynting's theorem to calculate the amount of electromagnetic energy absorbed per unit time within a volume bounded by a surface ∂V with

$$P = - \oint_{\partial V} d\vec{f} \vec{S} \quad (12)$$

where \vec{S} is the, in our case time-averaged, energy flux density (Poynting vector):

$$\vec{S} = \frac{1}{2} \text{Re} \left(\vec{E} \times \vec{H}^* \right) \quad (13)$$

From equation (12) we can calculate the energy absorbed in a layer with infinitesimal thickness dz and bounded on top and bottom by a surface area A_d to be:

$$dP = -A_d \frac{\partial S_z}{\partial z} dz \quad (14)$$

For further calculations in a specific layer j we introduce the complex 'vectorial refractive index' [46, 47] or refraction vector [48] \vec{N}_j with its relation to the wave vector \vec{k}_j :

$$\vec{N}_j = \vec{N}'_j - i\vec{N}''_j = \frac{\lambda}{2\pi} \vec{k}_j \quad (15)$$

Furthermore it can be shown [47] from Maxwell's equations for the dielectric constant ϵ_j :

$$\left(\vec{N}'_j - i\vec{N}''_j\right)^2 = \epsilon_j = \epsilon'_j - i\epsilon''_j \approx 1 - 2\delta_j - i2\beta_j \quad (16)$$

for small δ_j and β_j . This helps us to establish a relation to the scattering factors. In our specific layer model we also find the following relations:

$$N_{jx} = \cos \theta \quad (17)$$

and

$$N_{jz} = \sqrt{\epsilon_j - \cos^2 \theta} \quad (18)$$

The total electric field for our energy flow (equation (13)) is the sum of a transmitted and a reflected contribution in y direction (s polarization):

$$\begin{aligned} E_{jy} &\equiv E_j = E_j^\downarrow + E_j^\uparrow \\ &= E_j^t \exp\left[-i\frac{2\pi}{\lambda}N_{jz}z\right] \exp\left[i\left(\omega t - \frac{2\pi}{\lambda}N'_{jx}x\right)\right] \\ &\quad + E_j^r \exp\left[i\frac{2\pi}{\lambda}N_{jz}z\right] \exp\left[i\left(\omega t - \frac{2\pi}{\lambda}N'_{jx}x\right)\right] \end{aligned} \quad (19)$$

where E_j^t and E_j^r are the amplitudes of the transmitted and reflected field, which we will determine later with the Fresnel equations (equation (36), equation (37)).

The components of the magnetic field can be calculated from \vec{E}_j using Maxwell's equation:

$$\vec{\nabla} \times \vec{E}_j = -\mu_0 \frac{\partial H_j}{\partial t} \quad (20)$$

which yields:

$$H_{jx} = \sqrt{\frac{\epsilon_0}{\mu_0}} \left(E_j^\uparrow - E_j^\downarrow\right) N_{jz} \quad (21)$$

$$H_{jy} = 0 \quad (22)$$

$$H_{jz} = \sqrt{\frac{\epsilon_0}{\mu_0}} \left(E_j^\uparrow + E_j^\downarrow\right) N_{jx} \quad (23)$$

and for the components of the Poynting vector:

$$S_{jx} = \frac{1}{4} E_{jy}^* H_{jz} + c.c. = \frac{1}{2} \sqrt{\frac{\epsilon_0}{\mu_0}} |E_j^\uparrow + E_j^\downarrow|^2 \cos \theta \quad (24)$$

$$S_{jy} = 0 \quad (25)$$

$$S_{jz} = -\frac{1}{4} E_{jy}^* H_{jx} + c.c. = \frac{1}{4} \sqrt{\frac{\epsilon_0}{\mu_0}} (E_j^\downarrow + E_j^\uparrow)^* (E_j^\downarrow - E_j^\uparrow) N_{jz} + c.c. \quad (26)$$

After inserting and differentiating we find:

$$\begin{aligned} -\frac{\partial S_{jz}}{\partial z} &= \sqrt{\frac{\epsilon_0}{\mu_0}} \frac{2\pi}{\lambda} N'_{jz} N''_{jz} \left(|E_j^t|^2 \exp \left[-\frac{4\pi}{\lambda} N''_{jz} z \right] \right. \\ &\quad \left. + |E_j^r|^2 \exp \left[\frac{4\pi}{\lambda} N''_{jz} z \right] \right. \\ &\quad \left. + E_j^{t*} E_j^r \exp \left[\frac{4\pi i}{\lambda} N'_{jz} z \right] + c.c. \right) \end{aligned} \quad (27)$$

Inserting in equation (10), our starting point for the intensity, and adding absorption for the created XRF for a detection angle ψ_d , we find for atoms of a particular element a in layer j :

$$I_{aj} = C_a \frac{S_{a\lambda}}{\mu_{j\lambda}} \frac{2\pi}{hc} A_d \sqrt{\frac{\epsilon_0}{\mu_0}} N'_{jz} N''_{jz} \exp \left[-\sum_{n=1}^{j-1} \frac{\mu_{na} d_n}{\sin \psi_d} \right] \quad (28)$$

$$\times \left\{ |E_j^t|^2 \int_0^{d_j} dz \exp \left[-\left(\frac{4\pi}{\lambda} N''_{jz} + \frac{\mu_{ja}}{\sin \psi_d} \right) z \right] \right. \quad (29)$$

$$\left. + |E_j^r|^2 \int_0^{d_j} dz \exp \left[\left(\frac{4\pi}{\lambda} N''_{jz} - \frac{\mu_{ja}}{\sin \psi_d} \right) z \right] \right. \quad (30)$$

$$\left. + \text{Re} \left(2E_j^{t*} E_j^r \int_0^{d_j} dz \exp \left[\left(\frac{4\pi i}{\lambda} N'_{jz} - \frac{\mu_{ja}}{\sin \psi_d} \right) z \right] \right) \right\} \quad (31)$$

and after performing the integration:

$$I_{aj} = C_a \frac{S_{a\lambda}}{\mu_{j\lambda}} \frac{2\pi}{hc} A_d \sqrt{\frac{\epsilon_0}{\mu_0}} N'_{jz} N''_{jz} \exp \left[- \sum_{n=1}^{j-1} \frac{\mu_{na} d_n}{\sin \psi_d} \right] \quad (32)$$

$$\times \left\{ |E_j^t|^2 \frac{1 - \exp \left[- \left(\frac{4\pi}{\lambda} N''_{jz} + \frac{\mu_{ja}}{\sin \psi_d} \right) d_j \right]}{\frac{4\pi}{\lambda} N''_{jz} + \frac{\mu_{ja}}{\sin \psi_d}} \right. \quad (33)$$

$$+ |E_j^r|^2 \frac{1 - \exp \left[\left(\frac{4\pi}{\lambda} N''_{jz} - \frac{\mu_{ja}}{\sin \psi_d} \right) d_j \right]}{-\frac{4\pi}{\lambda} N''_{jz} + \frac{\mu_{ja}}{\sin \psi_d}} \quad (34)$$

$$\left. + \operatorname{Re} \left(2E_j^{t*} E_j^r \frac{1 - \exp \left[\left(\frac{4\pi i}{\lambda} N'_{jz} - \frac{\mu_{ja}}{\sin \psi_d} \right) d_j \right]}{-\frac{4\pi i}{\lambda} N'_{jz} + \frac{\mu_{ja}}{\sin \psi_d}} \right) \right\} \quad (35)$$

Finally to determine the field amplitudes E_j^t and E_j^r we use the Fresnel equations for s polarization [12, 49]:

$$r_j = \frac{N_{jz} - N_{j+1,z}}{N_{jz} + N_{j+1,z}} = \frac{k_{jz} - k_{j+1,z}}{k_{jz} + k_{j+1,z}} \quad (36)$$

$$t_j = \frac{2N_{jz}}{N_{jz} + N_{j+1,z}} = \frac{2k_{jz}}{k_{jz} + k_{j+1,z}} \quad (37)$$

and apply a recursive algorithm, going through all the layers:

$$E_{j+1}^t = \frac{a_j E_j^t t_j}{1 + a_{j+1}^2 X_{j+1} r_j} \quad (38)$$

$$E_j^r = a_j^2 X_j E_j^t \quad (39)$$

where

$$a_j = \exp \left[- \frac{2\pi i}{\lambda} N_{jz} d_j \right] \quad (40)$$

$$X_j = \frac{r_j + a_{j+1}^2 X_{j+1}}{1 + a_{j+1}^2 X_{j+1} r_j} \quad (41)$$

For the substrate there is no bottom layer and no reflection, i.e. $E_l^r = X_l = 0$, thus we can start from the substrate and calculate the amplitudes for all layers.

The normalized XRR intensity is the reflected intensity at the surface:

$$I_{XRR} = |E_0^r|^2 \quad (42)$$

The complete calculation for a measurement of a layered sample now consists of summing the respective XRF intensities for all layers and repeat this procedure for all measured angles.

2.1.5 Roughness

The treatment and inclusion of roughness is an essential part in the analysis of XRR and GIXRF, as virtually any sample will have surface or interfacial roughness. The roughness is typically represented by a value σ_j , which represents the root-mean-square (r.m.s) of the vertical deviations. There exist two well-known methods to include roughness in the GIXRF formalism, which basically derive from models in XRR calculations [12, 49].

In the first approach only r_j [6, 50, 49] or r_j as well as t_j [43] from the Fresnel equations (equation (36), equation (37)) are multiplied by a factor S_j and T_j respectively. An expression, which gives good results [12, 25] is:

$$S_j = \exp \left[-2 \left(\frac{2\pi\sigma_j}{\lambda} \right)^2 N_{jz} N_{j+1,z} \right] \quad (43)$$

$$T_j = \exp \left[\frac{1}{2} \left(\frac{2\pi\sigma_j}{\lambda} \right)^2 (N_{jz} - N_{j+1,z})^2 \right] \quad (44)$$

In a second method the rough interface between two layers is represented by a series of transition layers with smoothly varying refractive index. This approach may be more accurate, but is also more expensive in terms of computation time, as it introduces additional layers to the simulation. Thus for small roughness of some nanometers the first approach is preferred, as it is accurate enough.

2.1.6 Calculation examples

Figure 8 shows the results of calculations for the angle dependent fluorescence intensity emitted from a layer on Silicon substrate. It can be seen, that the curves of the ultra-thin Co layers are similar to those of non-reflecting layers. The maxima of those layers are located at the critical angle of Silicon (1.78 mrad for 17.5 keV excitation energy). These maxima are shifted towards the critical angle of Co (3.35 mrad for 17.5 keV excitation energy) for layers thicker than 10 nm. The reason is that for nanometer-thin Co-layers the radiation penetrates the film and total reflection occurs at the Si-substrate exclusively. For films thicker than about 10 nm the curves show oscillations of intensity above the critical angle of Co. These fluctuations are correlated to the Kiessig maxima and minima of the reflectivity of the layered sample [41, 14].

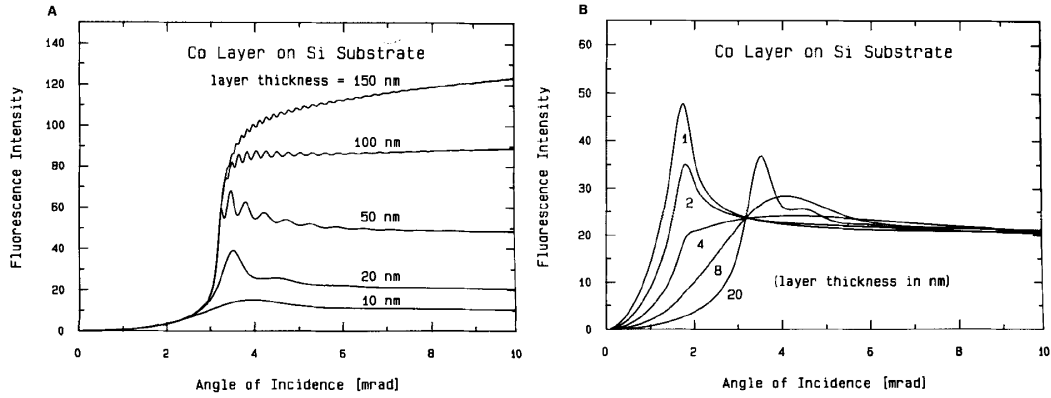


Figure 8: (A) Calculated fluorescence intensities as a function of incident angle for different layer thicknesses of Co on a Silicon reflector. Excitation energy: Mo-K α (17.5 keV). (B) as in (A), but fluorescence radiation normalized to the intensities at large angles of incidence.[51]

2.2 Coherence

A monochromatic and parallel beam would represent a perfect plane wave with perfect coherence and thus the extent of the XSW would only be limited by the beamsize. This is obviously an idealization as a real x-ray beam is not perfectly monochromatic and it does not propagate in a perfectly well defined direction, i.e. the beam has a energy/wavelength distribution, which is determined by the source type and the monochromator, and it has an angular divergence, due to source size and slit width. A means to estimate the coherence of a wave is the coherence length, which is the propagation distance over which a coherent wave maintains a specified degree of coherence. Wave interference is strong when the paths taken by all of the interfering waves differ by less than the coherence length. A wave with a longer coherence length is closer to a perfect sinusoidal wave.

The longitudinal coherence limits the interference of waves, which are propagating in the same direction, but have different wavelengths. The corresponding longitudinal coherence length can be defined as [52]:

$$L_L = \frac{1}{2} \frac{\lambda^2}{\Delta\lambda} \quad (45)$$

Similarly the transversal coherence limits the interference of waves of the same wavelength, but with slightly different directions of propagation separated by an angle of $\Delta\theta$. The corresponding transversal coherence length can be defined as [52]:

$$L_T = \frac{1}{2} \frac{\lambda}{\Delta\theta} \quad (46)$$

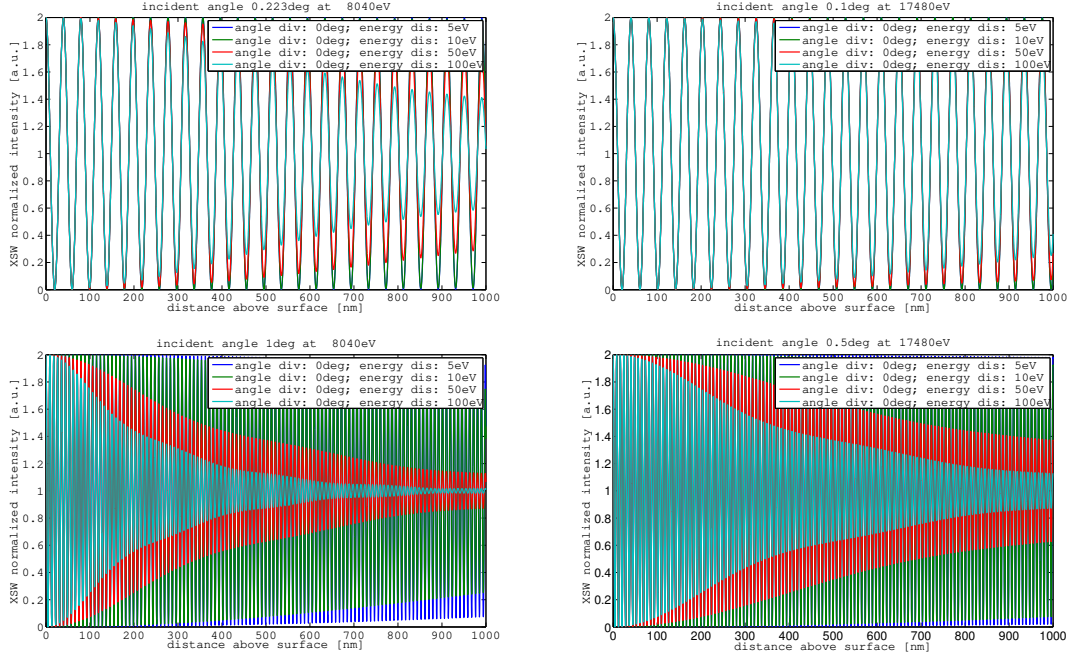


Figure 9: Graphical representation of XSW intensities for a lorentzian distribution of the primary beam energy with a FWHM of 5, 10, 50 and 100 eV. The respective coherence lengths are: 15273, 7636, 1527, 764 nm at 0.223 deg and 3406, 1703, 340, 170 nm at 1 deg for 8040eV (Cu-K α , $\lambda = 0.154$ nm); 35694, 17847, 3569, 1785 nm at 0.1 deg and 7139, 3569, 714, 357 nm at 0.5 deg for 17480eV (Mo-K α , $\lambda = 0.071$ nm).

The coherence of the XSW was investigated by von Bohlen et al. [53] and they proceeded to determine the coherence length of the XSW by directly plugging the wavelength of the incident radiation in the equation for the coherence length. At first glance this seems natural, but may not really be what we want, since we want to determine the influence of the incident wavelength on the longitudinal coherence of the fringes of the XSW and not directly the coherence of the incident beam.

The period h of the interference fringes of the XSW is dependent on the incident angle θ and can be approximated for small angles:

$$h = \frac{\lambda \sin(\theta)}{1 - \cos(2\theta)} \approx \frac{\lambda}{2\theta} \quad (47)$$

If we use this period, which is actually the wavelength of the XSW in the equation for the longitudinal coherence length we get for variation of λ :

$$L_{L,\lambda}^{XSW} = \frac{1}{2} \frac{h^2}{\Delta h} = \frac{1}{2} \frac{\left(\frac{\lambda}{2\theta}\right)^2}{\frac{\Delta \lambda}{2\theta}} = \frac{1}{4} \frac{\lambda^2}{\theta \Delta \lambda} \quad (48)$$

The new expression in equation (48) is dependent on the incident angle θ and

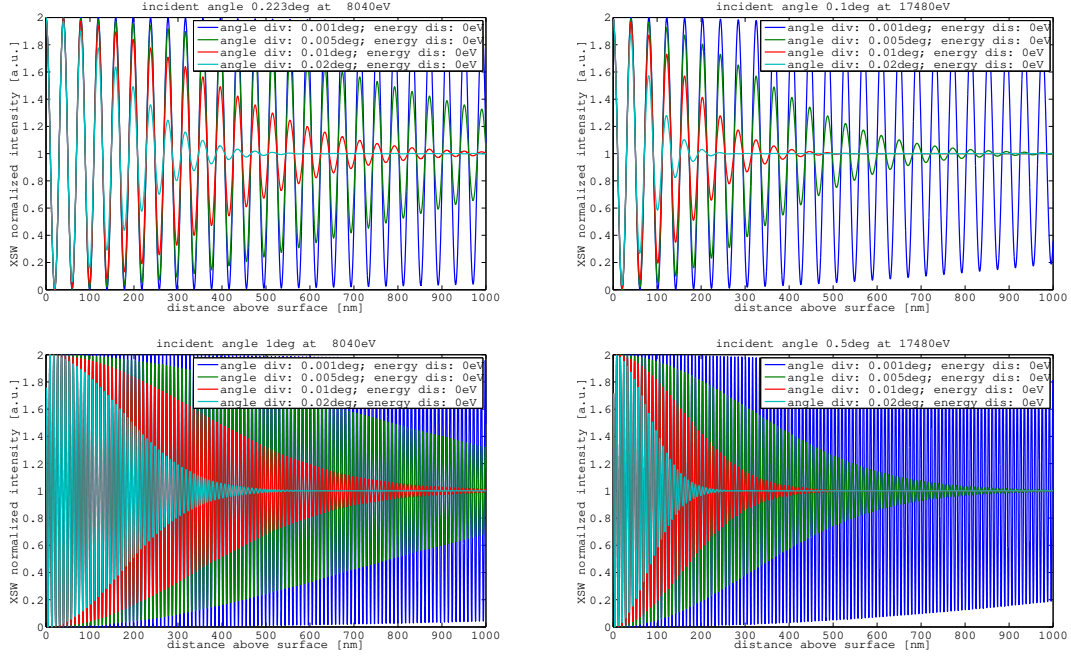


Figure 10: XSW intensities for a gaussian distribution of the incident angle with a FWHM of 0.001, 0.005, 0.01 and 0.02 deg. The corresponding coherence lengths are 4420, 884, 442, 221 nm for 8040eV (Cu-K α , $\lambda = 0.154$ nm) and 2032, 406, 203, 102 nm for 17480eV (Mo-K α , $\lambda = 0.071$ nm).

will be smaller for larger angles, but at the same time values will be overall larger than from equation (45), as the angles are typically very small. And in fact if we look at Figure 9, which was created by a superposition of waves according to equation (47) with varying λ , we see an angle dependence and good coherence for an energy distribution in the range of natural linewidths.

Figure 10, which was created for an angular divergence, shows as expected only a wavelength/energy dependence. For a divergence of 0.01 to 0.02 degree, which is quite typical for a measurement setup, there is already very noticeable dampening at 100 to 200 nm above the surface. Under these conditions this is a natural limitation for the layer thickness or nanoparticle size, which can be expected to show fringes or oscillations.

Thus our conclusion is that for measurement setups using characteristic x-rays with a natural linewidth of some eV from a tube and a multilayer or even crystal monochromator, the influence of angular divergence seems more critical and has to be considered in the simulation, especially for harder X-rays like Mo-K α .

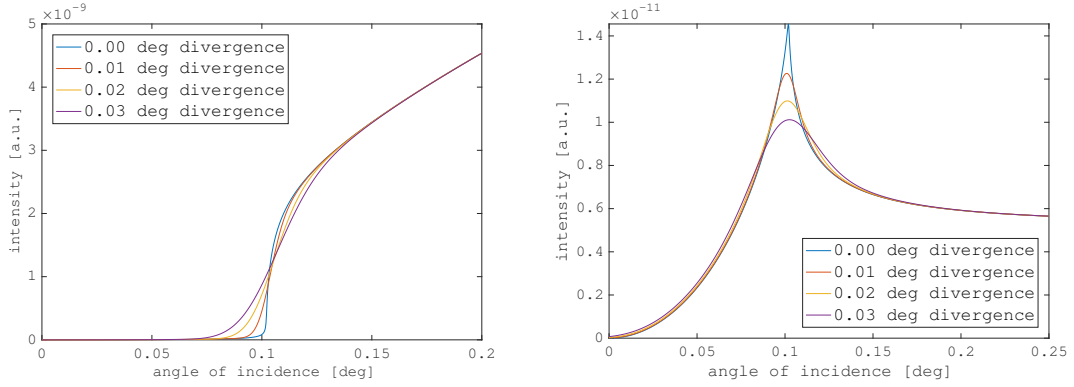


Figure 11: Influence of angular divergence on GIXRF scans of a bulk material (left) or a very thin layer (right).

2.3 Correction of instrumental effects

In modeling and fitting of a real experimental result, the instrumental effects have to be considered in the calculation. Two main influences have been identified: the angular beam divergence (transversal coherence) of the incident beam, as well as the beam footprint on the sample. Longitudinal coherence can be neglected for a primary beam of sufficiently monochromatized radiation (see section 2.2 and [54]). In our model the angular distribution of the incident beam is always approximated by a Gaussian shape, while the beam footprint, which represents the energy flux distribution on the surface of the sample, can be modeled as a Gaussian, a triangular, or a box-like distribution profile, depending on the X-ray source used in the experiment (e.g. lab source or synchrotron radiation).

2.3.1 Angular divergence

Because the beam used in a real measurement setup is not perfectly parallel but shows angular divergence, a certain range of incident angles has to be considered at each measurement point of the GIXRF scan. The influence of the angular divergence is considered in the calculation by convoluting the perfect theoretical curve with a Gaussian distribution, i.e. by calculating the sum of neighboring angles, weighted by a Gaussian distribution with a cutoff at 3 sigma, for each angle position. It has to be emphasized, that in general one has to use different values of angular divergence for the calculation of the GIXRF and XRR signals, because the reflected beam is usually shaped by additional optics in front of the XRR detector, which typically leads to a smaller divergence. Figure 11 and Figure 12 demonstrate the effect, which the angular divergence has on the GIXRF and XRR scans. In general it can be stated, that the divergence leads to a smoothing and

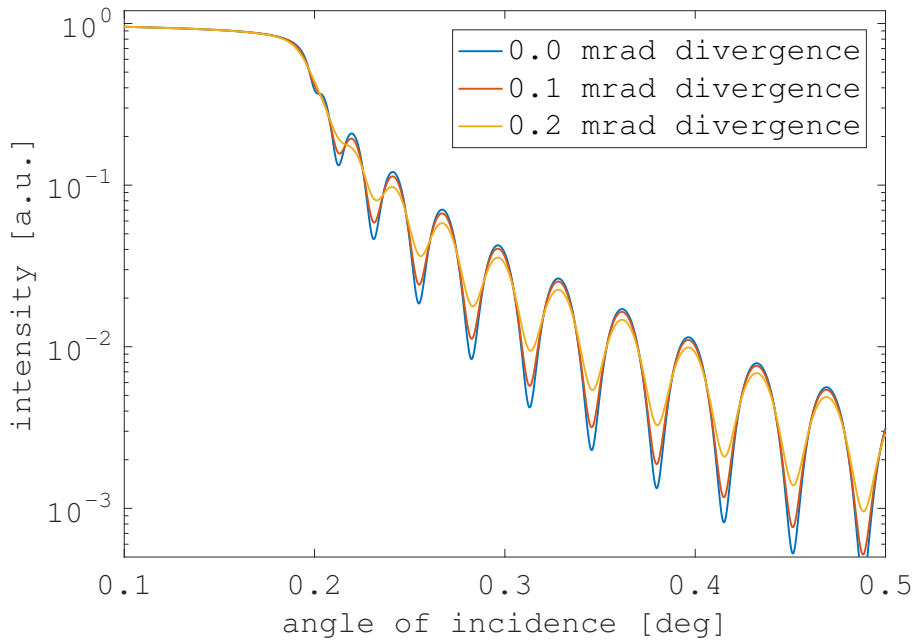


Figure 12: Influence of angular divergence on XRR scans.

dampening of the features.

In order to include the divergence effect as accurately as possible in the calculation, the software adjusts the number of calculation points per degree depending on the actual beam divergence. It calculates at least 150 points in the considered range of the Gaussian distribution or, in the case of a very large divergence, a lower limit of 5000 points per degree is used. The differences in the result for an assumed divergence of 0.02 degree and a varying number of steps per degree are shown in Figure 13. It becomes obvious that a smaller number of calculation points can lead to systematic errors in the evaluation, namely shifted maxima and minima in the XRR signal. By assuring a sufficient number of calculation points per degree the error of the simulation is expected to be significantly smaller than the experimental error, improving the accuracy of the fitting parameters.

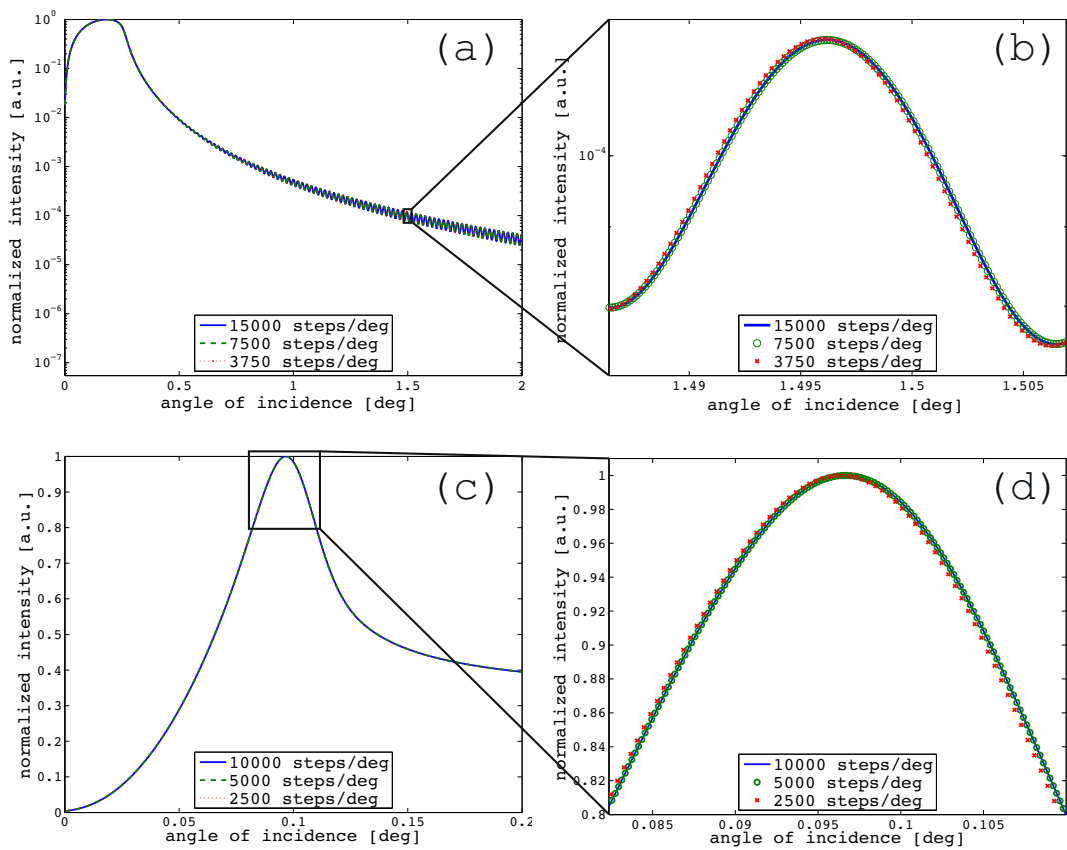


Figure 13: (a) XRR simulation of 100nm Au on Si; (b) The enlargement of one fringe shows a deviation for the calculation with 3750 steps per degree in comparison to 7500 or 15000 steps per degree; (c) Simulation of the angle dependent Al K-L₃ XRF emitted by 1nm of Al on Si; (d) The calculation using 2500 steps per degree deviates from the one performed using smaller step sizes. All calculations were carried out using Mo K-L₃ excitation and 0.02 degrees angular divergence.

2.3.2 Beam footprint

The footprint of the beam on the sample (i.e. the illuminated area on the sample) depends on the angle of incidence (Figure 14). Therefore a geometric correction factor was implemented in the GIXRF calculation, which considers the size and intensity distribution of the beam footprint in relation to the area of the sample seen by the detector (Figure 15). The approach also allows corrections for angles between sample and detector deviating from 90 degrees, which are usual for TXRF-like setups. Furthermore two different experimental setups can be modeled: either a setup, where the incident angle is chosen by rotating the sample in relation to source and detector, or a setup, where the source is moved and the angle of detector to sample is fixed. Therefore the software can be used to evaluate measurement data obtained at synchrotron setups, which typically are of the former kind, as well as lab setups, which can be of the latter kind. This procedure is similar to the suggestion in [55], but additionally considers the non-uniform beam profile. The approach of Li et al. [56], which describes the detector/collimator assembly with more parameters has also been investigated, but was dismissed as it does not lead to an improvement of the results [57].

Also for the calculation and measurement of XRR intensities an effect of the beam size and resulting footprint can be observed [58]. In this case, if the sample is shorter than the full beam footprint at a given angle, the detected intensity will be lower than expected, as shown in Figure 16. A correction factor for this effect has been included in the calculation of XRR intensities.

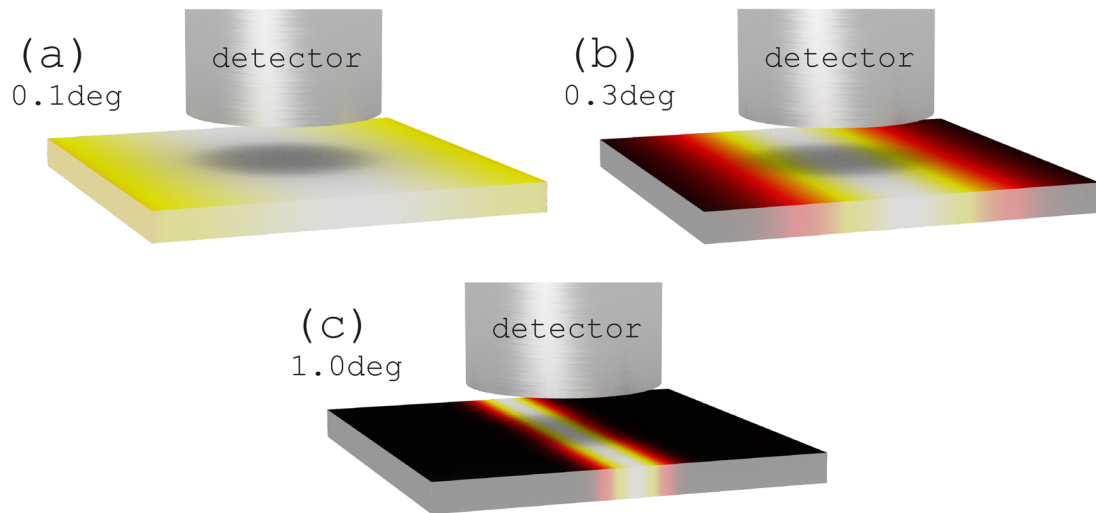


Figure 14: Beam footprint on a $2 \times 2 \text{ cm}^2$ sample for a beam of Gaussian shape with $50 \mu\text{m}$ FWHM in vertical direction in relation to the detected area. The angle of incidence is 0.1 (a), 0.3 (b) and 1.0 (c) degree.

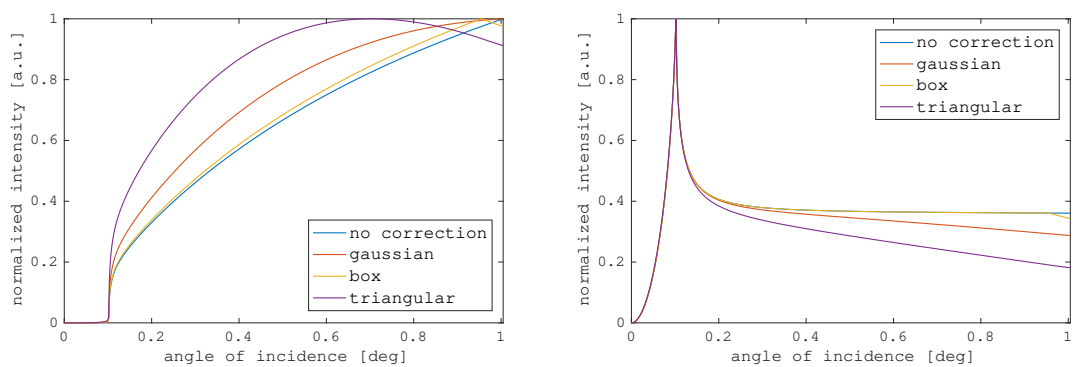


Figure 15: Influence of the beam shape and footprint on the sample on the GIXRF measurement of a Silicon bulk material (left) and a 1 nm layer on Silicon (right). Calculations were performed for Mo $K\alpha$ with $50 \mu\text{m}$ beam size and 3 mm detector slit.

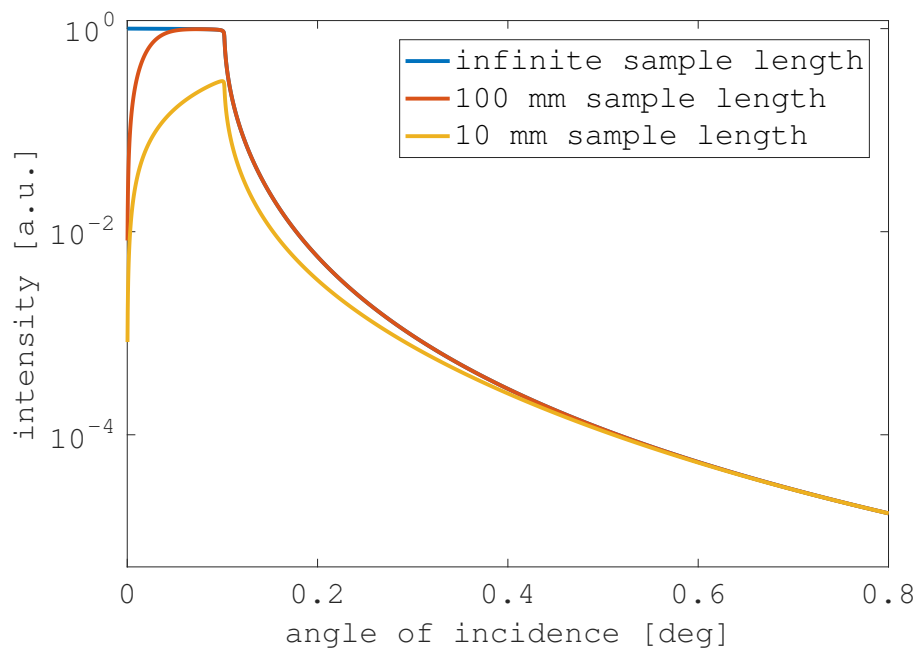


Figure 16: Influence of sample size on the XRR measurement for a $50\ \mu\text{m}$ beam of gaussian shape.

3 Instrumentation for combined measurements

GIXRF and XRR use a similar measurement procedure, i.e. increasing the incidence angle of an X-ray beam and collecting data at various angles. While the XRR detector is positioned behind the sample and records the intensity of the specular reflected beam at a specific angle, the XRF detector records the characteristic X-ray fluorescence emitted by the sample (Figure 17). As neither detector interferes with the respective beam path of the other detector and the requirements on the beam, i.e. monochromatization and low divergence, are similar, a combination of the two techniques is relatively straightforward.

There exist published examples of combined GIXRF and XRR measurement setups for the laboratory by van den Hoogenhof et al.[16], Ghose et al.[45] and a commercial instrument by Terada et al.[59]. Nevertheless when we started work on the project, there was no instrument for the laboratory, especially with state-of-the-art detectors, available.

Furthermore it has to be mentioned that concerning instrumentation, the situation at the synchrotrons was not much better. To the best of our knowledge there existed an experimental setup at the B16 Test beamline at Diamond Light Source[31] and a dedicated instrument at the PTB laboratory at BESSY II[36]. Only recently additional instruments have become available: at the BL-16 beamline of Indus-2[32], at the XRF beamline of Elettra Sincrotrone Trieste[34], at the metrology beamline of SOLEIL[35] and at the X-ray innovation laboratory BLiX (TU Berlin). It should be noted that the instruments at Elettra, SOLEIL and BLiX are based on a model developed by PTB and TU Berlin[33].

Thus in order to be able to test the software presented in section 4.4 and develop applications (chapter 5), we had to build a suitable instrument for our

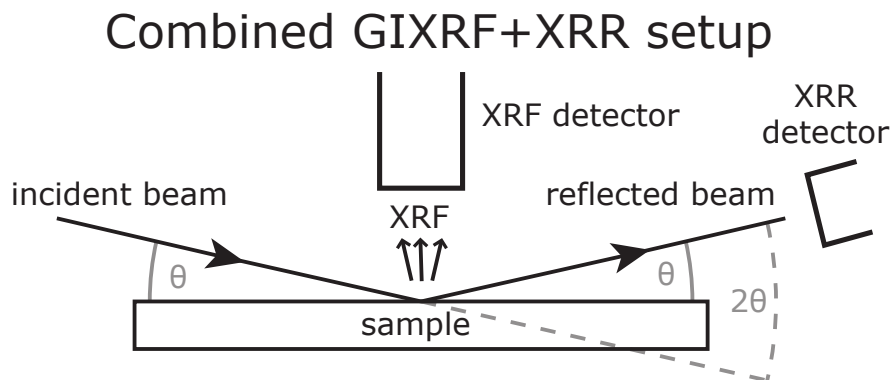


Figure 17: Schematic illustration of a combined GIXRF and XRR setup.

laboratory. We discerned two ways to achieve this goal with reuse of existing instrumentation, which should help limit expenses and development time: On the one hand we could modify an existing GIXRF setup in our laboratory at the Atominstitut (ATI) of the Vienna University of Technology by adding an XRR detector; on the other hand we could refit a commercial diffractometer at the X-ray Center of the TU Wien by adding an XRF detector. We decided to follow both approaches, which are presented in the following section (section 3.1) respectively section 3.2. Furthermore we evaluated the performance of the two spectrometers and also performed measurements for comparison purposes at the XRF beamline of Elettra (section 3.3).

3.1 GIXRF and XRR table-top vacuum spectrometer

A GIXRF spectrometer developed by Ingerle et. al.[21] was modified for the additional, simultaneous measurement of XRR within the framework of the master's thesis of M. Schiebl [60]. The details and results presented here were also published in [61].

The spectrometer allows flexibility in the choice of anode material and source size as standard XRD glass or ceramic tubes can be mounted. Typically a tube with Molybdenum or Copper anode and a virtual source size of $0.04 \times 12 \text{ mm}^2$ (long fine focus) or $0.04 \times 8 \text{ mm}^2$ (fine focus) is used. The setup uses a W/C multilayer monochromator and slits to collimate the beam to $0.05 \times 10 \text{ mm}^2$. A Vortex SDD with an active area of 50 mm^2 , which is fixed above the pivot of the sample, is used for the acquisition of XRF spectra. The detector has a collimator with a slit of $8 \times 3 \text{ mm}^2$, which is approximately 3 mm above the sample and has a length of 10 mm.

The XRR measurement is done in a classical ϑ - 2ϑ geometry: the sample rotates for an angle ϑ relative to the incident beam, and the detector collecting the reflected photons for 2ϑ . Due to the limitations imposed by the vacuum chamber, a motorized goniometer could not be used for the movement of the XRR detector. Instead of the rotational motion of the detector for 2ϑ , the angle position is approached by a translation combined with a tilt. Figure 18 shows the setup. As two different pivot points (sample and XRR detector) occur, a position correction was implemented to simulate a goniometer (see Figure 19). The necessary calculation for the translation of desired angle position to motor movements is performed in the control software, which was further developed from the software described in the master's thesis of D. Ingerle [62].

The reflected beam is measured by an Amptek Silicon Drift Detector (SDD),

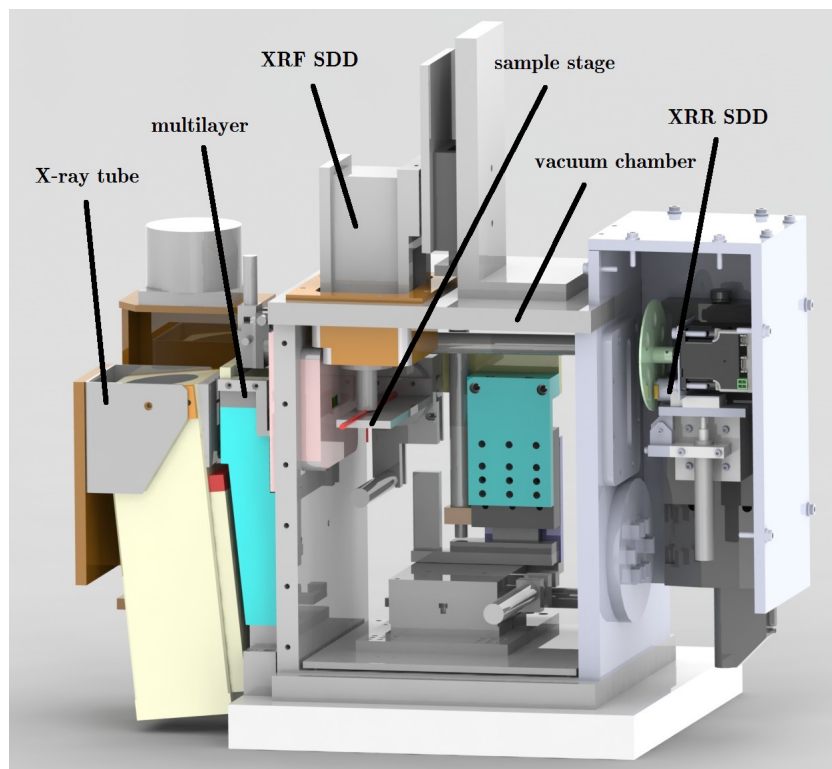


Figure 18: Scheme of the GIXRF+XRR spectrometer. A multilayer is used to monochromatize the incident X-ray beam. The Si wafer is positioned on a 5-axis sample stage, in order to perform sample movements necessary for adjustment and analysis. The sample stage is placed in a vacuum chamber with a size of $300 \times 300 \times 340 \text{ mm}^3$ and allows the measurement of wafers up to 100 mm in diameter. [61]

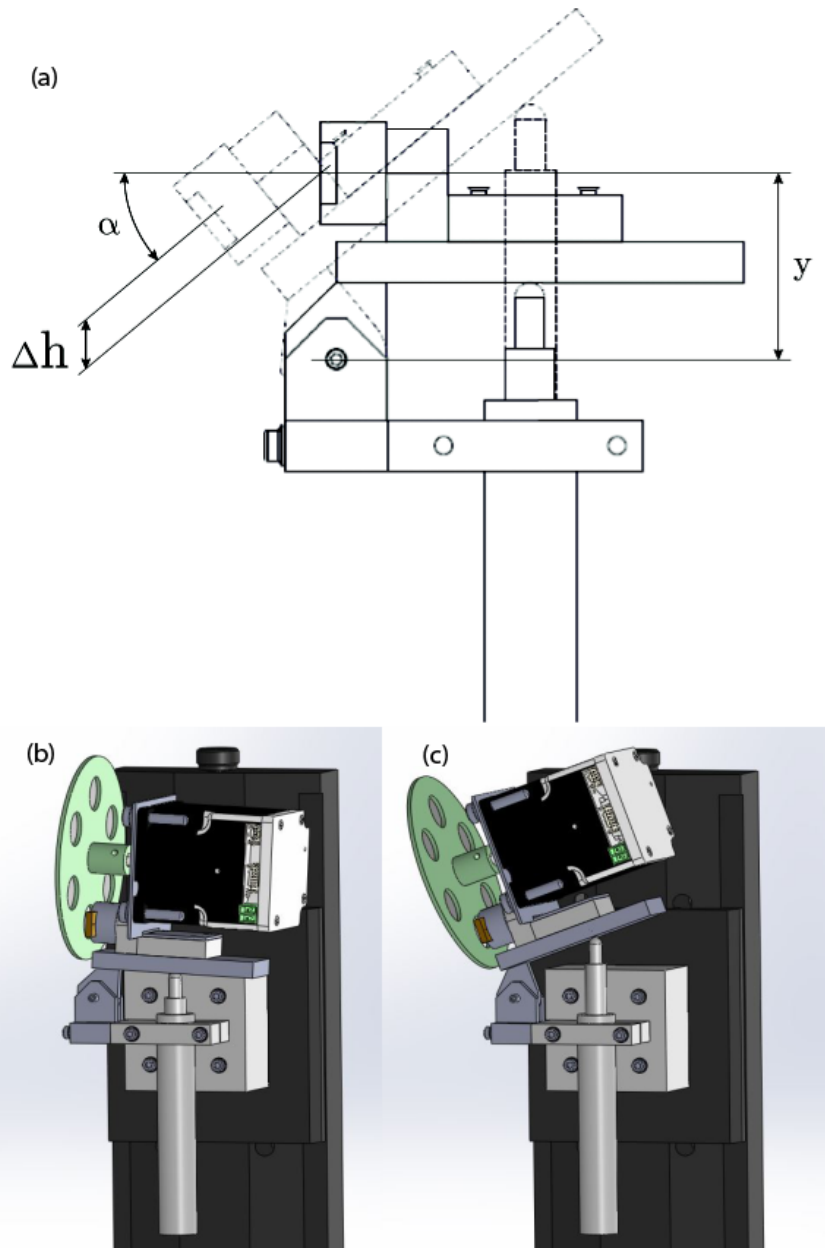


Figure 19: Scheme of the XRR-unit showing the tilt of the SDD done by a simple linear motor. (a) tilt correction, when changing the angle by a linear motion. (b) and (c) technical realization. [61]

which was chosen for its wide dynamic range and low electronic noise. In order to limit the angular divergence, a horizontal entrance slit of 100 μm is mounted in front of the detector. To reduce the high count-rate of the direct and totally reflected beam at small angles, which exceeds the working range of the SDD, different filters can be inserted in front of the detector by means of a motorized filter wheel. Typically we use a Zr filter for Mo $K\alpha$ or a Ni filter for Cu $K\alpha$ excitation. The measuring process is split into two parts: The first one (small angle of incidence) with a filter in front of the SDD, the second part (higher angle of incidence) is done without a filter. In this way the dynamic range could be enhanced from 6 orders of magnitude without using the filter to 8 orders of magnitude when using the filter.

3.2 Refitting an X-ray Diffraction System for combined GIXRF and XRR measurements

The Empyrean X-ray diffraction system by PANalytical[63] is a basic platform for a variety of applications in analytical X-ray diffraction. It offers beam optics, detectors and software for X-ray Reflectometry on thin layers, but no support for X-ray Fluorescence. The goniometer, which is the central part of the Empyrean, has a radius of 240 mm. It features Heidenhain encoders and a minimum step size of 0.0001 degree for the angle of incidence as well as the scattering angle. The PreFIX concept allows the exchange of beam optical and detector modules within minutes. An Amptek SDD was added to this system and the acquisition of XRF spectra synchronized to the XRR scan. A custom acquisition software, which is partly based on the software for the table-top spectrometer presented in section 3.1, was developed to achieve this goal.

The line focus of an Empyrean Cu LFF HR X-ray tube was used for the measurements. This metalceramic tube has a maximum power rating of 1.8 kW and a focal spot of 12 mm x 0.4 mm. The exit window consists of beryllium with a thickness of 300 μm . The tube was operated at 45 kV and 40 mA.

A wide variety of incident beam optics, i.e. monochromators and mirrors, is available for the Empyrean. We used and compared (section 3.3) four of them. All modules were used with a $1/32^\circ$ (0.05 mm) divergence slit and a 10 mm beam mask.

- The Hybrid monochromator consists of a parabolical shaped graded multilayer and a channel-cut Ge(220) crystal in one module. It creates an quasi-parallel beam of almost pure $K\alpha_1$ radiation.
- The Bragg-Brentano^{HD} module converts a divergent X-ray beam into a

monochromatic divergent X-ray beam. We used this module with a $1/32^\circ$ (0.05 mm) exit slit.

- The parallel beam X-ray mirror module contains a parabolical shaped graded multilayer. It converts the divergent beam into a monochromatic $K\alpha$ quasi-parallel beam.
- The focusing X-ray mirror module contains an elliptical shaped graded multilayer. It converts the divergent beam into a monochromatic $K\alpha$ beam, focused on the goniometer circle.

An Amptek XR-100SDD with Be entrance window was used for detection of the created X-ray Fluorescence radiation. It has a 25 mm^2 active area and is $500 \mu\text{m}$ thick. The signal processing was done by an Amptek PX4. The detector was placed 3 mm above the sample.

The XRR detector assembly consists of a 0.18° parallel plate collimator, a programmable beam attenuator and the detector module. The beam attenuator contains a Nickel foil, which is $125 \mu\text{m}$ thick. The foil, which reduces the Cu $K\alpha$ intensity by a factor of 174, is automatically inserted into or retracted from the beam path, if the count rate exceeds or falls below a configured threshold. Concerning the detector module, we tested a scintillation and a PIXcel3D (Medipix2) detector. After measurements with the parallel beam mirror we realized, that the count rate at small angles exceeds the specified 99% linearity range of the scintillation detector (0 - 500 kcps). Thus we only used the PIXcel^{3D}, which has a 99% linearity range of 0 - 5×10^6 cps per column, for further measurements. The detector was used in open detector (0D) mode.

We used the Data Collector program, which is the standard software for the Emyrean, for movement control and for the acquisition of XRR data. In order to start, stop and read out the XRF detector in synchrony with the XRR scan, we developed our own software. This program is partly based on the control software, which was developed for our GIXRF and XRR vacuum spectrometer (section 3.1). The XRF scan acquisition is only started for symmetric goniometer scans in step mode.

Figure 20 shows a view of the interior of the diffractometer with the added XRF detector.

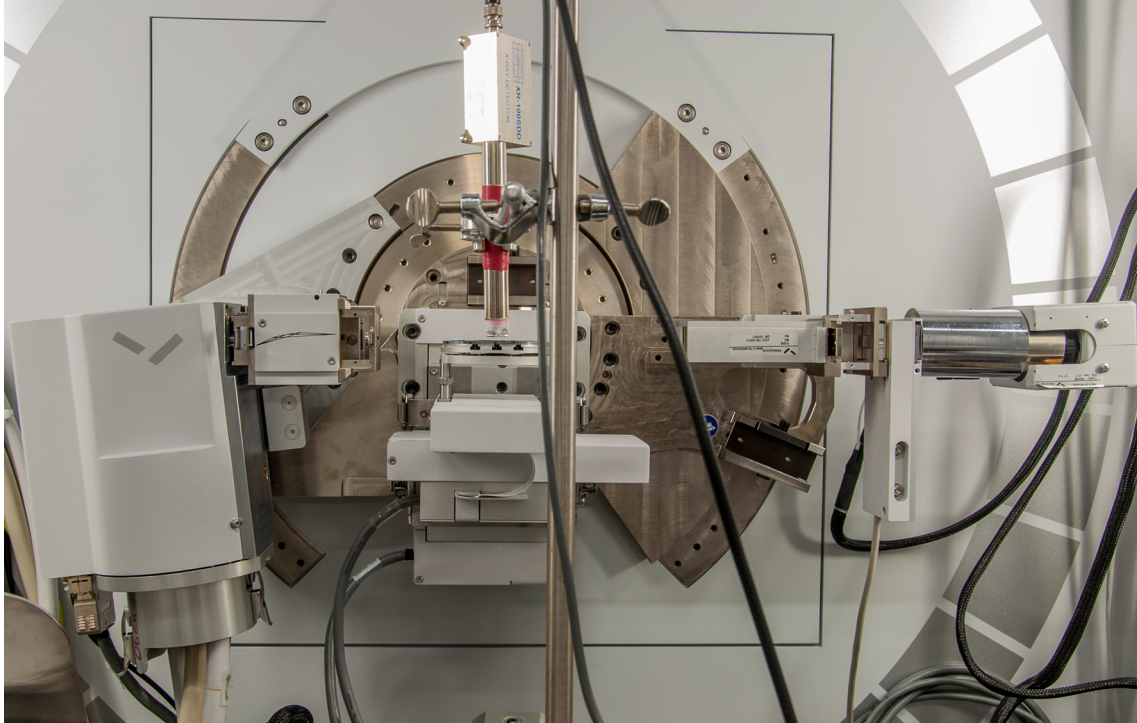


Figure 20: View of the interior of the Empyrean with the XRF detector in place.

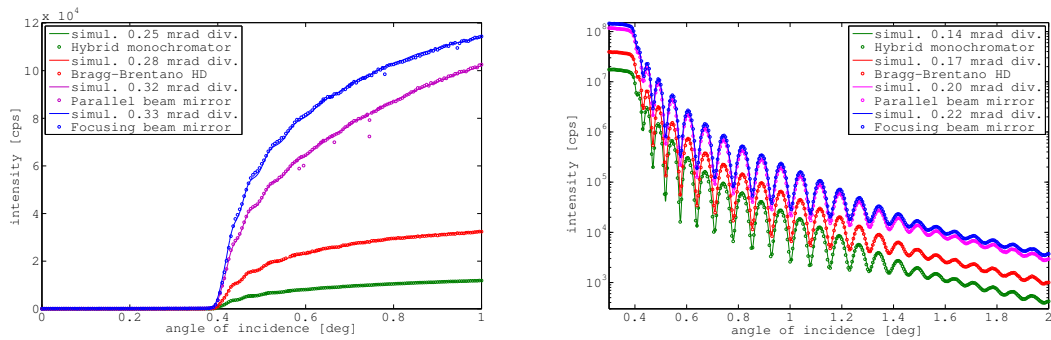


Figure 21: Comparison of GIXRF Si K α (left) and XRR (right) measurements of a 50 nm layer of Ni on a 300 nm thick, thermally grown SiO₂ layer on Si substrate performed with different monochromators at the Empyrean.

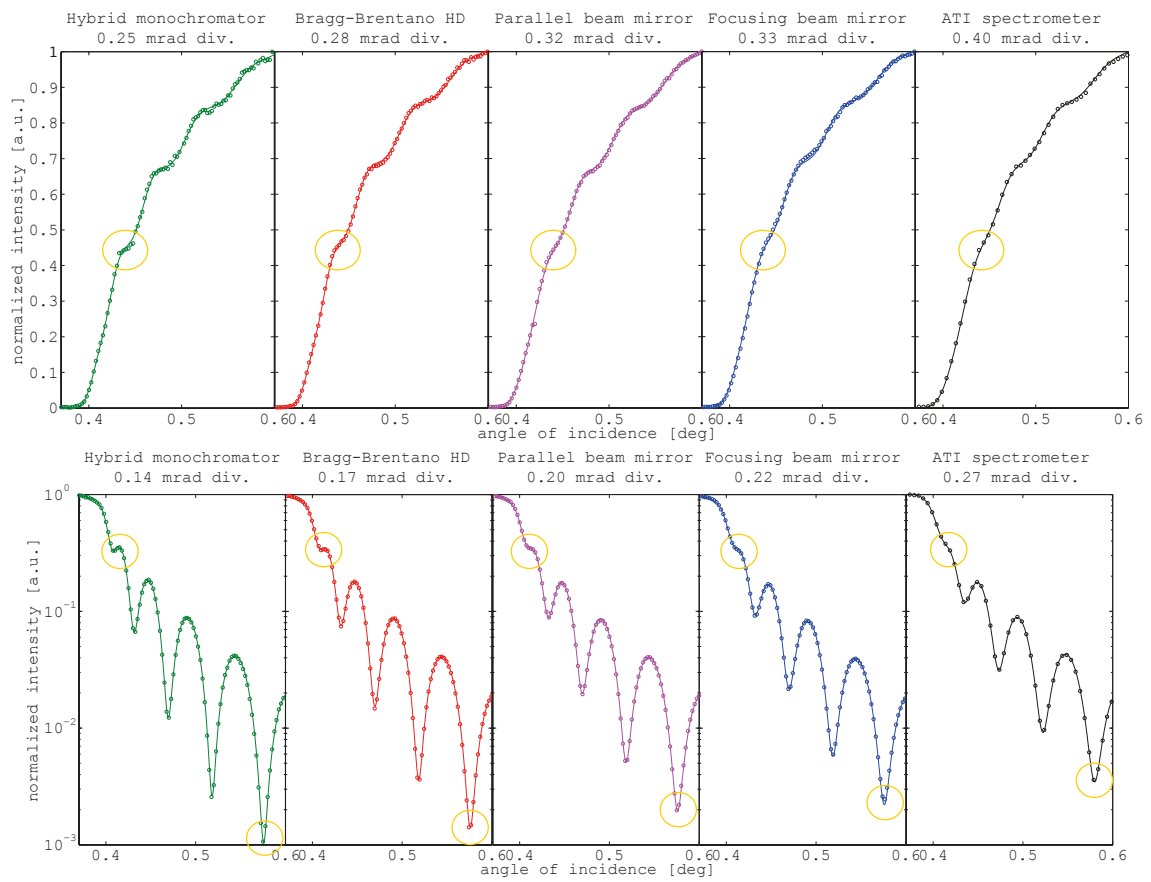


Figure 22: Magnification of the angular range near the critical angle of GIXRF Si $K\alpha$ (top) and XRR (bottom) measurements of a 50 nm layer of Ni on a 300 nm thick, thermally grown SiO_2 layer on Si substrate.

3.3 Comparison of measurements

3.3.1 Comparison of the table-top spectrometer with the Empyrean X-ray Diffraction System

A sample consisting of a ~50 nm Nickel layer on Silicon substrate was used to compare the performance (i.e. divergence and intensity) of the two developed spectrometers, which were described in the previous sections (3.1, 3.2). In the comparisons shown in Figure 21 and Figure 22 we also used the different incident beam optics, which were available for the Empyrean system. We performed combined measurements of Si-K α XRF and XRR with an acquisition time of 7 seconds per point. The evaluation was done with the software JGIXA (see section 4.4). The program reports two values for divergence, one for the XRF curve(s) and one for the XRR curve, as receiving slits or a parallel plate collimator in front of the XRR detector will usually improve the second value.

The data in Figure 21 and Figure 22 clearly show that there is a trade-off between divergence and intensity. The close match of parallel and focusing beam mirror can probably be explained by the large focal length of the focusing mirror (~40 cm). The Hybrid monochromator offers very good divergence with still reasonable intensities, while the parallel and focusing beam mirrors are the antipodes with very high intensity and good divergence. In the current configuration the Bragg-Brentano^{HD} module seems to represent a good compromise for most applications.

From the measured data it is obvious that the Empyrean showed smaller divergence than our table-top spectrometer. Also the measured intensities were higher, especially with the parallel and focusing mirror. But this better performance comes at the cost of reduced flexibility, as the beam optics for the Empyrean are configured for a specific energy and most of them are only available for Cu K α radiation.

3.3.2 Comparison of the table-top spectrometer with the XRF beamline of Elettra Sincrotrone Trieste

To compare the performance of the table-top spectrometer described in section 3.1 with a synchrotron source, we performed measurements at the multipurpose X-ray spectrometry end-station provided by the International Atomic Energy Agency (IAEA) [34] and located at the X-ray fluorescence (10.1L) beamline of Elettra Sincrotrone Trieste [64]. This instrument, like the lab instrument, is equipped for combined GIXRF and XRR measurements, i.e. the simultaneous

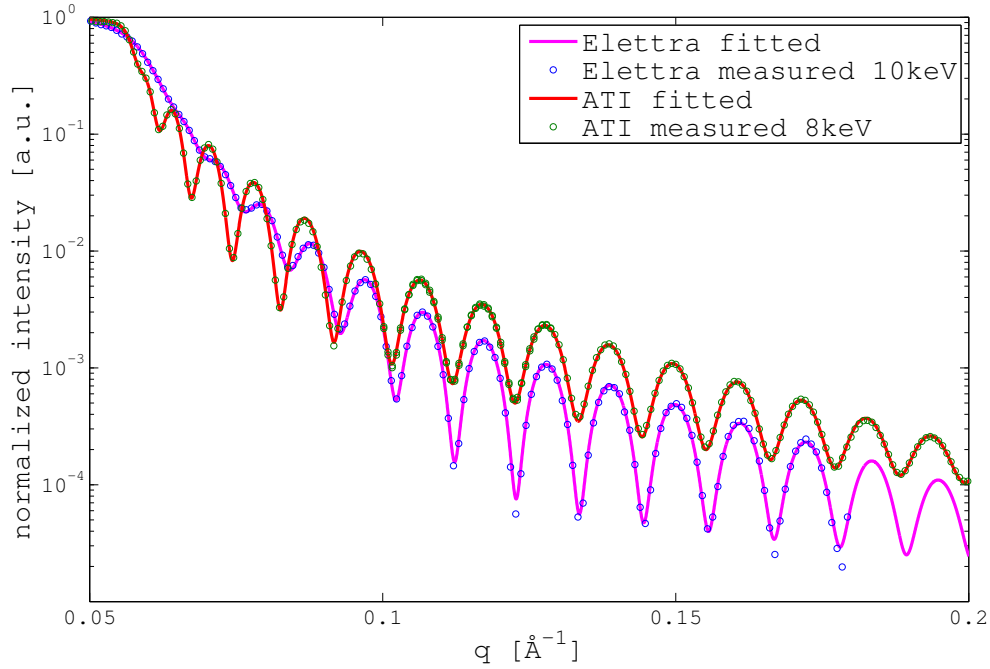


Figure 23: Comparison of measurements of a nominal 50 nm Nickel layer on Silicon substrate.

acquisition of both detector signals.

The beamline uses radiation from a bending magnet, which is preconditioned by a double crystal (Si(111)) monochromator. At the exit slit the beam has a size of $250 \times 100 \mu\text{m}^2$ (hor x ver) and an angular divergence of 0.15 mrad. The XRF detector is a SDD (XFlash 5030), which has a nominal crystal area of 30 mm^2 . The measurements were done using an optimized detector collimator with a length of 11 mm, which was positioned 5 mm from the sample. The XRR signal was measured via the current from a Hamamatsu Si-photodiode.

The source of the lab spectrometer was a fine focus Copper tube with characteristic Cu $K\alpha$ radiation of 8.04 keV, which was operated with 50 kV and 25 mA.

Figure 23 shows X-ray reflectometry data from a nominal 50 nm thick Nickel layer on a 300 nm thick, thermally grown SiO_2 layer on Silicon substrate. The measurement at Elettra Sincrotrone Trieste was performed using an incident beam of 10 keV and an acquisition time of 2 seconds per point, while the measurement in the lab used Cu- $K\alpha$ (8.04 keV) radiation and 30 seconds per point. The calculation shows a Nickel layer with a thickness of 52.5 nm and a density of 8.9 g/cm^3 , which agrees very well with the nominal thickness of 50 nm.

The second sample consisted of a layer of Titanium with a nominal thickness of 20 nm, which was deposited on a 300 nm thick, thermally grown SiO_2 layer

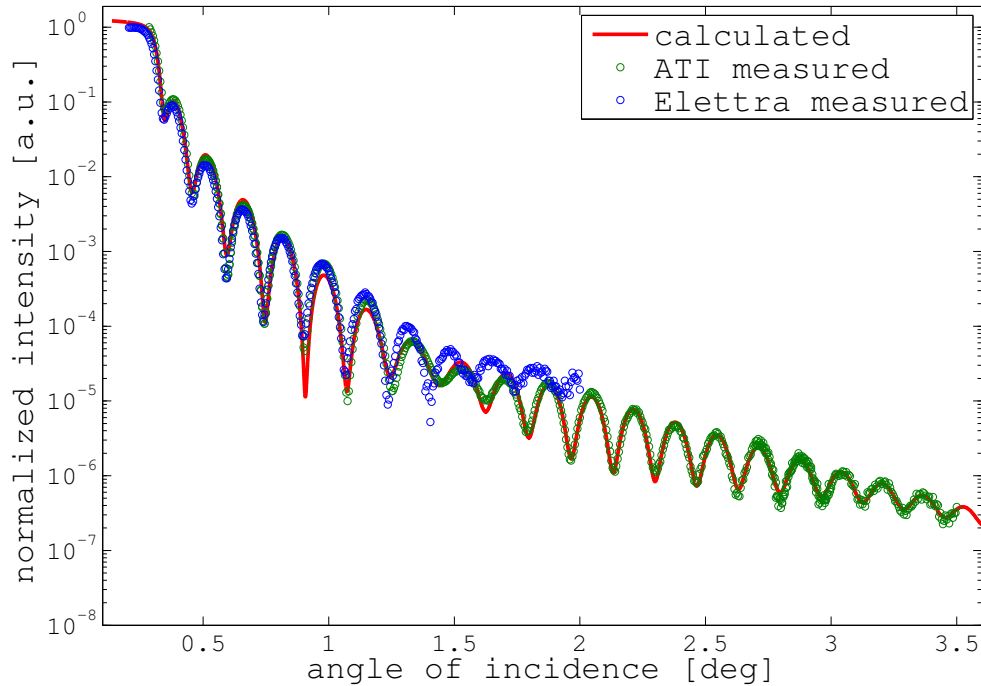


Figure 24: Comparison of measurements of a nominal 20 nm thick Titanium layer on a 300 nm thick, thermally grown SiO₂ layer on Silicon substrate.

on Silicon. Measurements were performed at 8.04 keV with an acquisition time of 2 seconds per point at the synchrotron and 30 seconds per point in the lab. The fitted result shows a model with 26 nm of TiO₂ and no pure Ti layer, i.e. the Titanium layer seems to be fully oxidized. The measurements of both spectrometers (Figure 24) show good agreement up to 1.4 degree, where the measured data start to deviate from each other.

A silicon wafer coated with nominal 100 nm of gold, using a Titanium adhesion layer between Gold and Silicon, was measured at an energy of 8.04 keV at the synchrotron and in the lab. Acquisition time per point was 5 and 10 seconds, respectively. The GIXRF data for Au-M α and Ti-K α of both instruments show good agreement with a calculated result for 101 nm of Gold and a density of 18.5 g/cm³, the differences in curve shape are only due to geometrical corrections (see section 2.3). The XRR data from the lab agree very well with the same model, while the synchrotron data deviate strongly and show no Kiessig fringes (Figure 25).

In conclusion we can assert that the GIXRF measurements and results of both setups were generally in good agreement, but that the XRR data obtained at the beamline were limited in dynamic range due to the photodiode.

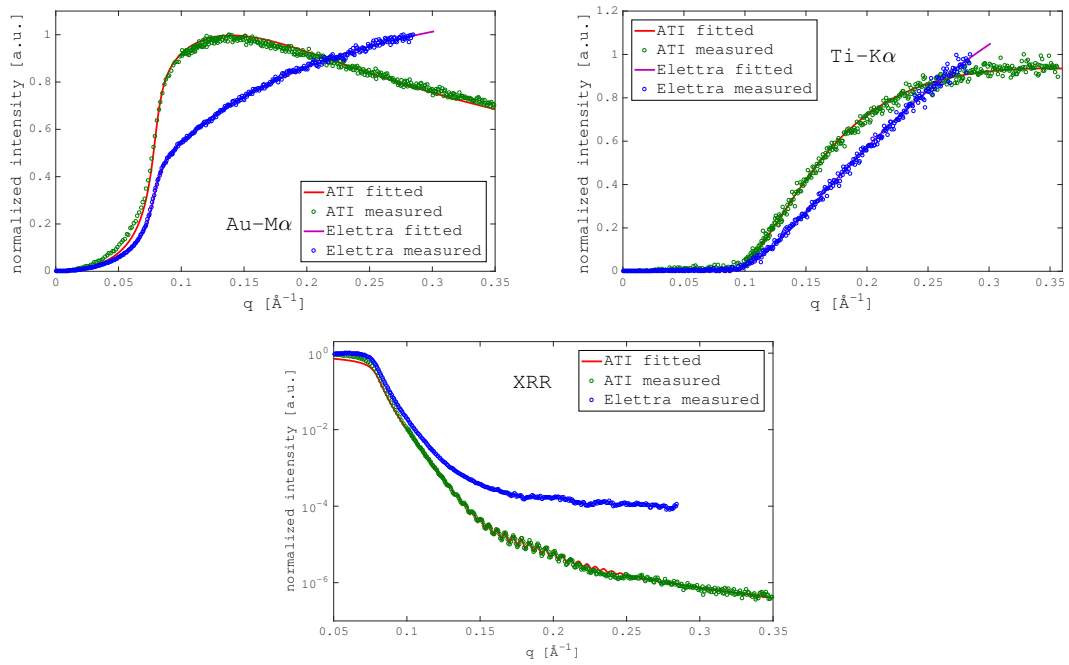


Figure 25: Comparison of measurements of a Silicon wafer coated with nominal 100 nm of Gold, using a Titanium adhesion layer between Gold and Silicon.

4 Evaluation

The evaluation of GIXRF and XRR data does not consist in a reverse transformation, but in calculation and fitting of simulated measurements for possible candidate sample models. The parameters like thickness, density and roughness of the layers of the sample are then refined by an optimization algorithm until a sufficiently good fit to the measurement data is found. Additional parameters, which have to be known or be determined for a good simulation, are parameters for the correction of the instrumental effects (see section 2.3) and the instrumental sensitivity. The developed software JGIXA (JavaGIXA) packages all the required inputs for the calculation and several optimization strategies in a GUI.

4.1

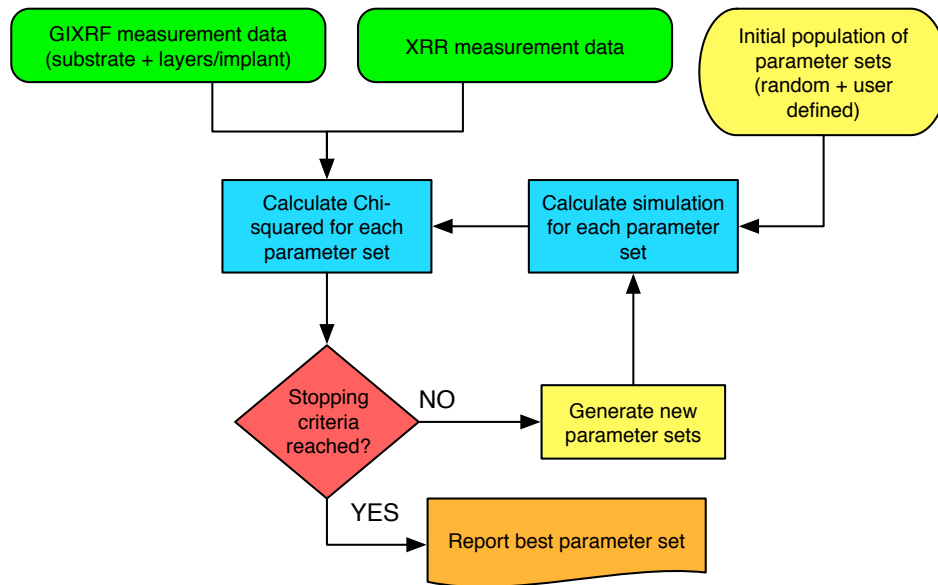


Figure 26: Flowchart of the optimization algorithm.

Figure 26 describes the workflow of the optimization algorithm. The goodness of the fit for all available measurement data (GIXRF and XRR) is combined in one chi-squared value, i.e. for n measurements with i data points:

$$\chi_{sum}^2 = \sum_n \frac{1}{\nu_n x_{n,max}} \sum_i \chi_{n,i}^2 \quad (49)$$

where ν is the number of degrees of freedom and x_{max} is the maximum cal-

culated value of each curve. This normalization of the chi-squares allows the combined evaluation of the measurement data, which have a varying number of measurement points and different orders of magnitude. The value $\chi_{n,i}^2$ is the measure for the i individual data points of the n -th measurement, which depends on the measurement type and the selection made by the user.

For GIXRF data the χ^2 measure is the common and well-known expression:

$$\chi_{n,i}^2 = \frac{(x_{n,i,meas} - x_{n,i,calc})^2}{x_{n,i,calc}} \quad (50)$$

For XRR data two choices are available:

- a log-based chi-squared, which is commonly used for XRR data evaluation:

$$\chi_{n,i}^2 = [\log(x_{n,i,meas}) - \log(x_{n,i,calc})]^2 \quad (51)$$

- multiplication of the data for measurement point i by the respective incident angle θ_i to the power of 4, which eliminates the reduction in intensity due to the increasing angle [65, 66], thus enhancing the sensitivity for small intensity differences at larger angles:

$$\chi_{n,i}^2 = \theta_{n,i}^4 \frac{(x_{n,i,meas} - x_{n,i,calc})^2}{x_{n,i,calc}} \quad (52)$$

As it was shown before in section 1.3, fitting results obtained using only GIXRF data can be ambiguous because density and layer thickness are correlated, while in the case of using only XRR data the hyper-surface in parameter space for XRR fitting can contain local minima [68, 69]. Additional investigations on the fitness landscape of a combined optimization, which were done within the project thesis of J. Kirschner [67], indicate that even in the case of combined analysis, the surface can contain local minima (Figure 27). Thus a local optimization algorithm like Levenberg-Marquardt or Simplex would produce different results depending on the starting point in parameter space. To avoid these problems we firstly combine measurement data from both techniques and secondly based the fitting procedure on global optimization algorithms, which do not rely on the calculation of derivatives.

4.2 Overview of available optimization algorithms

The optimization algorithms in JGIXA were chosen from the branch of global optimization algorithms, which focus on finding the global minimum in the parameter space and try to prevent being stuck in a local minimum. The algorithms

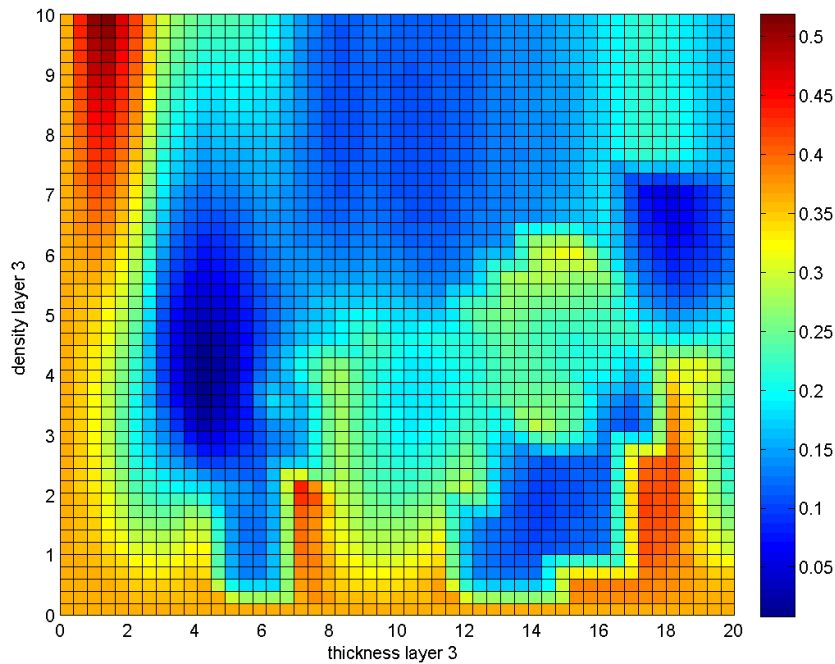


Figure 27: Fitness landscape for variations of thickness [nm] and density [g/cm³] of the TiO₂ layer in a TiO₂/Ti sample on Si substrate with several local minima. (from [67])

do not rely on derivatives and are heuristic strategies, which are not deterministic, i.e. they do not theoretical guarantee that the reported solution is the global one. Nevertheless our results with some algorithms were quite promising, but in some cases repeated execution of the optimization can lead to improved results.

The following algorithms are available in JGIXA:

- Simulated annealing (SA) [70] was inspired by the controlled heating and cooling of materials to reduce the dislocation of atoms in the crystal lattice. The algorithm evaluates candidate solutions and decides whether to move to a new state or not by evaluating an acceptance probability function. This function depends on the values of the current and the new state and a global parameter called the temperature, which changes and generally decreases over time. The higher the current temperature the higher the probability that the algorithm will move “uphill” to a higher value, thus possibly moving out of a local minimum.
- Genetic algorithm (GA) [71] considers the optimization like natural selection in an evolutionary process. At each iteration step the population of candidate solutions is evaluated for its fitness (i.e. smaller chi-squared) and a new generation of child solutions is created by mutation and crossover of

parameter values. Mainly the best solutions are selected for this reproduction step, thus the average fitness of the population will increase with each generation.

- Pattern search [72] is a direct search algorithm, which uses a set of vectors, called a pattern, to determine which points will be searched at each iteration. The strategy for this exploration of the search-space is adapted, depending on the success or failure of finding a smaller value.
- Differential evolution (DE) [73] is an evolutionary algorithm which is quite similar to GA in some respects. It also uses a population of candidate solutions, but uses different strategies to create its new population members. Furthermore it is greedy in the selection of new members, i.e. it only accepts a member, if it is better than the one it replaces.
- Particle swarm optimization (PSO) [74] is a relatively simple algorithm, which uses a population of candidate solutions with position and velocity. The movement of this swarm of particles in search-space is modeled like a simplified social model of bird flocks or fish schools. The particles exchange information on best known positions and therefore the movement of each particle is not only guided by its own current and best known position, but also by the best known position of other particles or the swarm.

Pattern search, simulated annealing and genetic algorithm use the implementation from the MATLAB Global optimization toolbox. A comparison of the performance and results of the individual algorithms for a layered sample and an implanted sample will be presented in section 4.3.

4.3 Comparison of optimization algorithms

The performances of the available optimization algorithms (simulated annealing (SA), genetic algorithm (GA), pattern search, differential evolution (DE) and particle swarm optimization (PSO)) were tested by repeated (10 times) fitting with each algorithm and comparing the convergence. For the differential evolution algorithm two common variants were tested: DE/rand/1/bin and DE/best/1/bin [75]. For the algorithms DE, GA and PSO a population size of 100 was used. The number of maximum iterations was set to 5000 for simulated annealing and 500 for all others.

4.3.1 Layers

The parameters for layers that can be fitted are thickness, density, roughness, and elemental concentration. The first sample shown is a nominally 50nm thick

layer of pure Ni on a Si substrate, which was measured by using Mo-K α radiation. The sample model used for fitting consisted of an oxidized low density surface layer of 1.5-2 nm on top of a pure Ni layer. The starting values for thickness and density (80 nm, 8 g/cm³) of the pure Ni layer were chosen far from the nominal values (50 nm, 8.9 g/cm³), in order to test the performance under more difficult conditions. During the fit a large parameter range for thickness (30-100 nm) and density (8-9.5 g/cm³) was allowed. Figure 28 summarizes the results obtained for thickness, density and roughness of the pure Ni layer during 10 runs of each optimization algorithm and also shows a comparison of measured data to simulations using the best and worst result. The results for simulated annealing were not included in the plots, as even the best result was not close to the minimum found by the other algorithms. The overall best results were obtained by DE/best/1/bin and DE/rand/1/bin, which are very close to the same minimum, but DE/best/1/bin also shows an outlier, probably due to premature convergence to a local minimum. But also the other algorithms with the exception of SA and PS showed results within a few percent of the best obtained value. The overall most reliable algorithm was found to be DE/rand/1/bin.

4.3.2 Ion implanted samples

The calculation procedure for ion implanted samples is also based on a layered model. This is achieved by discretization of the implant depth distribution into layers of 1 nm thickness. A detailed description and justification of this procedure will be presented in 5.3. The software allows to choose from a wide range of distribution functions, e.g. symmetric and asymmetric Gaussian, or Pearson [77, 78, 79]. The refractive index for each discretization layer is calculated from the scattering factors based on the ratio of substrate atoms to implant atoms in each individual layer (which is the fitting parameter determining the profile shape). Thus the refractive index depends on the concentration profile of the implant in the substrate. For the current comparison we used a Pearson distribution with 4 parameters to describe shape and depth of the profile and the total dose of the implantation. The starting parameters were chosen far from the expected minimum in order to test the performance under more difficult conditions. Figure 29 shows a comparison of the results obtained by the different optimization algorithms for measurements of a Silicon substrate implanted with 1E15 atoms per cm² of Arsenic at 0.5 keV implantation energy in comparison to SIMS results from [76].

Simulated annealing was again omitted from the plot, as the chi-squared of

all results was approximately 2 orders of magnitudes worse than the overall best (DE/best/1/bin). The best and worst profile shapes of all other algorithms are very similar except for the worst of PSO, which shows a significant larger chi-squared value caused by a deviation in the XRR signal.

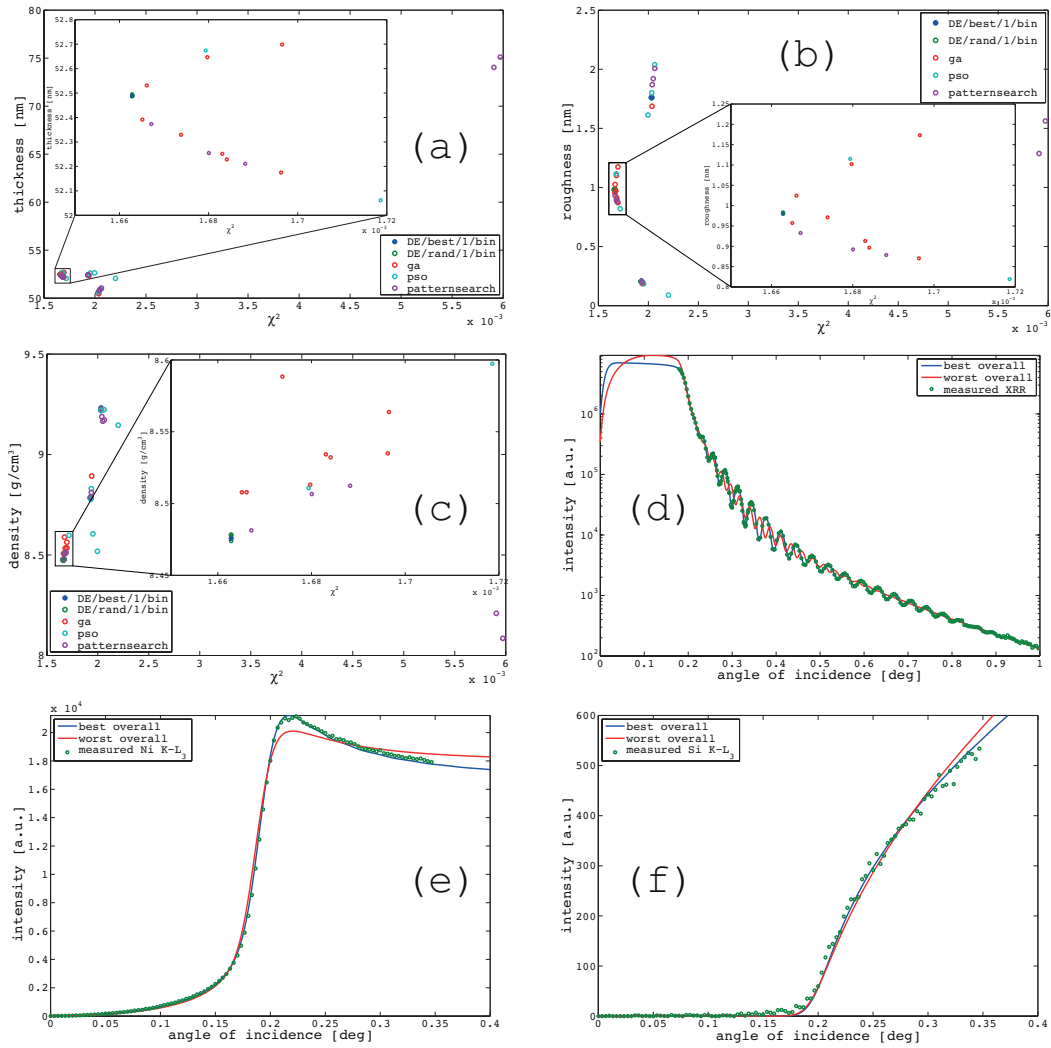


Figure 28: (a), (b) and (c) show the best result for thickness, roughness and density versus chi-squared of each run (totally 10) for the different algorithms. (d), (e) and (f) show XRR and GIXRF of Ni K-L₃ and Si K-L₃ measurement data and the simulations for the best and worst fitting results.

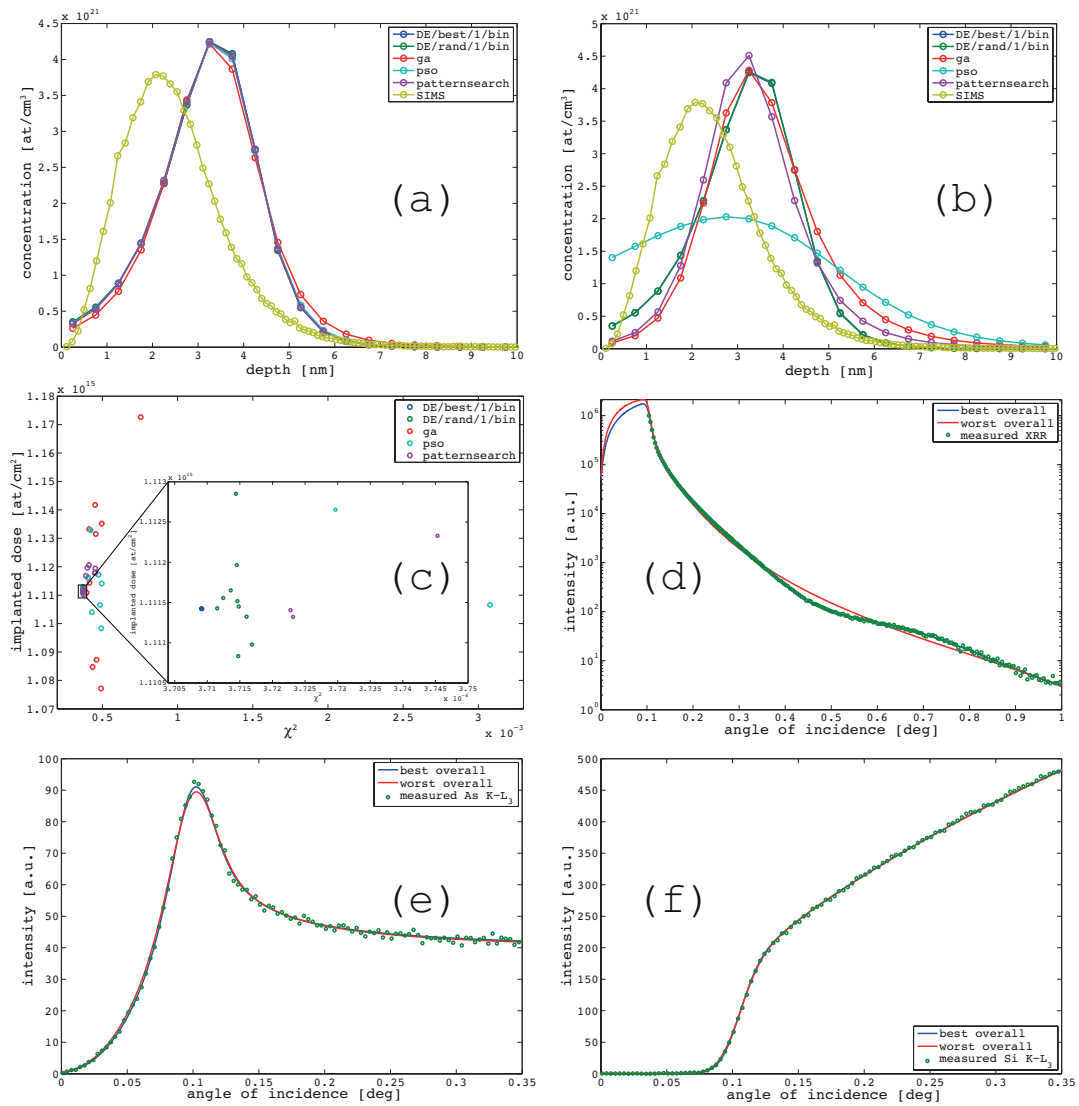


Figure 29: (a) and (b) show the best and worst result of each algorithm for the implantation profile in comparison to a SIMS profile of the same sample from [76]. (c) shows the total implanted dose versus chi-squared of each run (totally 10) for the different algorithms. (d), (e) and (f) show XRR and GIXRF of As K-L₃ and Si K-L₃ measurement data and the simulations for the best and worst fitting results.

4.4 Software - JGIXA

The developed software JGIXA is based on Java and MATLAB. Due to the choice of these programming languages the software is easily portable and in fact available for Windows, Mac and Linux. The runtime libraries of Java and MATLAB, which are required for the compiled software, are freely available for download. The relevant physical constants and coefficients e.g. scattering factors are taken from an internal database, which uses published results by Henke et al. and Ebel et al. [39, 80].

Because calculation speed is also a critical issue, especially for global optimization algorithms using several parameter sets per iteration step, the software takes advantage of local parallelization by using one Java thread per CPU core and also allows distributed parallel computation using the MATLAB Distributed Computing Server. Nevertheless and although the simulation of a single GIXA measurement typically only takes some hundred milliseconds, depending on sample complexity and computer performance, an evaluation run using genetic algorithm or differential evolution with some hundred population members can still take a few hours.

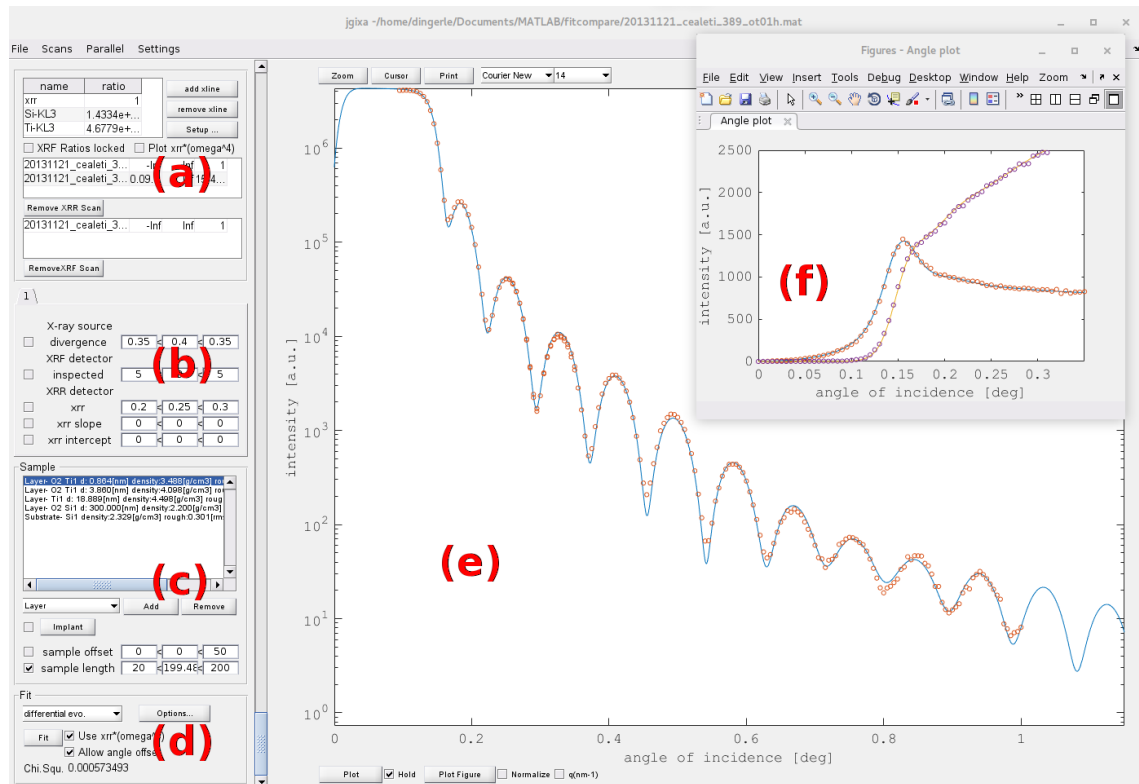


Figure 30: Screenshot of the JGIXA GUI with the areas of the main window: XRF lines and measurement data (a), setup parameters (b), sample model (c), fit and optimization algorithm (d) and data plot (e); data can also be plotted in a separate window (f).

A Graphical User Interface (GUI) has been developed to allow a user-friendly operation (Figure 30). The main window is separated into areas for the different tasks of the evaluation procedure, which will be described in detail in the following sections:

- an area for specifying the measured X-ray lines and for the management of the measurement data (section 4.4.1).
- a list of optimizable setup parameters (section 4.4.2).
- a description of the sample model (section 4.4.3).
- an area for the management of the optimization algorithm and fit related controls (section 4.4.4).
- a large plot area with controls to manage the appearance of the figures (section 4.4.5).

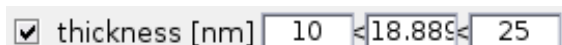


Figure 31: A parameter, which is enabled for the optimization, with lower limit, actual value and upper limit.

Most of the parameters in the software can be enabled for variation in the optimization run. Enabling a parameter for fitting is as simple as clicking the checkbox and specifying lower and upper boundaries in the left- and rightmost column (Figure 31). The center column shows or sets the actual value, which is used for the calculation and plot, and contains the value from the best parameter vector after an optimization run.

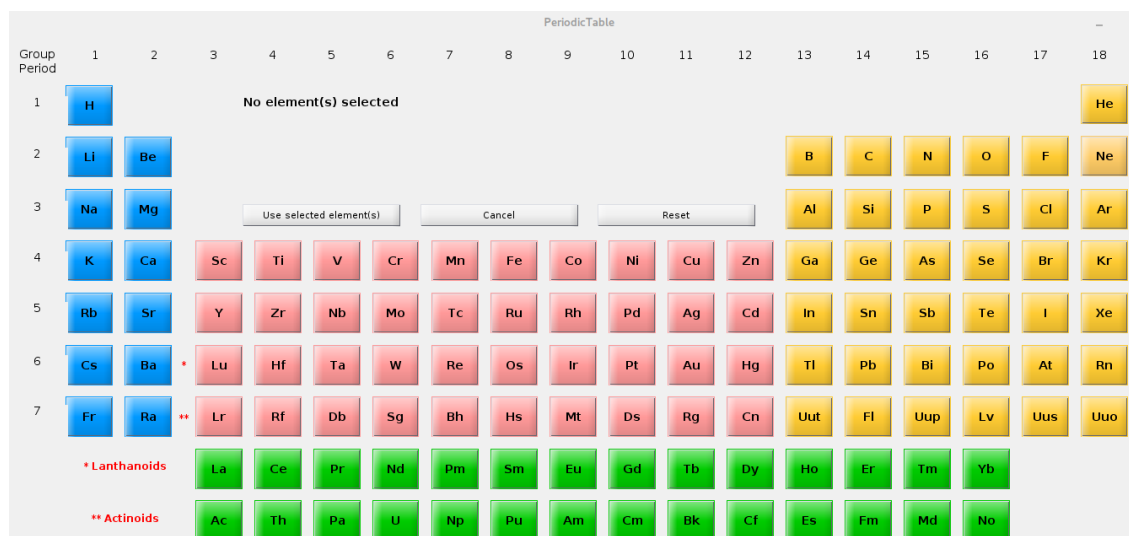


Figure 32: Dialog window with a periodic table for selecting elements.

All tasks, which involve the selection of chemical elements e.g. selection of

XRF lines or layer composition, are done via an integrated periodic table as shown in Figure 32.

4.4.1 XRF lines and measurement data

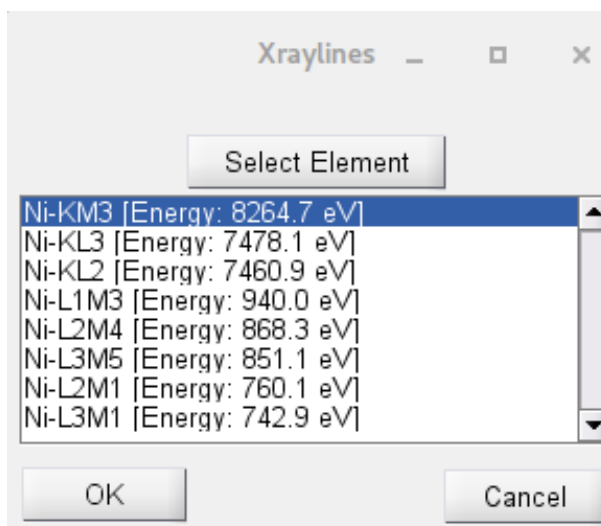


Figure 33: Dialog window for selecting XRF lines.

The first step in an evaluation project is the specification of the expected XRF lines by using the 'add xlines' button. This will open the periodic table (Figure 32) and subsequently the dialog with the XRF lines (Figure 33) of the selected element.

If the relative sensitivities of the setup for the selected XRF lines are known from a previous characterization of the instrument with a reference sample (section 5.1), they can be entered in the ratio column and the checkbox 'XRF ratios locked' can be enabled. This will keep the ratios of the scaling factors of the calculation to the measurement fixed, thus enabling quantification via internal standard or substrate.

The measurement data can be imported in two ways via import commands in the Scans menu. If the software supports the file format, no line overlap in the recorded XRF spectra has to be considered and a simple trapezoidal background subtraction in a Region of Interest (ROI) of the spectra is sufficient, the software can directly read in all recorded spectra of a GIXRF scan. Currently files from the Elettra XRF beamline, the ESRF, PANalytical diffractometers (XRR) and our own ATI scan software [62] are supported. Figure 34 shows the dialog for the GIXRF scan import. The first step after selecting the file format is clicking the 'Load Headers' button to select and read in the scan file. If required by the format, the parameters like position or livetime have to be mapped to the correspond-

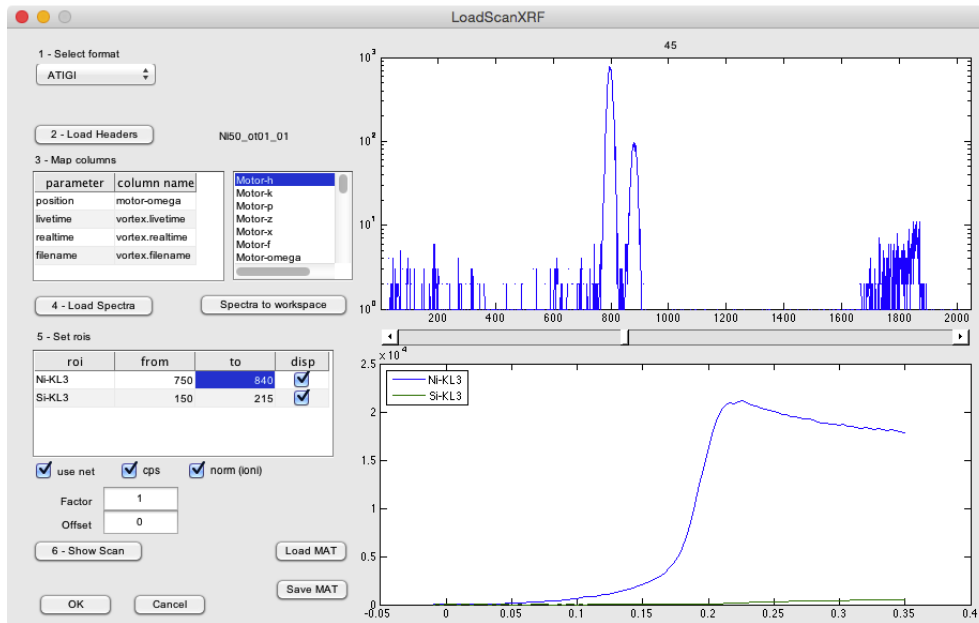


Figure 34: Dialog window for importing GIXRF scans.

ing columns. Then the single spectra can be imported and will be displayed in the upper right plot area. Moving the slider below the spectrum plot will scroll through the spectra. The minimum and maximum channel for each XRF line have to be entered in the corresponding 'from' and 'to' column. If 'use net' is enabled, a trapezoidal background subtraction will be used, otherwise all counts in the respective channel range will be used as peak area. The 'cps' checkbox normalizes the counts to counts per second and the 'norm(ioni)' normalizes to ring current or an ionization chamber, if supported by the file format and present in the measurement. 'Show Scan' displays a preview of the imported scan and 'Factor' and 'Offset' can be used to shift or convert the angle positions, if they are not in degree from zero angle.

If a more sophisticated peak deconvolution is required (as, for example performed by QXAS/Axil [81] or PyMCA [82]) or the file format ist not supported, text files with dead time-corrected net intensities per angle can also be imported.

After the import is finished, the first column in the scan list will contain the name of the imported file. The second and third column can be adjusted to limit the minimum and maximum angle, which will be used from the corresponding scan. The fourth column is a scaling factor, which can be useful, if parts of a measurement run were performed with a filter; e.g. to reduce the high intensities at small angles of an XRR scan.

4.4.2 Setup parameters

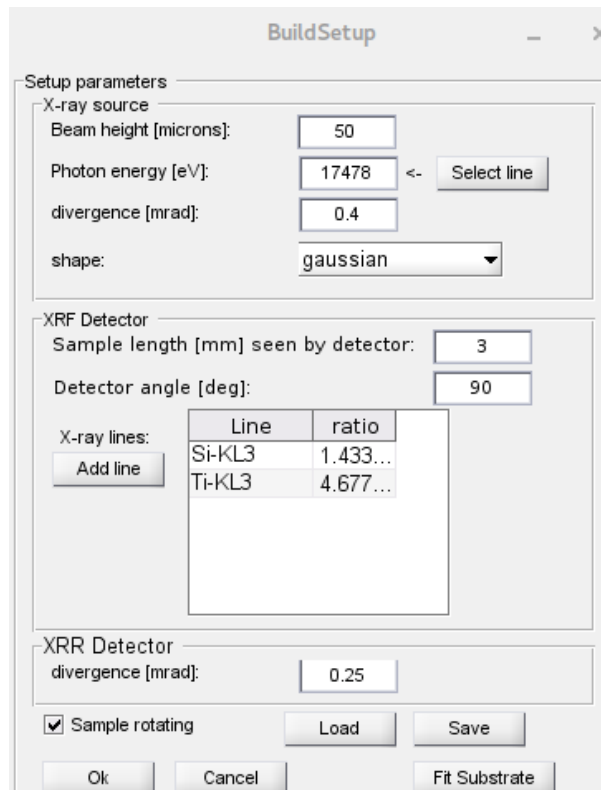


Figure 35: Dialog window for additional setup parameters.

By pressing the 'Setup..' button the dialog window for setup parameters (Figure 35) can be opened. This window contains parameters, which are also available on the main window, like the divergence parameters, the detector slit width and the XRF lines, but additionally some parameters, which are not fittable and thus only available here. This includes the beam height and shape, as well as the angle of the XRF detector to the sample surface at an incidence angle of zero degree. Furthermore the checkbox 'Sample rotating' determines whether the sample is rotating in respect to the XRF detector, or if the XRF detector angle stays fixed.

The main window contains setup parameters, which can be enabled for fitting: A divergence value each for GIXRF and XRR calculations, a parameter for the width of the sample inspected by the detector, as well as slope and intercept for a linear background model for the XRR calculation.

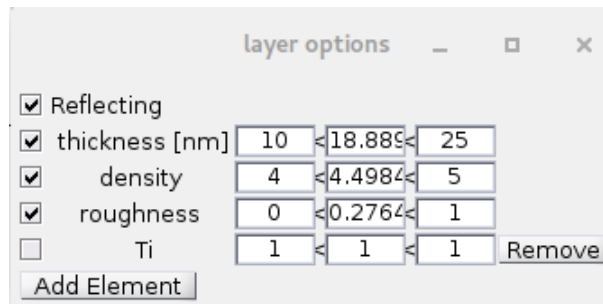


Figure 36: Dialog window for layer options.

4.4.3 Sample model

The sample area of the main windows contains a list of the objects, which constitute the sample model. Different types of objects can be added to the sample model: an arbitrary number of layers or stacks of layers, up to one implantation profile and exactly one substrate. Clicking on an object in the listbox will open the respective property dialog. The sample also has a length and offset (from center) property, which are used to calculate the beam footprint on the sample as described in section 2.3.2.

Layers are the most basic object type, which have thickness, density and roughness as their properties. As shown in Figure 36, elements can be added to or removed from a layer in order to construct a material. For layers consisting of a single element, the initial density will be read from the internal database. For mixed layers the density has to be entered by the user, as the software does not contain a database of materials. The 'reflecting' property of a layer can be disabled to calculate only transmission, which can be useful to simulate residue or particles on the surface of a sample.

Stacks are basically (possibly repeating) aggregations of layers (Figure 37). The properties of the constituting layers are the same as for the case of a singular layer. A stack can be set to repeat the entered layers, which is convenient to simulate multilayer samples.

Implantation profiles are described by one or several distribution functions and a total implanted dose. A wide range of distribution functions is available for selection, among them the beta, gamma and normal distribution. Also available is the Pearson distribution system [83, 84], which is a superset of many common distributions and was already used producing good results for the modeling of implantation profiles [85, 86]. As shown in Figure 38, the resulting concen-

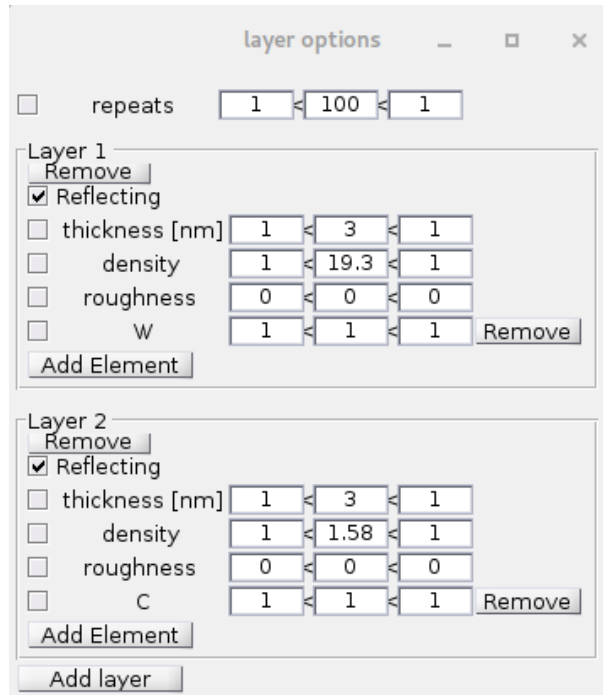


Figure 37: Dialog window for stack options.

tration profile is then discretized up to a maximum depth, as entered by the user. Subsequently atoms of the implantation profile will be substituted for atoms in the also discretized layered sample model. The number of atoms replaced by each implant atom is equal to the 'substitution factor' specified.

Owing to the combination and collaboration with SIMS in the beginning of our work, there is also the possibility to import a SIMS profile and quickly fit it with distribution functions as an initial guess.

The substrate is the bottommost object in the sample model and cannot be removed. It is a basic layer with density and roughness, but with intrinsic infinite thickness, which cannot be changed. The composition defaults to pure Silicon, but can be changed like for common layers.

4.4.4 Fit and optimization algorithm

The desired optimization algorithm can be selected from a drop-down list and options like the maximum number of iterations or a limit for the chi-squared value can be set in an options dialog. If the checkbox 'Allow angle offset' is enabled, the algorithm will allow small shifts in the angle. This can be used to compensate for small miscalibrations of the imported scan data. The measure, which is used for the calculation of the chi-squared for XRR data (see section

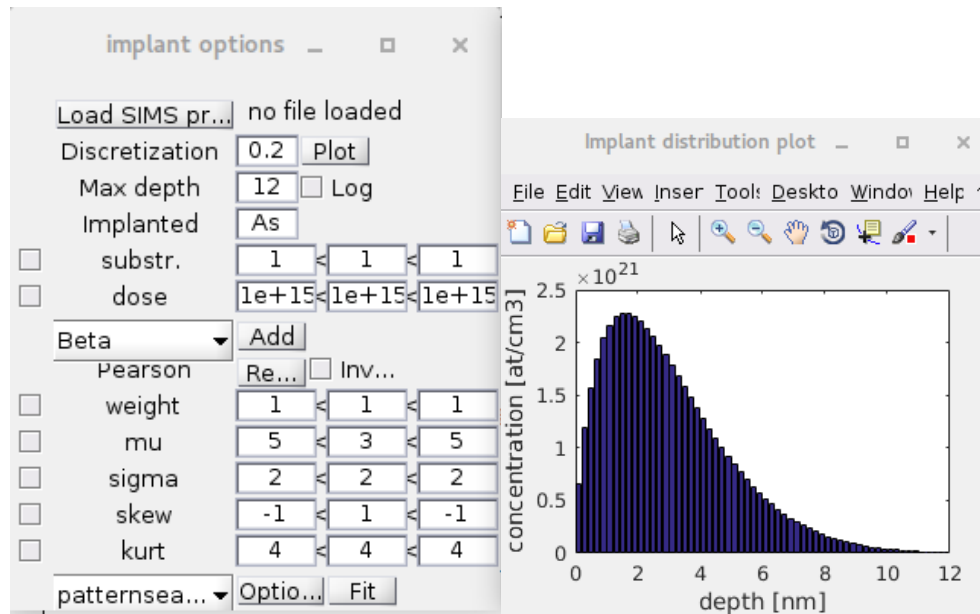


Figure 38: Dialog window for implant options.

4.1), is also selected here. An optimization using the currently selected values is started by clicking the 'Fit' button. The starting positions for the algorithms which use a population of candidate solutions (GA,DE,PSO) consist of one population member with the currently entered parameters and randomly selected vectors from the search-space.

The actual chi-squared value will be calculated and displayed every time a simulation is plotted, if measurement data are currently loaded.

4.4.5 Data plot

The result of a calculation with the actual parameters can be plotted in the plot area of the main window or in a separate window. The line to be plotted can be selected by clicking on the corresponding entry in the list in the upper left part of the main window. If applicable measurement data are loaded, they will also be plotted with the calculated data. By default the plot area or window will be cleared before plotting a new curve. The 'Hold' checkbox can be used, if the current plot should be retained, e.g. to create a single figure with multiple data curves. Font and font size, as well as zoom range of the plot can be adjusted. Finally the figure can be exported to several common picture formats (png,tif,eps).

4.4.6 Load and Save

The File menu provides the possibility to load or save a complete JGIXA evaluation project, which includes the experimental setup, the sample model and

imported measurement data. The user can also opt for loading only part of a project file, which can be useful to reuse an already characterized experimental setup for evaluation of unknown samples or to use the model of a well-known reference sample to characterize a new setup (section 5.1).

5 Applications

After introduction to the theoretical aspects of the calculation, the evaluation and our instrumentation, we showcase now some practical applications of the GIXA technique. The presented applications were motivated by the needs of and developed in cooperation with several collaboration partners.

The characterization of layers presented in section 5.2 was performed in cooperation with CEA-Leti, Grenoble, i.e. mainly E. Nolot and B. Caby, who provided many samples. More details on the results of this work can be found in publications by Caby et al. [87] and Rotella et al. [88], as well as the doctoral thesis of B. Caby [57].

Our work on ion implanted samples in section 5.3 was a continuation of the collaboration from the European Integrated Activity of Excellence and Networking for Nano and Micro-Electronics Analysis (ANNA), mainly with G. Pepponi, D. Giubertoni and E. Demenev from FBK, Trento. The results were published by Ingerle et al. [89].

Finally, the preliminary results on nanoparticles in section 5.4 originated from a collaboration with F. Meirer and J. Zecevic from the Debye Institute for Nanomaterials Science, Utrecht University. The data were presented in the poster session of the 16th International Conference on Total Reflection X-ray Fluorescence Analysis and Related Methods (TXRF 2015) [90].

5.1 Instrument characterization

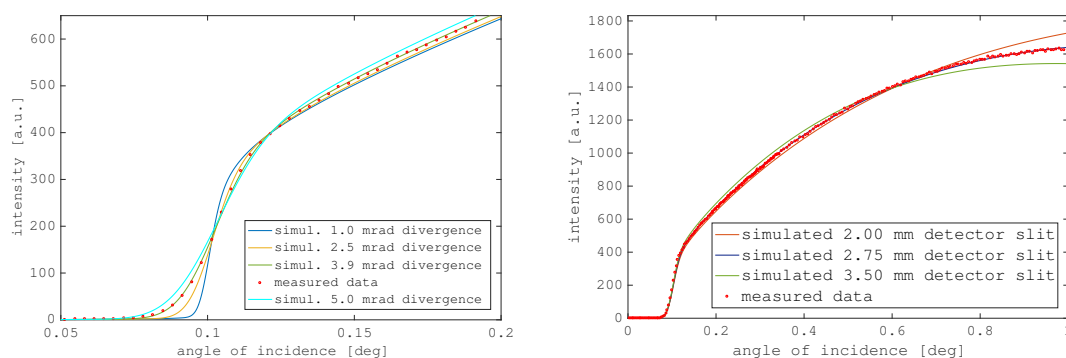


Figure 39: Determination of divergence and detector geometry

An important aspect and application, which can and should be done prior to the evaluation of unknown samples, is the characterization of the measurement setup. The instrumental parameters, which consist mainly of the angular

divergence of the beam and the beam-sample-detector geometry, have a considerable influence on the measured curves and are included in the simulation as described in section 2.3. Typically we would use a stable and well-known reference sample for this purpose, e.g. a pure silicon wafer as shown in Figure 39 or a Ni layer on silicon as in section 3.3. Additionally reference samples of known composition can be used to determine the relative sensitivity factors of the instrument for different XRF lines, like in our measurements of ion implanted samples as presented in section 5.3, where we used a reference sample with $7.99E14$ atoms of arsenic per cm^2 for the quantification. Generally the measurement of reference samples should be performed during each measurement cycle, possibly repeatedly, to increase confidence in the result and the instrumentation. Furthermore the determination in advance of these instrumental parameters typically improves the fitting results as it reduces the number of variable parameters.

5.2 Layers

A typical and relatively straightforward application of the combined GIXRF and XRR analysis is the characterization of layers with thicknesses in the nanometer range. In the sections below we show for demonstration purposes measurements and fit results of a Nickel reference and a Titanium test sample, as well as a research sample of In_2O_3 and Ag layers for photovoltaic applications. All samples were provided by B. Caby and E. Nolot of CEA-LETI, Grenoble.

5.2.1 Nickel layer

Figure 40 shows the XRR and GIXRF measurement data for a nominally 50 nm thick layer of pure Nickel on Silicon substrate, together with the result obtained by fitting with the JGIXA software. The best fit model consisted of a 2nm low density (3.7 g/cm^3) oxide surface layer with a roughness of 1 nm and a pure Ni layer with a thickness of 52.5 nm, a density of 8.5 g/cm^3 and a roughness of 0.98 nm. The measurements were performed in the table-top spectrometer (section 3.1) using Molybdenum $K\alpha$ excitation.

5.2.2 Titanium layer

Figure 41 shows fitted data for a layer of Titanium with a nominal thickness of 18 nm on a Silicon substrate. Two additional surface layers of TiO_2 had to be included in the model (Table 1), in order to obtain a good fit result. This can be readily explained by an inhomogeneous surface oxidation of the Titanium due

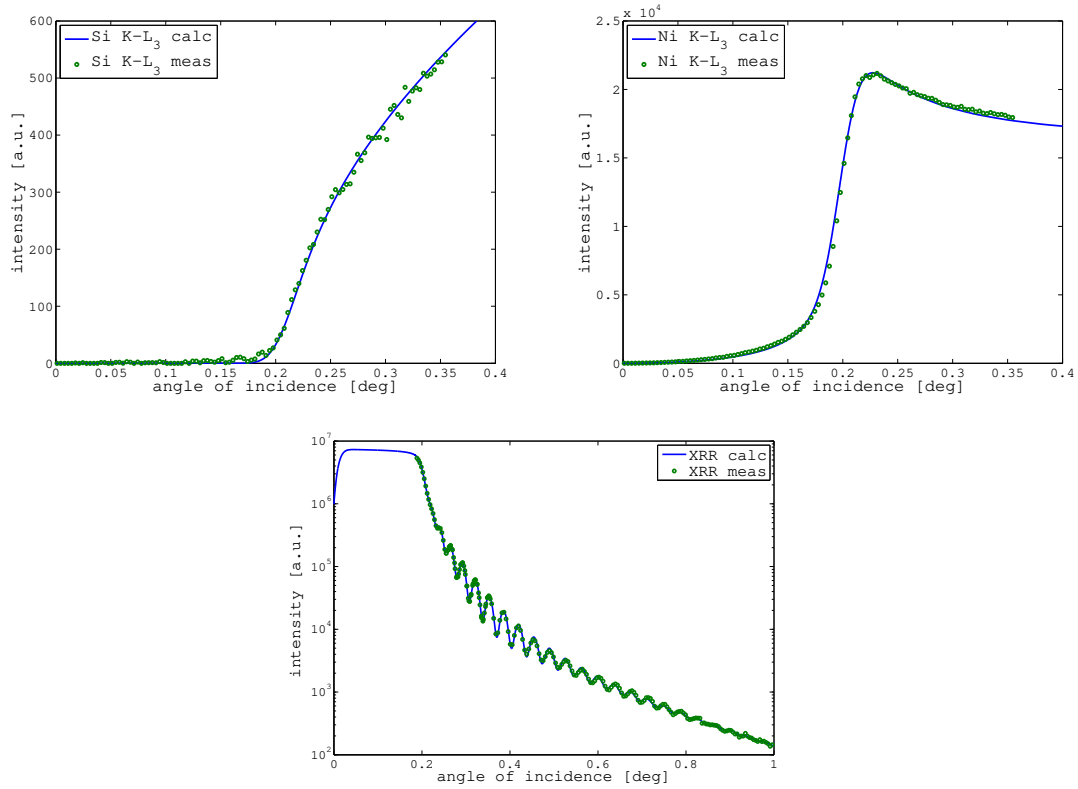


Figure 40: Combined fit for 50nm of Ni on Si including Si K-L₃ and Ni K-L₃ GIXRF data as well as XRR data.

	Thickness [nm]	Density [g/cm ³]	Roughness [nm]
TiO ₂	0.9	3.5	0.8
TiO ₂	3.9	4.1	0.1
Ti	18.9	4.5	0.3

Table 1: Layer model for the best fit result of a nominal 18 nm Titanium layer on Silicon.

to the exposure to the Oxygen in the air. The measurements were performed in our table-top spectrometer (section 3.1) with Molybdenum K α excitation.

5.2.3 In₂O₃ and Ag layers

As a somewhat more intricate example we present the analysis of samples with layers of In₂O₃ and Ag, which were carried out in cooperation with B. Caby and E. Nolot of CEA-LETI, Grenoble and published in [87] as well as presented in the doctoral thesis of B. Caby [57].

A set of four samples, with a 6 nm Ag layer embedded between two In₂O₃ layers deposited on a 500 nm SiO₂/Si substrate, was prepared with physical vapor deposition at CEA-LETI. Two samples were annealed at 200 °C before measurement, while the other two were measured as deposited. The samples

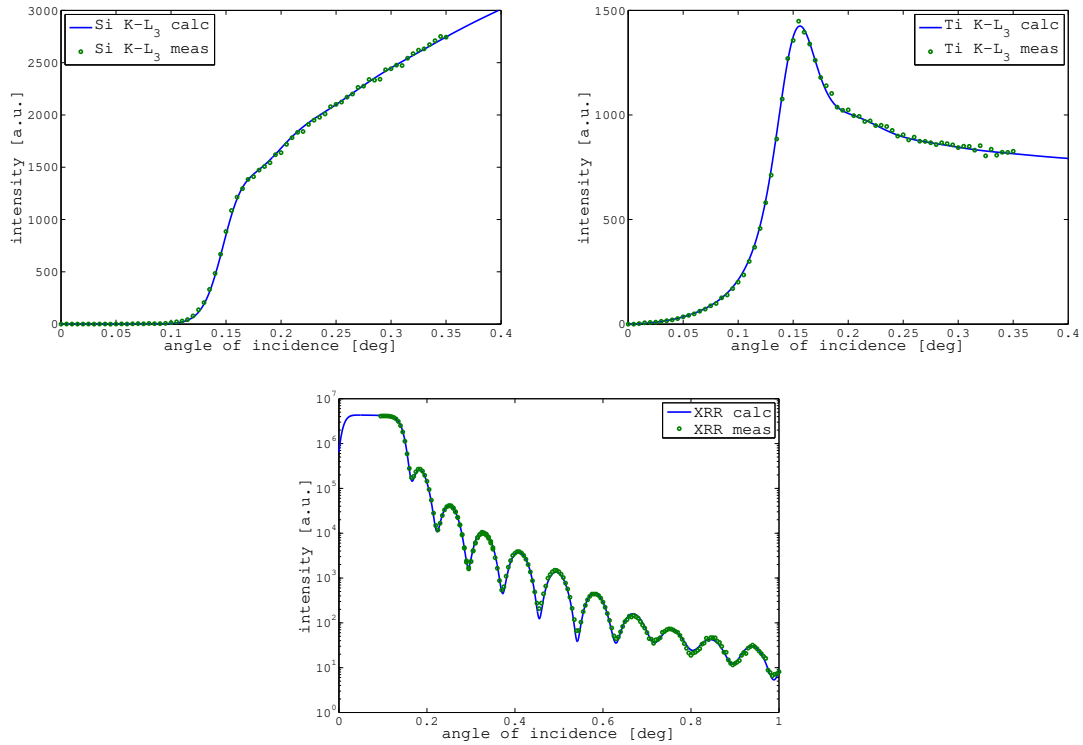


Figure 41: Combined fit for a nominally 18 nm thick Titanium layer deposited on Silicon: Si K-L₃ and Ti K-L₃ GIXRF data and XRR data.

were measured at the Atominstitut with Cu K α in the instrument described in Figure 18 as well as on the Gilda (BM08) line at ESRF, Grenoble. The synchrotron measurements were performed at 26,400 eV, i.e. above the Ag-K but below the In-K edge, in order to improve the sensitivity for the Ag-K lines.

All evaluations of reflectivity and fluorescence measurements were carried out using the JGIXA software (section 4.4).

	Thickness [nm]	Density [g/cm ³]
LD-In ₂ O ₃	2	6.12
In ₂ O ₃	16.3	7.18
In ₂ O ₃ ;Ag	1.1	8.36
Ag	5.7	9.9
In ₂ O ₃ ;Ag	0.6	7.47
In ₂ O ₃	40	7

Table 2: Thickness and densities of the sample D obtained from correlating JGIXA fits of the experimental data measured at two different energies (respectively 26.4 and 8.05 keV). (from [87]) (LD = low density)

The final model for the annealed sample D as presented in Table 2 was obtained by a combined fit of the XRR obtained in the laboratory and the Ag-K α from the synchrotron (Figure 42). Thin intermixing layers were added between

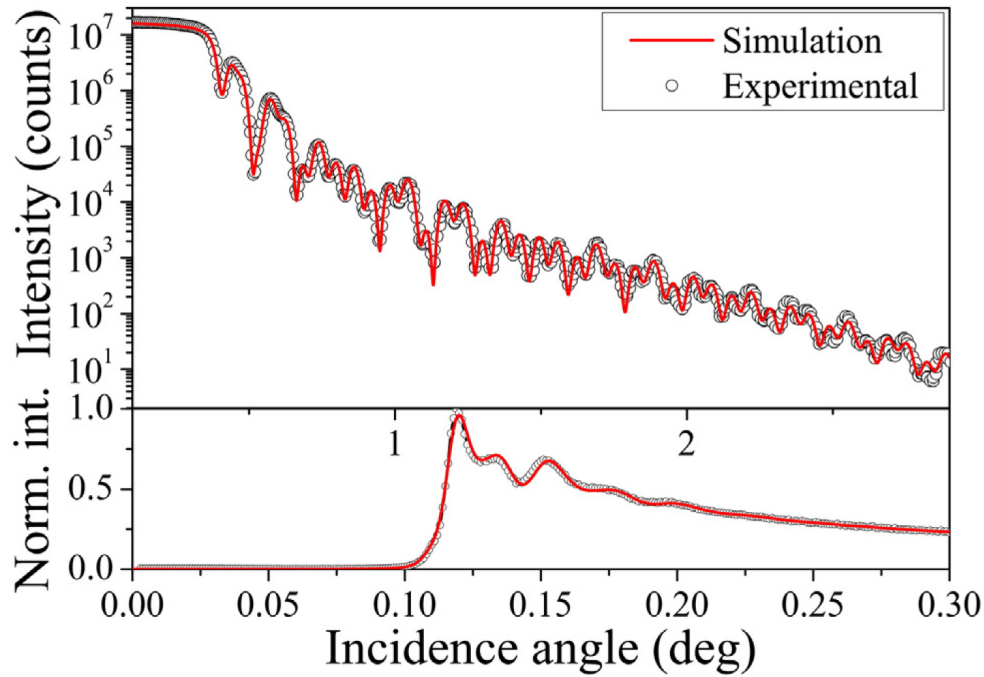


Figure 42: XRR and GIXRF measurements and fitting of the sample D with reflectivity measured at 8.05 keV and fluorescence at 26.4 keV. (from [87])

In_2O_3 and Ag to obtain a good fit and were interpreted as interdiffusion induced by the annealing.

5.3 Ion implanted samples

The characterization of (ultra-)shallow dopant distributions in semiconductors has historically been a challenge for micro-electronics technology. Advances in the fabrication have been connected to shallower and shallower distributions and increasing dopant concentrations. GIXRF has been used in the past for the evaluation of dilute near surface dopant profiles, but these previous investigations e.g. by Pepponi et. al. [17] used physical models for the simulation of the fluorescence intensities and the quantification of the dose, which did not consider the modification of the x-ray optical constants of the substrate material due to the dopant.

In our new approach we use a discretized layer model of the first few nanometers of the substrate and replace substrate atoms by implant atoms as shown in Figure 43 for Arsenic in Silicon. The optical constants of the layers are then calculated from the scattering factors of the respective atoms.

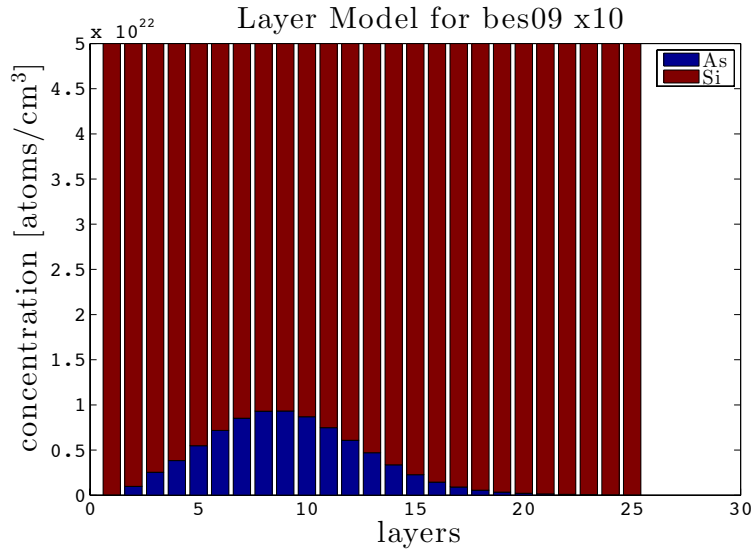


Figure 43: A discretized layer model of the Arsenic implant distribution in the Silicon substrate.

5.3.1 Influence of Implanted Dose

To give our calculations a realistic starting point, we used data from a SIMS depth profile for a sample implanted with Arsenic for a total dose of $7.99\text{E}14$ atoms per cm^2 at 5 keV implantation energy, which was measured by cooperation partners Giubertoni et al. at Fondazione Bruno Kessler [18]. The depth profile was scaled to simulate different implantation doses and transformed to a layer model with 25 layers and 1 nanometer per layer. The Arsenic atoms were assumed to replace Silicon atoms; the total number of atoms was therefore kept constant. The scaled depth profiles were used to determine the influence of different implantation doses (with the same depth distribution) on the Arsenic and the Silicon curve. The results were normalized relative to the unmodified profile and the As intensities were scaled according to their dose (Figure 44).

As expected the As curve loses its peakedness with higher concentrations and the Si curve also changes already for a dose of $4\text{E}15$ atoms/ cm^2 .

5.3.2 Influence of Layer Model

To verify that the resolution of our model with 25 layers and 1 nanometer per layer is enough, we compared the calculation results for discretizations of the first 25 nm in 10, 25 and 100 layers for a profile with an total implanted dose of $7.99\text{E}14$ atoms of Arsenic per cm^2 . Figure 45 shows that the curves for 100 and 25 layers are practically identical, while the 10 layer model shows small but noticeable differences in the As curve.

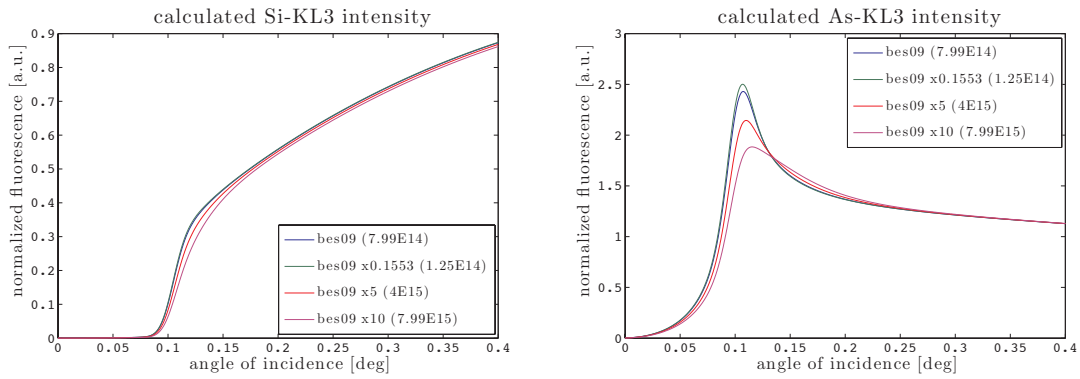


Figure 44: Normalized calculated intensities for the same profile shape with varying implanted dose.

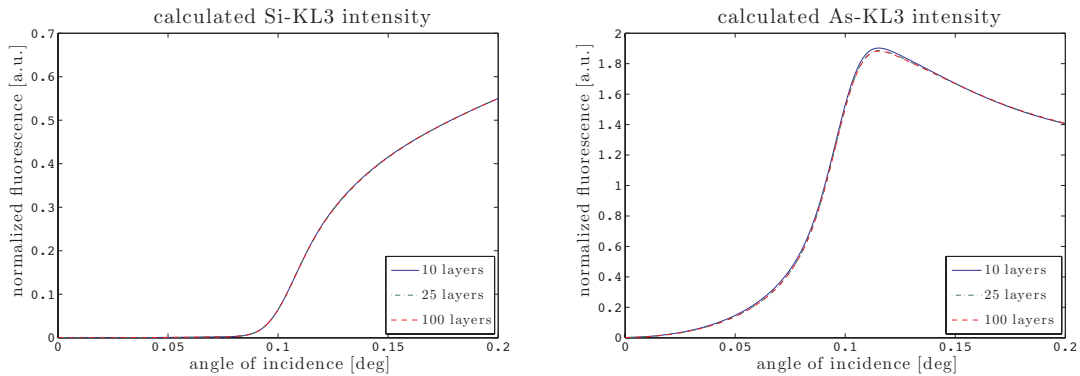


Figure 45: Comparison of calculated Si K-L₃ and As K-L₃ intensities for the same implant distribution function with different discretization.

5.3.3 Comparison with other techniques

Silicon wafers implanted with Arsenic were used to test the above-described approach. We investigated two sets of samples: one with a constant nominal fluence of $1\text{E}15$ atoms/cm² and implantation energies of 0.5, 2, and 3 keV and one with a constant implantation energy of 2 keV and varying nominal fluence of $1\text{E}14$, $5\text{E}14$ and $1\text{E}15$ atoms/cm² (details can be found in Table 3). The total dose measurements by INAA (performed by G. Steinhauser at the Atominstitut) and SIMS (E. Demenev and D. Giubertoni of Fondazione Bruno Kessler, Trento, Italy) are published in [19] and additional SIMS profiles are published in [76].

The following figures report the fit results to the experimental data collected for the samples described above, as obtained by the JGIXA program. Figure 46 shows the fit results for the Si signal, the As signal and the XRR signal for the samples with the same dose ($1\text{E}15$ atoms/cm²) but different implantation energy (0.5, 2, 3 keV), following the sample description in Table 3. The fits of all curves

Sample	Implant energy [keV]	Dose nominal [at/cm ²]	Dose JGIXA [at/cm ²]	Dose NAA [at/cm ²]	Dose SIMS 500eV [at/cm ²]	Dose SIMS 350eV [at/cm ²]	Dose SIMS 250eV [at/cm ²]
As1	0.5	1E15	1.11E15	1.13E15	1.06E15	1.01E15	9.80E14
As3	2.0	1E15	1.10E15	1.13E15	1.02E15	1.07E15	1.11E15
As4	3.0	1E15	1.09E15	9.87E14	1.06E15	1.08E15	1.08E15
As6	2.0	1E15	1.17E14	1.03E14	1.10E14	1.00E14	1.03E14
As7	2.0	5E14	5.67E14	5.59E14	5.50E14	5.50E14	5.46E14

Table 3: Samples description and dose determined by GIXRF using the program JGIXA in comparison to other techniques.

are in good agreement with the measured data points.

In Figure 47 the implantation profiles obtained from JGIXA in comparison to SIMS measurement data of Demenev et al. [76] are shown. The profile of sample As4 (3 keV implantation energy) shows the best correlation with the SIMS profile, while the profile of sample As3 (2 keV implantation energy) shows a slight deviation from the SIMS profile in the direction of increasing depth, but reporting the same total dose. The profile of sample As1 (0.5 keV implantation energy) shows a deviation of 1 nanometer in the mean implantation depth in the direction to increasing depth and also slight differences in the dose distribution.

Figure 48 shows the fits for samples with same implantation energy (2 keV), but different implantation dose (1E15, 1E14, 5E14 atoms/cm²).

In Figure 49 the implantation profiles obtained from JGIXA in comparison with SIMS data from [76] are reported. The profile of sample As3 (1E15 atoms/cm²) shows the best agreement with the SIMS profile. The profile of sample As6 (1E14 atoms/cm²) shows a deviation of 1 nm of the mean implantation depth from the SIMS profile in the direction of increasing depth, but the same total dose. The profile of sample As7 (5E14 atoms/cm²) shows a slight deviation in the mean implantation depth in the direction to increasing depth and also slight differences in the dose distribution.

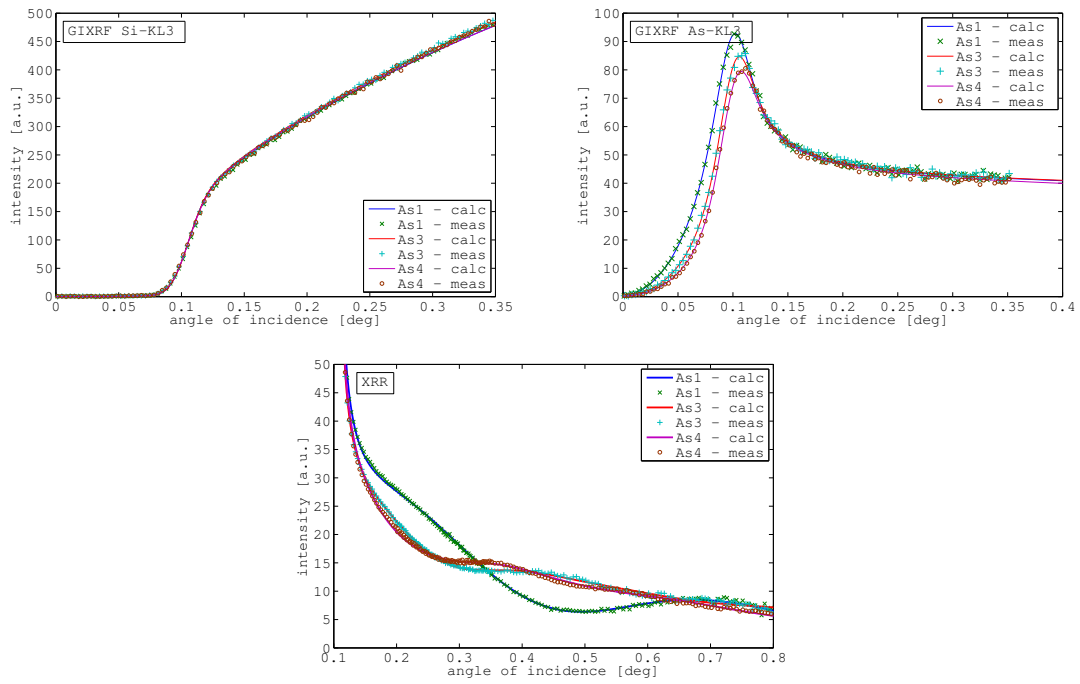


Figure 46: GIXRF and XRR for sample As1, As3, As4; same dose ($1E15$), different implantation energy (0.5,2,3keV).

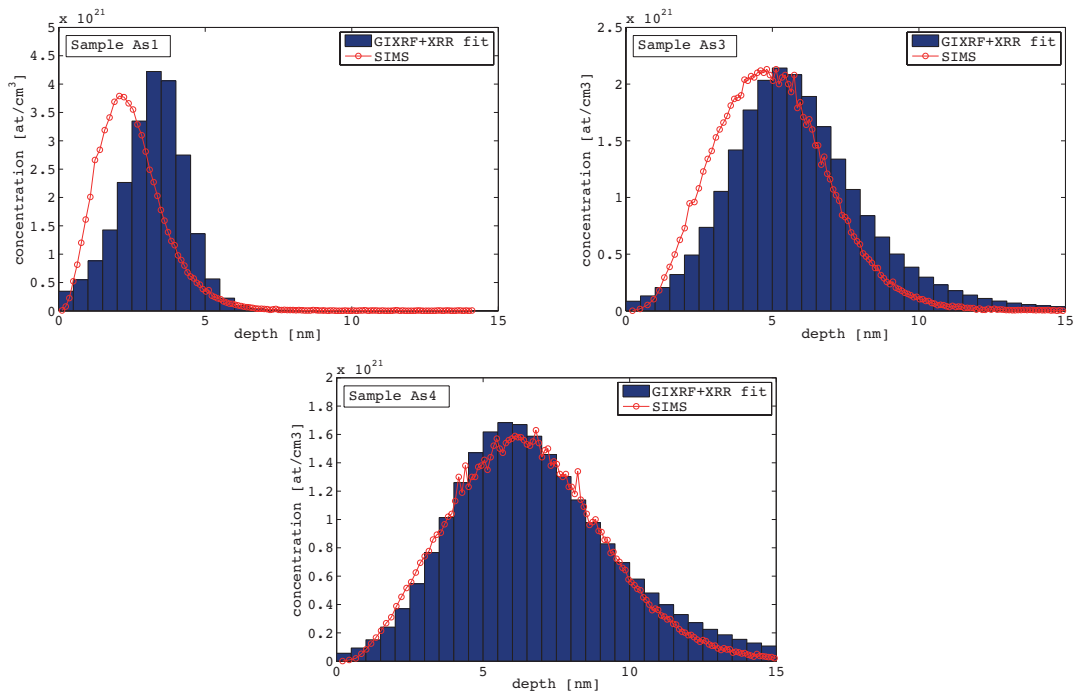


Figure 47: Depth profiles for fits in Fig.4 (As1, As3, As4) and SIMS from [76].

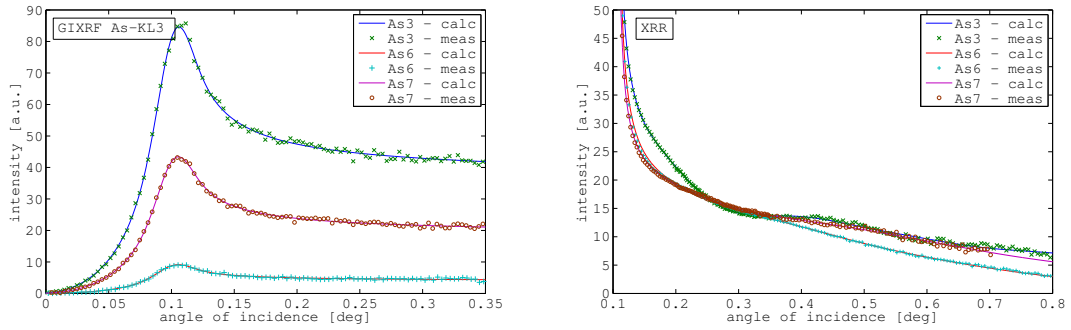


Figure 48: GIXRF-As signal and XRR measurement and fitting for sample As3, As6 and As7; same implantation energy (2keV), different dose (1E15, 1E14, 5E14).

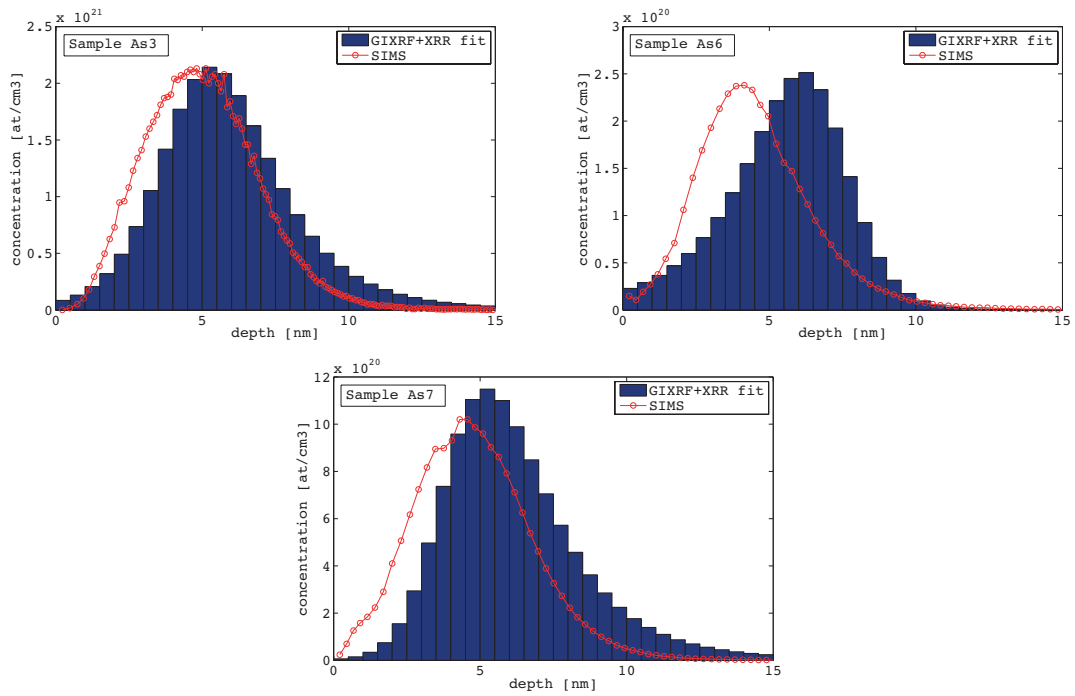


Figure 49: Depth profiles for fits in Fig.6 (As3,As6,As7) and SIMS from [76].

5.3.4 Depth-sensitivity of the method

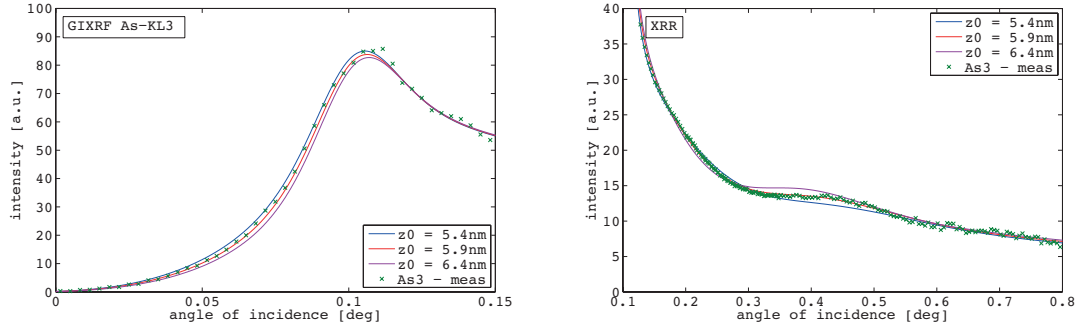


Figure 50: Simulations of depth variations of 0.5 nm around the mean implantation depth in both directions, both the GIXRF As curve as well as the XRR curve show significant discrepancies between simulation and experimental data which are also manifested in an increased chi squared value.

The discrepancy between the results and the SIMS profiles shown in the previous section 5.3.3 motivated an investigation of the sensitivity of the fits to changes in implantation depth. Figure 50 shows the results for a change of the mean implantation depth (z_0) of 0.5 nanometer in both directions towards increasing depth or more shallow depth. The GIXRF Arsenic angle curve as well as the XRR data both show a significant discrepancy between simulation and experimental data for these just 0.5 nanometer shifts, highlighting the high sensitivity of the presented method.

5.4 Nanoparticles

Our work on nanoparticles was initiated by colleagues at the Debye Institute for Nanomaterials Science, Utrecht University. Their question was whether we could use GIXRF and the XSW to determine size and homogeneity of metal nanoparticles, which can be used for Catalysis [91]. The standard methods for the characterization of nanoparticles, Transmission Electron Microscopy (TEM) and Scanning Electron Microscopy (SEM), are limited in sample area, can require special sample preparation and are quite expensive. An investigation by GIXRF on the other hand probes a relatively large area of some mm^2 in one scan, is relatively uncomplicated and inexpensive.

Previous work by Tiwari et al. [92, 31] and von Bohlen et al. [53, 93] suggested that XSW measurements of very small nanoparticles, i.e. in the range of some nanometers, on pure silicon wafers are difficult to evaluate, due to the relatively small critical angle and thus limited angular range. The answer of Tiwari et al. [31] was to use a W/C multilayer. This increases the critical angle and also adds a

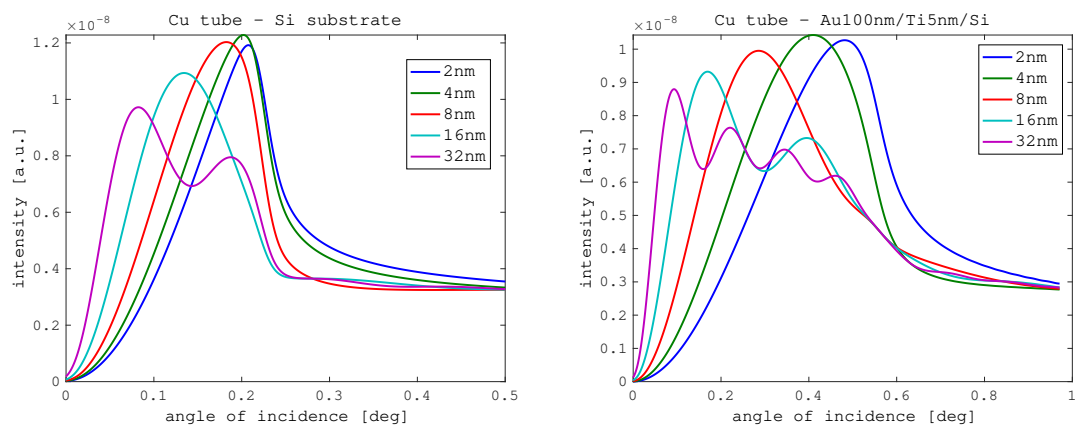


Figure 51: Simulations for comparison of GIXRF intensities of nanoparticles on Si (left) and on 100 nm Au/5 nm Ti/Si (right).

strong reflection near the Bragg angle. Nevertheless we looked for other options as multilayers could introduce additional uncertainties, if the layer thickness is not homogenous over the whole area, and high quality large area multilayers are also still quite expensive for basically one shot sample carriers. A coating of silicon with a single thick layer of a high density material should provide a similar significant increase in critical angle and in fact simulations with nanoparticles on a commercially available gold/titanium/silicon substrate were quite promising as shown in Figure 51. A thin layer of titanium is included in these coated wafers to increase the adhesion of the gold layer. The simulations were performed by using non-reflecting layers in the model for the nanoparticles.

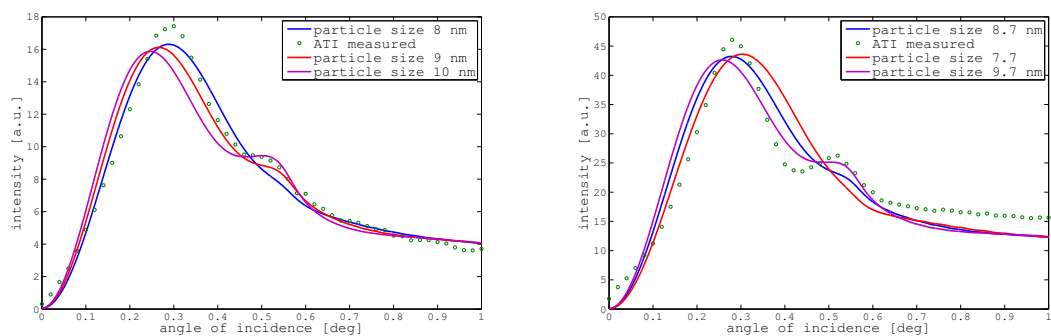


Figure 52: GIXRF scans of Fe $K\alpha$ of iron nanoparticles on 100 nm Au/5 nm Ti/Si performed in our lab spectrometer.

Subsequently iron nanoparticles were deposited on a gold layer on silicon substrate by J. Zecevic from the Debye Institute for Nanomaterials Science, Utrecht University. We performed measurements using Cu $K\alpha$ radiation in our lab spectrometer (section 3.1) and at an equivalent primary energy of 8.04 keV at the

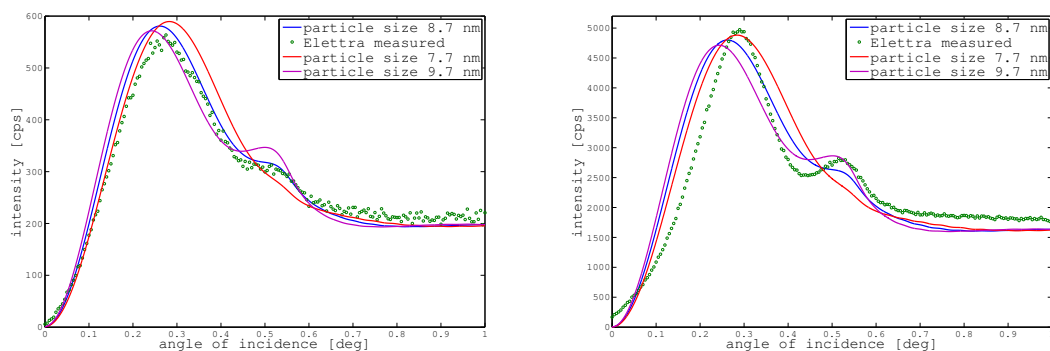


Figure 53: GIXRF scans of Fe $K\alpha$ of iron nanoparticles on 100 nm Au/5 nm Ti/Si performed at Elettra.

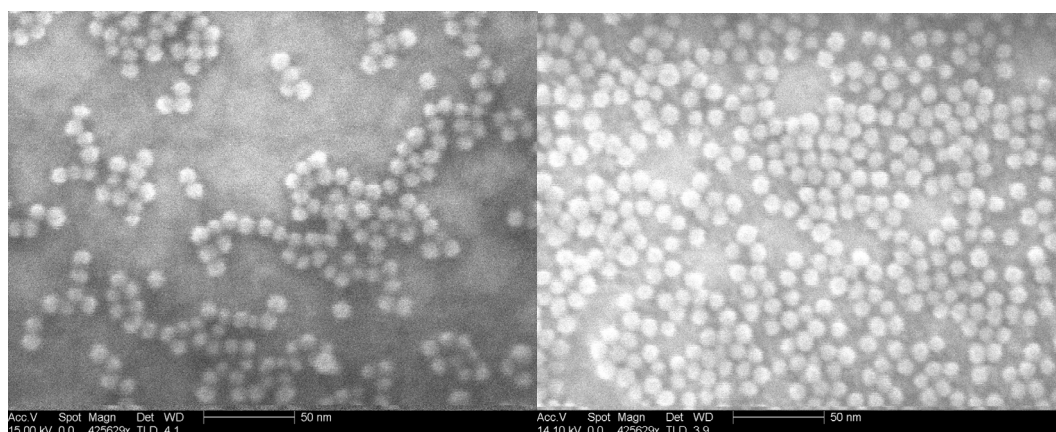


Figure 54: SEM images of iron nanoparticles (performed at Utrecht University).

X-ray fluorescence (10.1L) beamline of Elettra Sincrotrone Trieste (section 3.3.2). In both cases several measurements were performed at different spots of the sample. The measurement time per point of the GIXRF angle scan was 10s with a 100 μm wide beam at the synchrotron and 900s with a 1 mm wide beam in the lab. Both measurements show differences in particle density (i.e. XRF intensity) for different spots, which corresponds with SEM images of the samples. The best fits, especially for the area with low particle density, are obtained for particle sizes between 7 and 10 nanometer, which is in good agreement with results from SEM images (8-9nm) performed at Utrecht University.

6 Concluding remarks

A software for the combined evaluation of GIXRF and XRR measurements has been developed and the theoretical influence of the limited coherence of the beam has been investigated. At the same time suitable instrumentation has been designed and implemented in the form of a table-top spectrometer and the adaptation of an X-ray diffraction system. The many experiments and evaluations of them, which were performed in cooperation with different partners, helped to test and improve the program and the spectrometers.

Especially the combined analysis of arsenic implanted silicon wafers in cooperation with FBK, Trento, was very successful and in fact the first of its kind. The depth profiles and dose quantifications of the analysis were in good agreement with the results obtained by other techniques. A sensitivity for changes in the depth of less than 0.5 nm was achieved.

Also the analysis of many different layered samples, which was performed in collaboration with CEA-Leti, Grenoble, was insight- and fruitful. Furthermore the input and feedback, which resulted from this cooperation, helped to improve the software and the instrumentation.

The investigation and characterization of nanoparticles in cooperation with colleagues from Utrecht University were promising and show the general applicability of the developed tools for this type of problem.

In view of these numerous good results it can be stated with confidence, that the software and instrumentation work properly and reliable. The table-top spectrometer with its custom acquisition software provides a convenient and stable tool for angle scans, which can take several hours or even days for samples with low concentration. The relative ease of use of the program should help to spread the knowledge about GIXA and lead to new applications for the technique. With this objective in mind, the software and other tools related to GIXA will be available at the project website[94].

Certainly there are also necessities and opportunities for further research and development.

On the instrumentation side, the table-top spectrometer would benefit from the increase in intensity of a parallel beam mirror. This would drastically reduce the time consumption of the scans. Furthermore the XRF detector at the Empyrean should be mounted on a more stable and robust attachment module.

On the simulation and software side, there are several different aspects which present themselves for further work. The margins of error of the combined GIXA

technique should be investigated similar to work on XRR by Tiilikainen et al. [24, 95]. Especially the case of correlated parameters can be difficult to handle, thus the convergence properties and fitting accuracy should be studied further. The model for the calculation of intensities in the case of nanoparticles currently assumes an unaltered XSW above the surface of the substrate. In the case of larger particles or higher particle density this assumption might no longer be justified, hence the field alterations due to the particles should be investigated. Finally, the technique as a whole would benefit from further speedup of the calculation and evaluation. This could be achieved by general-purpose computing on graphics processing units (GPGPU) or cloud computing.

References

- [1] W. C. Röntgen, Über eine neue Art von Strahlen. (Vorläufige Mittheilung.), Sitzungsberichte der Würzburger Physik.-medic. Gesellschaft (1895) 137–147.
- [2] A. H. Compton, CXVII. The total reflexion of X-rays, Philosophical Magazine Series 6 45 (270) (1923) 1121–1131. doi:10.1080/14786442308634208. URL <http://www.tandfonline.com/doi/abs/10.1080/14786442308634208>
- [3] J. A. Prins, The Total Reflection of X-rays, Nature 120 (3014) (1927) 188–189. doi:10.1038/120188a0. URL <http://www.nature.com/doi/abs/10.1038/120188a0>
- [4] H. Kiessig, Interferenz von Röntgenstrahlen an dünnen Schichten, Annalen der Physik 402 (7) (1931) 769–788. doi:10.1002/andp.19314020702. URL <http://doi.wiley.com/10.1002/andp.19314020702>
- [5] L. Parratt, Surface Studies of Solids by Total Reflection of X-Rays, Physical Review 95 (2) (1954) 359–369. doi:10.1103/PhysRev.95.359. URL <http://link.aps.org/doi/10.1103/PhysRev.95.359>
- [6] P. Croce, L. Névoit, Étude des couches minces et des surfaces par réflexion rasante, spéculaire ou diffuse, de rayons X, Revue de Physique Appliquée 11 (1) (1976) 113–125. doi:10.1051/rphysap:01976001101011300. URL <http://www.edpsciences.org/10.1051/rphysap:01976001101011300>
- [7] R. Becker, J. Golovchenko, J. Patel, X-Ray Evanescent-Wave Absorption and Emission, Physical Review Letters 50 (3) (1983) 153–156. doi:10.1103/PhysRevLett.50.153. URL <http://golovchenko.physics.harvard.edu/XrayEvanescentWaveAbsorption.pdf><http://link.aps.org/doi/10.1103/PhysRevLett.50.153>
- [8] J. M. Bloch, M. Sansone, F. Rondelez, D. G. Peiffer, P. Pincus, M. W. Kim, P. M. Eisenberger, Concentration Profile of a Dissolved Polymer near the Air-Liquid Interface: X-Ray Fluorescence Study, Physical Review Letters 54 (10) (1985) 1039–1042. doi:10.1103/PhysRevLett.54.1039. URL <https://link.aps.org/doi/10.1103/PhysRevLett.54.1039>
- [9] D. de Boer, X-ray Standing Waves and the critical sample thickness for Total-reflection X-Ray Fluorescence analysis, Spectrochimica Acta Part B: Atomic

- Spectroscopy 46 (10) (1991) 1433–1436. doi:10.1016/0584-8547(91)80194-8.
URL <http://linkinghub.elsevier.com/retrieve/pii/0584854791801948>
- [10] D. de Boer, W. van den Hoogenhof, TXRF of thin layers on and in solids, *Adv. X-Ray Anal.* 34 (1991) 35.
- [11] D. De Boer, W. Van Den Hoogenhof, Total reflection X-ray fluorescence of single and multiple thin-layer samples, *Spectrochimica Acta Part B: Atomic Spectroscopy* 46 (10) (1991) 1323–1331. doi:10.1016/0584-8547(91)80181-2.
URL <http://linkinghub.elsevier.com/retrieve/pii/0584854791801812>
- [12] D. de Boer, Glancing-incidence x-ray fluorescence of layered materials, *Physical Review B* 44 (2) (1991) 498–511. doi:10.1103/PhysRevB.44.498.
URL <http://link.aps.org/doi/10.1103/PhysRevB.44.498>
- [13] D. de Boer, W. van den Hoogenhof, A. J. G. Leenaers, The profile of layered materials reflected by glancing-incidence X-ray analysis, *Applied Physics A Solids and Surfaces* 58 (3) (1994) 169–172. doi:10.1007/BF00324372.
URL <http://www.springerlink.com/index/10.1007/BF00324372>
- [14] D. de Boer, A. J. G. Leenaers, W. van den Hoogenhof, Glancing-incidence x-ray analysis of thin-layered materials: A review, *X-Ray Spectrometry* 24 (3) (1995) 91–102. doi:10.1002/xrs.1300240304.
URL <http://onlinelibrary.wiley.com/doi/10.1002/xrs.1300240304/abstract>
<http://doi.wiley.com/10.1002/xrs.1300240304>
- [15] W. Van Den Hoogenhof, D. De Boer, Glancing-incidence X-ray analysis, *Spectrochimica Acta Part B: Atomic Spectroscopy* 48 (2) (1993) 277–284. doi:10.1016/0584-8547(93)80034-R.
URL <http://linkinghub.elsevier.com/retrieve/pii/058485479380034R>
- [16] W. van den Hoogenhof, D. de Boer, Glancing incidence X-ray analysis: Forgotten or to be discovered?, *Surface and Interface Analysis* 22 (1-12) (1994) 572–575. doi:10.1002/sia.7402201121.
URL <http://doi.wiley.com/10.1002/sia.7402201121>
- [17] G. Pepponi, C. Strelì, P. Wobrauschek, N. Zoeger, K. Luening, P. Pianetta, D. Giubertoni, M. Barozzi, M. Bersani, Nondestructive dose determination and depth profiling of arsenic ultrashallow junctions with total reflection X-ray fluorescence analysis compared to dynamic secondary ion mass

- spectrometry, *Spectrochimica Acta Part B: Atomic Spectroscopy* 59 (8) (2004) 1243–1249. doi:10.1016/j.sab.2004.04.014.
 URL <http://linkinghub.elsevier.com/retrieve/pii/S0584854704001405>
- [18] D. Giubertoni, G. Pepponi, B. Beckhoff, P. Hoenicke, F. Gennaro, F. Meirer, D. Ingerle, G. Steinhauser, M. Fried, P. Petrik, A. Parisini, M. Reading, C. Strel, J. van den Berg, M. Bersani, Multi-technique characterization of arsenic ultra shallow junctions in silicon within the ANNA consortium, *AIP Conference Proceedings* 1173 (2009) 45–49. doi:10.1063/1.3251258.
 URL <http://www.scopus.com/inward/record.url?eid=2-s2.0-70450228734&partnerID=tZ0tx3y1>
- [19] G. Pepponi, D. Giubertoni, M. Bersani, F. Meirer, D. Ingerle, G. Steinhauser, C. Strel, P. Hoenicke, B. Beckhoff, Grazing incidence x-ray fluorescence and secondary ion mass spectrometry combined approach for the characterization of ultrashallow arsenic distribution in silicon, *Journal of Vacuum Science & Technology B: Microelectronics and Nanometer Structures* 28 (1) (2010) C1C59. doi:10.1116/1.3292647.
 URL <http://link.aip.org/link/JVTBD9/v28/i1/pC1C59/s1?Agg=doi>
- [20] P. Hönicke, B. Beckhoff, M. Kolbe, D. Giubertoni, J. van den Berg, G. Pepponi, Depth profile characterization of ultra shallow junction implants., *Analytical and bioanalytical chemistry* 396 (8) (2010) 2825–32. doi:10.1007/s00216-009-3266-y.
 URL <http://www.ncbi.nlm.nih.gov/pubmed/19941133>
- [21] D. Ingerle, F. Meirer, N. Zoeger, G. Pepponi, D. Giubertoni, G. Steinhauser, P. Wobrauschek, C. Strel, A new spectrometer for grazing incidence X-ray fluorescence for the characterization of Arsenic implants and Hf based high-k layers, *Spectrochimica Acta Part B: Atomic Spectroscopy* 65 (6) (2010) 429–433. doi:10.1016/j.sab.2010.02.015.
 URL <http://dx.doi.org/10.1016/j.sab.2010.02.015><http://linkinghub.elsevier.com/retrieve/pii/S0584854710000467>
- [22] G. Reiss, R. Lipperheide, Inversion and the phase problem in specular reflection, *Physical Review B* 53 (13) (1996) 8157–8160. doi:10.1103/PhysRevB.53.8157.
 URL <http://link.aps.org/doi/10.1103/PhysRevB.53.8157>
- [23] S. Banerjee, S. Ferrari, D. Chateigner, a. Gibaud, Recent advances in char-

acterization of ultra-thin films using specular X-ray reflectivity technique, *Thin Solid Films* 450 (1) (2004) 23–28. doi:10.1016/j.tsf.2003.10.042.

URL <http://linkinghub.elsevier.com/retrieve/pii/S0040609003014172>

- [24] J. Tiilikainen, V. Bosund, M. Mattila, T. Hakkarainen, J. Sormunen, H. Lipsanen, Fitness function and nonunique solutions in x-ray reflectivity curve fitting: crosserror between surface roughness and mass density, *Journal of Physics D: Applied Physics* 40 (14) (2007) 4259–4263. doi:10.1088/0022-3727/40/14/023.

URL <http://stacks.iop.org/0022-3727/40/i=14/a=023?key=crossref.7f6ea22f079539123bce32cf0dcebdf1>

- [25] M. K. Tiwari, G. S. Lodha, K. Sawhney, Applications of the CATGIXRF computer program to the grazing incidence X-ray fluorescence and X-ray reflectivity characterization of thin films and surfaces, *X-Ray Spectrometry* 39 (2) (2010) 127–134. doi:10.1002/xrs.1215.

URL <http://doi.wiley.com/10.1002/xrs.1215>

- [26] M. K. Tiwari, G. Das, An interactive graphical user interface (GUI) for the CATGIXRF program - for microstructural evaluation of thin film and impurity doped surfaces, *X-Ray Spectrometry* 45 (4) (2016) 212–219. doi:10.1002/xrs.2692.

URL <http://doi.wiley.com/10.1002/xrs.2692>

- [27] F. Brigidi, G. Pepponi, GIMPY: a software for the simulation of X-ray fluorescence and reflectivity of layered materials, *X-Ray Spectrometry* 46 (2) (2017) 116–122. doi:10.1002/xrs.2746.

- [28] M. Bortolotti, L. Lutterotti, G. Pepponi, Combining XRD and XRF analysis in one Rietveld-like fitting, *Powder Diffraction* (2017) 1–6doi:10.1017/S0885715617000276.

URL https://www.cambridge.org/core/product/identifier/S0885715617000276/type/journal_{_}article

- [29] L. Lühl, C. Herzog, J. Eilbracht, B. Pollakowski, W. Jark, M. Krämer, B. Beckhoff, B. Kanngießner, D. Eichert, MARS (Modelling Angle Resolved Spectroscopy), a New Software for GIXRF (Grazing Incidence X-ray Fluorescence Analysis) Data Analysis; Presented in poster session at the EXRS 2014 in Bologna, Italy (2014).

- [30] B. Detlefs, G. Picot, E. Nolot, H. Rotella, G. Pepponi, F. Brigidi, B. Caby, M. Müller, P. Hönicke, B. Beckhoff, MedePy : a new software for the investigation of depth-dependent properties using X-rays; presented in oral session at the TXRF 2015 in Denver, USA (2015).
URL <http://www.dxcicdd.com/txrf/abstracts/T23.pdf>
- [31] M. K. Tiwari, K. Sawhney, T. Lee, S. Alcock, G. S. Lodha, Probing the average size of self-assembled metal nanoparticles using x-ray standing waves, *Physical Review B* 80 (3) (2009) 035434. doi:10.1103/PhysRevB.80.035434.
URL <http://link.aps.org/doi/10.1103/PhysRevB.80.035434>
- [32] G. Das, S. R. Kane, A. Khooha, A. Singh, M. K. Tiwari, Simultaneous measurements of X-ray reflectivity and grazing incidence fluorescence at BL-16 beamline of Indus-2 055102. doi:10.1063/1.4919557.
URL <http://dx.doi.org/10.1063/1.4919557>
- [33] J. Lubeck, M. Bogovac, B. Boyer, B. Detlefs, D. Eichert, R. Fliegau, D. Gröttsch, I. Holfelder, P. Hönicke, W. Jark, R. B. Kaiser, B. Kanngießner, A. G. Karydas, J. J. Leani, M.-C. Lépy, L. Lühl, Y. Ménesguen, A. Migliori, M. Müller, B. Pollakowski, M. Spanier, H. Sghaier, G. Ulm, J. Weser, B. Beckhoff, A new generation of x-ray spectrometry UHV instruments at the SR facilities BESSY II, ELETTRA and SOLEIL, in: *AIP Conference Proceedings*, Vol. 1741, 2016, p. 030011. doi:10.1063/1.4952834.
URL <http://aip.scitation.org/doi/abs/10.1063/1.4952834>
- [34] IAEA, XRF Newsletter No. 24, March 2013 (24).
- [35] Y. Ménesguen, B. Boyer, H. Rotella, J. Lubeck, J. Weser, B. Beckhoff, D. Gröttsch, B. Kanngießner, A. Novikova, E. Nolot, M.-C. Lépy, CASTOR, a new instrument for combined XRR-GIXRF analysis at SOLEIL, *X-Ray Spectrometry* (November 2016). doi:10.1002/xrs.2742.
URL <http://doi.wiley.com/10.1002/xrs.2742>
- [36] J. Lubeck, B. Beckhoff, R. Fliegau, I. Holfelder, P. Hönicke, M. Müller, B. Pollakowski, F. Reinhardt, J. Weser, A novel instrument for quantitative nanoanalytics involving complementary X-ray methodologies, *Review of Scientific Instruments* 84 (4). doi:10.1063/1.4798299.
- [37] R. James, *The Optical Principles of the Diffraction of X-rays*, Vol. II, 1962.
URL <http://www.archive.org/details/opticalprinciple031059mbphttp://www.slac.stanford.edu/spires/find/books?irn=128686>

- [38] D. Attwood, *Soft X-rays and Extreme Ultraviolet Radiation*, Cambridge University Press, Cambridge, 1999. doi:10.1017/CB09781139164429.
URL <http://ebooks.cambridge.org/ref/id/CB09781139164429>
- [39] B. Henke, E. Gullikson, J. Davis, *X-Ray Interactions: Photoabsorption, Scattering, Transmission, and Reflection at $E = 50\text{--}30,000$ eV, $Z = 1\text{--}92$* , *Atomic Data and Nuclear Data Tables* 54 (2) (1993) 181–342. doi:10.1006/adnd.1993.1013.
URL <http://www.sciencedirect.com/science/article/pii/S0092640X83710132><http://linkinghub.elsevier.com/retrieve/pii/S0092640X83710132>http://xrm.phys.northwestern.edu/research/pdf/_papers/1993/henke_{_}atomic_{_}1993.pdf
- [40] A. Guinier, *X-ray diffraction in crystals, imperfect crystals, and amorphous bodies*, Dover Publications, New York, 1994.
- [41] R. Klockenkämper, A. von Bohlen (Eds.), *Total-Reflection X-Ray Fluorescence Analysis and Related Methods*, John Wiley & Sons, Inc., Hoboken, New Jersey, 2014. doi:10.1002/9781118985953.
URL <http://doi.wiley.com/10.1002/9781118985953>
- [42] B. Vidal, P. Vincent, *Metallic multilayers for x rays using classical thin-film theory.*, *Applied optics* 23 (11) (1984) 1794.
URL <http://www.ncbi.nlm.nih.gov/pubmed/18212906>
- [43] B. Pardo, T. Megademini, J. André, *X-UV synthetic interference mirrors : theoretical approach*, *Revue de Physique Appliquée* 23 (10) (1988) 1579–1597. doi:10.1051/rphysap:0198800230100157900.
URL <http://www.edpsciences.org/10.1051/rphysap:0198800230100157900>
- [44] U. Weisbrod, R. Gutschke, J. Knoth, H. Schwenke, *Total Reflection X-ray Fluorescence Spectrometry for Quantitative Surface and Layer Analysis*, *Applied Physics A: Materials Science & Processing* 53 (5) (1991) 449–456.
URL <http://www.springerlink.com/index/X2345M48R67417P8.pdf>
- [45] S. Ghose, B. Dev, *X-ray standing wave and reflectometric characterization of multilayer structures*, *Physical Review B* 63 (24) (2001) 1–11. doi:10.1103/PhysRevB.63.245409.
URL <http://link.aps.org/doi/10.1103/PhysRevB.63.245409>
- [46] M.-R. Lefévère, M. Montel, *Rayonnement Electromagnetique*, *C. R. Hebd. Acad. Sci. B* 273 (1971) 329–332.

- [47] M.-R. Lefèvre, M. Montel, Influence de L'absorption sur les Propriétés Optiques des Solides: Propagation des Ondes électromagnétiques Hétérogènes, Planes et Uniformes, dans les Milieux Homogènes et Isotropes, *Optica Acta: International Journal of Optics* 20 (2) (1973) 97–128. doi:10.1080/713818737.
URL <http://www.tandfonline.com/doi/abs/10.1080/713818737>
- [48] V. A. Kizel', MODERN STATUS OF THE THEORY OF LIGHT REFLECTION, *Soviet Physics Uspekhi* 10 (4) (1968) 485–508. doi:10.1070/PU1968v010n04ABEH003698.
URL <http://stacks.iop.org/0038-5670/10/i=4/a=R03?key=crossref.2233ef19dd864063c3cb9ea5c24e5a60>
- [49] K. Stoev, Recent theoretical models in grazing incidence x-ray reflectometry, *The Rigaku J* 14 (2).
URL <http://www.rigaku.com/downloads/journal/Vol14.2.1997/stoev.pdf>
- [50] L. Névot, P. Croce, Caractérisation des surfaces par réflexion rasante de rayons X. Application à l'étude du polissage de quelques verres silicates, *Revue de Physique Appliquée* 15 (3) (1980) 761–779. doi:10.1051/rphysap:01980001503076100.
URL <http://www.edpsciences.org/10.1051/rphysap:01980001503076100>
- [51] H. Schwenke, J. Knoth, U. Weisbrod, Current work on total reflection x-ray fluorescence spectrometry at the GKSS research centre, *X-Ray Spectrometry* 20 (6) (1991) 277–281. doi:10.1002/xrs.1300200606.
URL <http://onlinelibrary.wiley.com/doi/10.1002/xrs.1300200606/abstract>
<http://doi.wiley.com/10.1002/xrs.1300200606>
- [52] J. Als-Nielsen, D. McMorrow, *Elements of Modern X-ray Physics*, John Wiley & Sons, Inc., Hoboken, NJ, USA, 2011. doi:10.1002/9781119998365.
URL <http://doi.wiley.com/10.1002/9781119998365>
- [53] A. von Bohlen, M. Krämer, C. Sternemann, M. Paulus, The influence of X-ray coherence length on TXRF and XSW and the characterization of nanoparticles observed under grazing incidence of X-rays, *Journal of Analytical Atomic Spectrometry* 24 (6) (2009) 792. doi:10.1039/b811178b.
URL <http://xlink.rsc.org/?DOI=b811178b>
- [54] D. Ingerle, P. Wobrauschek, C. Strelt, The influence of beam coherence on

the GIXRF characterization of nanoparticles. Presented in poster session at European Conference on X-Ray Spectrometry 2014 in Bologna (2014).

- [55] D. De Boer, Angular dependence of X-ray fluorescence intensities, *X-Ray Spectrometry* 18 (3) (1989) 119–129. doi:10.1002/xrs.1300180309.
URL <http://onlinelibrary.wiley.com/doi/10.1002/xrs.1300180309/abstract><http://doi.wiley.com/10.1002/xrs.1300180309>
- [56] W. Li, J. Zhu, X. Ma, H. Li, H. Wang, K. Sawhney, Z. Wang, Geometrical factor correction in grazing incident x-ray fluorescence experiment., *The Review of scientific instruments* 83 (5) (2012) 053114. doi:10.1063/1.4722495.
URL <http://www.ncbi.nlm.nih.gov/pubmed/22667609>
- [57] B. Caby, Doctoral Thesis: Development of X-ray Reflectometry (XRR) and Grazing Incidence X ray Fluorescence (GIXRF) combined analysis for micro and nano electronic applications, Ph.D. thesis (2015).
URL <http://www.theses.fr/s116367>
- [58] K. Stoev, K. Sakurai, Aberration effects in quick X-Ray reflectivity of curved samples, *IOP Conference Series: Materials Science and Engineering* 24 (2011) 012014. doi:10.1088/1757-899X/24/1/012014.
URL <http://stacks.iop.org/1757-899X/24/i=1/a=012014?key=crossref.8d03c2a574fd1c70a1e820a6f0a9f15d>
- [59] S. Terada, H. Murakami, K. Nishihagi, Thickness and density measurement for new materials with combined X-ray technique, 2001 IEEE/SEMI Advanced Semiconductor Manufacturing Conference (IEEE Cat. No.01CH37160) (2001) 125–130doi:10.1109/ASMC.2001.925630.
URL <http://ieeexplore.ieee.org/lpdocs/epic03/wrapper.htm?arnumber=925630>
- [60] M. Schiebl, Master's Thesis: Kombination von Röntgenfluoreszenz und Röntgenreflexion bei streifendem Einfall zur verbesserten Charakterisierung von dünnen Schichten und Implantaten auf bzw. in Silizium-Wafern, Master's thesis, Vienna University of Technology (2013).
- [61] D. Ingerle, M. Schiebl, C. Strel, P. Wobrauschek, Combination of grazing incidence x-ray fluorescence with x-ray reflectivity in one table-top spectrometer for improved characterization of thin layer and implants on/in silicon wafers, *Review of Scientific Instruments* 85 (8) (2014) 083110. doi:10.1063/1.4893383.

URL <http://www.ncbi.nlm.nih.gov/pubmed/25173249><http://scitation.aip.org/content/aip/journal/rsi/85/8/10.1063/1.4893383>

- [62] D. Ingerle, A new spectrometer for grazing incidence X-ray fluorescence for the characterization of Arsenic implants and Hf based high-k layers, Master's thesis, Vienna University of Technology (2015). doi:10.1016/j.sab.2010.02.015.

URL <http://resolver.obvsg.at/urn:nbn:at:at-ubtuw:1-86510>

- [63] PANalytical, Empyrean X-ray diffraction system homepage.

URL <http://www.panalytical.com/Empyrean.htm>

- [64] W. Jark, D. Eichert, L. Luehl, A. Gambitta, Optimisation of a compact optical system for the beamtransport at the x-ray fluorescence beamline at Elettra for experiments with small spots, 2014, p. 92070G. doi:10.1117/12.2063009.

URL <http://proceedings.spiedigitallibrary.org/proceeding.aspx?doi=10.1117/12.2063009>

- [65] R. A. Cowley, T. W. Ryan, X-ray scattering studies of thin films and surfaces: thermal oxides on silicon, *Journal of Physics D: Applied Physics* 20 (1) (1987) 61–68. doi:10.1088/0022-3727/20/1/010.

URL <http://iopscience.iop.org/0022-3727/20/1/010><http://stacks.iop.org/0022-3727/20/i=1/a=010?key=crossref.ba0e291dd258574fdce526fec415bbb4>

- [66] S. M. Heald, X-ray reflectivity study of SiO₂ on Si, *Journal of Vacuum Science & Technology A: Vacuum, Surfaces, and Films* 8 (3) (1990) 2046. doi:10.1116/1.576803.

URL <http://link.aip.org/link/?JVA/8/2046/1{&}Agg=doi>

- [67] J. Kirschner, *Parametervariation und ihre Auswirkungen auf Fit-Lösungen*, Project thesis, Vienna University of Technology (2014).

- [68] B. Luokkala, S. Garoff, R. Suter, Using x-ray reflectivity to determine the structure of surfactant monolayers, *Physical Review E* 62 (2) (2000) 2405–2415. doi:10.1103/PhysRevE.62.2405.

URL <http://www.ncbi.nlm.nih.gov/pubmed/11088720><http://link.aps.org/doi/10.1103/PhysRevE.62.2405>

- [69] A. Dane, A. Veldhuis, D. Boer, A. J. G. Leenaers, L. Buydens, Application of genetic algorithms for characterization of thin layered materials by

- glancing incidence X-ray reflectometry, *Physica B: Condensed Matter* 253 (3-4) (1998) 254–268. doi:10.1016/S0921-4526(98)00398-6.
 URL <http://www.sciencedirect.com/science/article/B6TVH-3W2564S-57/2/ddb78eeb7375f30b366df9dd01ff609bhttp://linkinghub.elsevier.com/retrieve/pii/S0921452698003986>
- [70] S. Kirkpatrick, C. D. Gelatt, M. P. Vecchi, Optimization by simulated annealing., *Science (New York, N.Y.)* 220 (4598) (1983) 671–80. doi:10.1126/science.220.4598.671.
 URL <http://www.ncbi.nlm.nih.gov/pubmed/17813860>
- [71] D. E. Goldberg, *Genetic Algorithms in Search, Optimization and Machine Learning*, Addison-Wesley, 1989.
- [72] R. Hooke, T. A. Jeeves, “Direct Search” Solution of Numerical and Statistical Problems, *Journal of the ACM* 8 (2) (1961) 212–229. doi:10.1145/321062.321069.
 URL <http://portal.acm.org/citation.cfm?doid=321062.321069>
- [73] R. Storn, K. Price, Differential Evolution - A Simple and Efficient Heuristic for Global Optimization over Continuous Spaces, *Journal of Global Optimization* 11 (4) (1997) 341–359. doi:10.1023/A:1008202821328.
 URL <http://link.springer.com/10.1023/A:1008202821328>
- [74] J. Kennedy, R. Eberhart, Particle swarm optimization, in: *Proceedings of ICNN'95 - International Conference on Neural Networks*, Vol. 4, IEEE, 1995, pp. 1942–1948. doi:10.1109/ICNN.1995.488968.
 URL <http://ieeexplore.ieee.org/lpdocs/epic03/wrapper.htm?arnumber=488968>
- [75] R. Storn, K. Price, Differential Evolution Homepage, Retrieved from <http://www1.icsi.berkeley.edu/~storn/code.html>.
 URL <http://www1.icsi.berkeley.edu/{~}storn/code.html>
- [76] E. Demenev, D. Giubertoni, J. van den Berg, M. Reading, M. Bersani, Calibration correction of ultra low energy SIMS profiles based on MEIS analyses for arsenic shallow implants in silicon, *Nuclear Instruments and Methods in Physics Research Section B: Beam Interactions with Materials and Atoms* 273 (null) (2012) 192–194. doi:10.1016/j.nimb.2011.07.073.
 URL <http://dx.doi.org/10.1016/j.nimb.2011.07.073http://linkinghub.elsevier.com/retrieve/pii/S0168583X11007178>

- [77] K. Pearson, Contributions to the Mathematical Theory of Evolution., Proceedings of the Royal Society of London 54 (326-330) (1893) 329–333. doi: 10.1098/rsp1.1893.0079.
URL <http://rsp1.royalsocietypublishing.org/cgi/doi/10.1098/rsp1.1893.0079>
- [78] R. G. Wilson, The pearson IV distribution and its application to ion implanted depth profiles, Radiation Effects 46 (3-4) (1980) 141–147. doi: 10.1080/00337578008209163.
URL <http://www.tandfonline.com/doi/abs/10.1080/00337578008209163>
- [79] K. B. Winterbon, Pearson distributions for ion ranges, Applied Physics Letters 42 (2) (1983) 205. doi:10.1063/1.93850.
URL <http://link.aip.org/link/?APL/42/205/1{&}Agg=doi>
- [80] H. Ebel, R. Svagera, M. F. Ebel, A. Shaltout, J. H. Hubbell, Numerical description of photoelectric absorption coefficients for fundamental parameter programs, X-Ray Spectrometry 32 (6) (2003) 442–451. doi:10.1002/xrs.667.
URL <http://doi.wiley.com/10.1002/xrs.667>
- [81] P. Van Espen, K. Janssens, J. Nobels, AXIL-PC, software for the analysis of complex X-ray spectra (1986). doi:10.1016/0169-7439(86)80031-4.
URL <https://www.researchgate.net/profile/Koen{ }Janssens/publication/234802146{ }AXIL-PC{ }software{ }for{ }the{ }analysis{ }of{ }compl links/0deec530110251e5da000000/AXIL-PC-software-for-the-analysis-of-complex-X-pdf>
- [82] V. a. Solé, E. Papillon, M. Cotte, P. Walter, J. Susini, A multiplatform code for the analysis of energy-dispersive X-ray fluorescence spectra, Spectrochimica Acta Part B: Atomic Spectroscopy 62 (1) (2007) 63–68. doi:10.1016/j.sab.2006.12.002.
URL <http://linkinghub.elsevier.com/retrieve/pii/S0584854706003764>
- [83] K. Pearson, Contributions to the Mathematical Theory of Evolution. II. Skew Variation in Homogeneous Material, Philosophical Transactions of the Royal Society A: Mathematical, Physical and Engineering Sciences 186 (January) (1895) 343–414. doi:10.1098/rsta.1895.0010.
URL <http://rsta.royalsocietypublishing.org/cgi/doi/10.1098/rsta.1895.0010>

- [84] K. Pearson, *Mathematical Contributions to the Theory of Evolution. X. Supplement to a Memoir on Skew Variation*, *Philosophical Transactions of the Royal Society A: Mathematical, Physical and Engineering Sciences* 197 (287-299) (1901) 443–459. doi:10.1098/rsta.1901.0023.
URL <http://rsta.royalsocietypublishing.org/cgi/doi/10.1098/rsta.1901.0023>
<http://rsta.royalsocietypublishing.org/cgi/doi/10.1098/rsta.1916.0009>
- [85] D. G. Ashworth, R. Oven, B. Mundin, *Representation of ion implantation profiles by Pearson frequency distribution curves*, *Journal of Physics D: Applied Physics* 23 (7) (1990) 870–876. doi:10.1088/0022-3727/23/7/018.
URL <http://stacks.iop.org/0022-3727/23/i=7/a=018?key=crossref.f36e88028344174c05782a1e26134212>
- [86] K. Suzuki, *Analysis of Ion Implantation Profiles for Accurate Process/Device Simulation: Ion Implantation Profile Database Based on Tail Function*, *Fujitsu Scientific and Technical Journal* (2010) 307–317.
URL <https://www.fujitsu.com/downloads/MAG/vol146-3/paper13.pdf>
- [87] B. Caby, F. Brigidi, D. Ingerle, E. Nolot, G. Pepponi, C. Strelis, L. Lutterotti, A. André, G. Rodriguez, P. Gergaud, M. Morales, D. Chateigner, *Study of annealing-induced interdiffusion in In₂O₃/Ag/In₂O₃ structures by a combined X-ray reflectivity and grazing incidence X-ray fluorescence analysis*, *Spectrochimica Acta Part B: Atomic Spectroscopy* 113 (2015) 132–137. doi:10.1016/j.sab.2015.09.008.
URL <http://www.scopus.com/inward/record.url?eid=2-s2.0-84943406689&partnerID=tZ0tx3y1>
<http://linkinghub.elsevier.com/retrieve/pii/S0584854715002116>
- [88] H. Rotella, B. Caby, Y. Ménesguen, Y. Mazel, A. Valla, D. Ingerle, B. Detlefs, M.-C. Lépy, A. Novikova, G. Rodriguez, C. Strelis, E. Nolot, *Elemental depth profiling in transparent conducting oxide thin film by X-ray reflectivity and grazing incidence X-ray fluorescence combined analysis*, *Spectrochimica Acta Part B: Atomic Spectroscopy* 135 (2017) 22–28. doi:10.1016/j.sab.2017.06.011.
URL <http://linkinghub.elsevier.com/retrieve/pii/S0584854716303950>
- [89] D. Ingerle, F. Meirer, G. Pepponi, E. Demenev, D. Giubertoni, P. Wo-brauschek, C. Strelis, *Combined evaluation of grazing incidence X-ray fluorescence and X-ray reflectivity data for improved profiling of ultra-shallow*

depth distributions., *Spectrochimica acta. Part B: Atomic spectroscopy* 99 (100) (2014) 121–128. doi:10.1016/j.sab.2014.06.019.

URL <http://linkinghub.elsevier.com/retrieve/pii/S0584854714001232><http://www.sciencedirect.com/science/article/pii/S0584854714001232><http://www.pubmedcentral.nih.gov/articlerender.fcgi?artid=4152003&tool=pmcentrez&rendertype=abstract>

[90] D. Ingerle, A. Stanitznig, G. Pepponi, J. J. Leani, A. Migliori, A. G. Karydas, D. Eichert, W. Jark, P. Wobrauschek, J. Zecevic, F. Meirer, C. Strel, Comparison of grazing incidence X-ray fluorescence and X-ray reflectivity data obtained at the XRF beamline of the Elettra Sincrotrone Trieste and an optimized lab spectrometer. Presented at the 16th International Conference on Total Reflection X-ray Fluo (2015).

[91] F. F. Tao (Ed.), *Metal Nanoparticles for Catalysis*, RSC Catalysis Series, Royal Society of Chemistry, Cambridge, 2014. doi:10.1039/9781782621034.

URL <http://ebook.rsc.org/?DOI=10.1039/9781782621034>

[92] M. K. Tiwari, G. M. Bhalerao, M. Babu, A. Sinha, C. Mukherjee, Investigation of metal nanoparticles on a Si surface using an x-ray standing wave field, *Journal of Applied Physics* 103 (5) (2008) 054311. doi:10.1063/1.2885346.

URL <http://link.aip.org/link/JAPIAU/v103/i5/p054311/s1?Agg=doi>

[93] A. von Bohlen, M. Brücher, B. Holland, R. Wagner, R. Hergenröder, X-ray standing waves and scanning electron microscopy - Energy dispersive X-ray emission spectroscopy study of gold nanoparticles, *Spectrochimica Acta Part B: Atomic Spectroscopy* 65 (5) (2010) 409–414. doi:10.1016/j.sab.2010.04.017.

URL <http://linkinghub.elsevier.com/retrieve/pii/S058485471000128X>

[94] D. Ingerle, GIXA project homepage.

URL <http://gixa.ati.tuwien.ac.at>

[95] J. Tiilikainen, M. Mattila, T. Hakkarainen, H. Lipsanen, Novel method for error limit determination in x-ray reflectivity analysis, *Journal of Physics D: Applied Physics* 41 (11) (2008) 115302. doi:10.1088/0022-3727/41/11/115302.

URL <http://stacks.iop.org/0022-3727/41/i=11/a=115302?key=crossref.9176a9152e1c756405912639edd53159>

Dieter Ingerle

Flor.Hauptstr. 22/4/9 • 1210 Wien • Tel.: +43 680 3342162

Curriculum Vitae

■ Personal Information

Name: Dieter Stefan Ingerle
Date of birth: 22.09.1975
Nationality: Austria

■ Education

1981 – 1985 Henry-Dunant-Volksschule
1985 – 1993 Öffentliches Gymnasium der Stiftung Theresianische Akademie Wien
1993 Matura (exit exam) passed with merit
1994 – 2015 Student of Technical Physics at the Vienna University of Technology
2015 Master Thesis “A new spectrometer for grazing incidence X-ray fluorescence for the characterization of Arsenic implants and Hf based high-*k* layers”
Since 2015 PhD student in technical sciences at the Vienna University of Technology

■ Work Experience

Since 1998 Unterberger EDV-Beratung
Software developer for several clients (Arwag, Raiffeisen Ware Austria, XXXLutz)
2000 – 2010 ITP – IT Services Paier GmbH
Firewall specialist (Censeo Vermögensverwaltung, Club Danube, Massenbauer Finanzierungsberatung, Mehrsicht Unternehmensberatung, Wallner & Neubert) and software developer (BMF, Topcall)
2011 – 2016 Project assistant at the Institute of Atomic and Subatomic Physics (Atominstitut) for FWF-Project P23832-N20 (Synchrotron radiation induced GIXRF with absorption spectroscopy)
Software development JGIXA

■ **Language Skills**

German (Mother Tongue)

English (Fluent)

French (Advanced)

Russian (Elementary)

■ **Personal Skills**

Programming Languages: Java, Matlab, C++, C#, SQL